FINAL REPORT ON

RADAR IMAGE ENHANCEMENT, FEATURE EXTRACTION AND MOTION COMPENSATION USING JOINT TIME-FREQUENCY TECHNIQUES

Office of Naval Research
Research Grant N00014-98-1-0615

For the period April 15, 1999 through September 30, 2001

Submitted by

Professor Hao Ling

Department of Electrical and Computer Engineering
The University of Texas at Austin
Austin, TX 78712-1084

October 31, 2001

DISTRIBUTION STATEMENT A
Approved for Public Release
Distribution Unlimited

20011116 223

REPORT DOCUMENTATION PAGE

Form Approved
OMB No. 0704-0188

Public reporting burden for this collection of information is estimated to average 1 hour per response, including the time for reviewing instructions, searching existing data sources, gathering and maintaining the data needed, and completing and reviewing the collection of information. Send comments regarding this burden estimate or any other aspect of this collection of information, including suggestions for reducing this burden to Washington Headquarters Services, Directorate for Information Operations and Reports, 1215 Jefferson Davis Highway, Suite 1204, Arlington, VA 22202-4302, and to the Office of Management and Budget, Paperwork Reduction Project (0704-0188), Washington, DC 20503.

1. AGENCY USE ONLY *(Leave blank)*	2. REPORT DATE	3. REPORT TYPE AND DATES COVERED
	October 31, 2001	Final Report 15 April 98-30 Sept 01

4. TITLE AND SUBTITLE
Final Report on Radar Image Enhancement, Feature Extraction and Motion Compensation Using Joint Time-Frequency Techniques

5. FUNDING NUMBERS
Research Grant ONR N00014-98-1-0615

6. AUTHOR(S)
Hao Ling

7. PERFORMING ORGANIZATION NAMES(S) AND ADDRESS(ES)
The University of Texas at Austin
Department of Electrical and Computer Engineering
Austin, TX 78712-1084

8. PERFORMING ORGANIZATION REPORT NUMBER
No. 3

9. SPONSORING / MONITORING AGENCY NAMES(S) AND ADDRESS(ES)
Office of Naval Research
Ballston Centre Tower One
800 North Quincy Street
Arlington, VA 22217-5660

Program Officer
William Miceli/G.D. McNeal
ONR 313

10. SPONSORING / MONITORING AGENCY REPORT NUMBER

11. SUPPLEMENTARY NOTES

a. DISTRIBUTION / AVAILABILITY STATEMENT
Approved for Public Release
Distribution Unlimited

12. DISTRIBUTION CODE

13. ABSTRACT *(Maximum 200 words)*

This report summarizes the scientific progress on the research grant "Radar Image Enhancement, Feature Extraction, and Motion Compensation Using Joint Time-Frequency Techniques" during the period 15 April 1998-30 September 2001. Research on radar motion compensation using NATO and Navy SCATR radar data, feature extraction of targets with movable components, and radar image formation in the presence of chaotic target motions is presented.

14. SUBJECT TERMS
Radar imaging, joint time-frequency techniques

15. NUMBER OF PAGES
139

16. PRICE CODE

17. SECURITY CLASSIFICATION OF REPORT	18. SECURITY CLASSIFICATION OF THIS PAGE	19. SECURITY CLASSIFICATION OF ABSTRACT	20. LIMITATION OF ABSTRACT
Unclassified	Unclassified	Unclassified	

FINAL REPORT ON

RADAR IMAGE ENHANCEMENT, FEATURE EXTRACTION AND MOTION COMPENSATION USING JOINT TIME-FREQUENCY TECHNIQUES

Office of Naval Research
Research Grant N00014-98-1-0615

For the period April 15, 1999 through September 30, 2001

Submitted by

Professor Hao Ling

Department of Electrical and Computer Engineering
The University of Texas at Austin
Austin, TX 78712-1084

October 31, 2001

RADAR IMAGE ENHANCEMENT, FEATURE EXTRACTION AND MOTION COMPENSATION USING JOINT TIME-FREQUENCY TECHNIQUES

Project Starting Date:	April 15, 1998
Reporting Period:	April 15, 1998 – September 30, 2001
Principal Investigator:	Professor Hao Ling (512) 471-1710 ling@ece.utexas.edu
Graduate Students:	Y. Wang, H. Deng, J. Li, Y. Zhou, S. Nam
Undergraduate Students:	M. Andringa, D. Buhl, M. Anderson
Research Associate:	R. Bhalla

A. SCIENTIFIC OBJECTIVES: The objective of this research program is to devise innovative joint time-frequency (JTF) processing concepts for radar image enhancement and physics-based feature extraction. In particular, we investigate how JTF techniques can be utilized to enhance synthetic aperture radar (SAR) and inverse synthetic aperture radar (ISAR) imageries by removing artifacts due to uncompensated target motion, complex target scattering physics, articulating target components and clutter and propagation effects. Furthermore, we set out to re-interpret the extracted artifacts in a more meaningful feature space so that they can be utilized to enhance the performance of target identification algorithms. This research is leveraged against our previous JTF work under the Joint Services Electronics Program, as well as our state-of-the-art radar signature simulation capabilities. The JTF-based radar image processing tools developed under this program will be disseminated to radar researchers in the US Navy.

B. SUMMARY OF RESULTS AND SIGNIFICANT ACCOMPLISHMENTS: During this program, we have followed two lines of research: (i) processing real radar data to identify needed areas of research and to test our JTF algorithms, (ii) developing new JTF algorithms to address the problem areas identified in (i).

Our accomplishments along the first line of research include:

1.1 Application of JTF motion compensation algorithm to NATO TIRA radar data.

1.2 Processing of NATO MERIC radar data.

1.3 Processing of Navy SCATR data.

Along the second line of research, we have focused on two key research areas identified from processing of measurement data. The first area focuses on the imaging of targets with movable components. We have developed a number of JTF algorithms to extract features from targets having moving components:

2.1 Removal of image artifacts due to helicopter rotor blades.

2.2 Removal of image artifacts due to jet engine modulation.

2.3 Extraction of microDoppler features from ISAR data using adaptive chirplet representation.

The second area focuses on targets having highly chaotic motions. We have addressed a number of issues in image formation in the presence of chaotic target motions:

3.1. Three-dimensional motion detection using JTF algorithm.

3.2. 3D ISAR image reconstruction of a target with motion data.

3.3. Application of genetic algorithms to ISAR imaging.

Finally, we have carried out some exploratory research on two topics related to radar imaging and JTF analysis:

4.1. Clutter reduction for SAR images using adaptive wavelet packet transform.

4.2. Inverse scattering using genetic algorithms.

The detailed descriptions of our accomplishments are discussed below.

1.1. Application of JTF Motion Compensation Algorithm to NATO TIRA Data. We have devoted considerable efforts to process the NATO TIRA radar data taken in Germany in November 1997. The objectives of this effort are to test our previously developed adaptive joint time-frequency (AJTF) algorithm [1] for ISAR motion compensation and to identify needed areas of research in ISAR-based target recognition. Our algorithm uses a search and projection technique in the joint (dwell time)-(Doppler frequency) plane to select and track the prominent point scatterers. The higher-order translation and rotation motions are then extracted and compensated for in the data to

form a focused image of the target. The motion compensated images have been compared against the reference images generated by using the motion information available in the instrumented ARDS data. Furthermore, comparison has also been made with the simulated ISAR images of the air target from the radar signature prediction code Xpatch. A set of representative images is shown below. Figs. 1.1.1(a), (b) and (c) are the images for a target at azimuth=56° (0° being nose-on) generated using, respectively, AJTF motion compensation, ARDS sensor information and Xpatch simulation. The dynamic range of the displayed images is 55 dB. The look angle information was deciphered from the ARDS data. By comparing Figs. 1.1.1(a) and 1.1.1(b), we observe that the motion compensated image and the ARDS-derived reference image appear to be in good agreement. The Xpatch image is more focused and does not exhibit the diffused characteristics of the measurement data. A more detailed CAD model should improve the quality of the predicted image.

While the comparison among the images is quite good, we have identified several needed areas of research in ISAR-based target recognition. Fig. 1.1.2 shows both the correlation coefficient between the JTF and truth images and that between the JTF and Xpatch images versus azimuth look angle. From the two curves, we see that the JTF images agree very well with the truth images, indicating that blind motion compensation is a very feasible method for processing real-world radar data. The correlation coefficient between the JTF and Xpatch images is slightly lower than that between the measured images. In particular, two problem regions can be seen from this plot. First, in the region near nose-on (180 degrees in azimuth), the correlation coefficient is significantly lower. The reason is due to the strong jet engine modulation (JEM) lines in the measured data. This problem is further discussed in 2.2 and an algorithm to remove JEM lines is proposed. Second, at some angles around the broadside region (90 degrees in azimuth), the correlation coefficient is also low. In this case, both the associated JTF image and the truth image are both found to be of low quality. After further investigation, it is found that the image blurring is due to the non-steadiness of the imaging plane. This problem is further addressed in 3.1.

(a) Motion compensated Image using AJTF processing

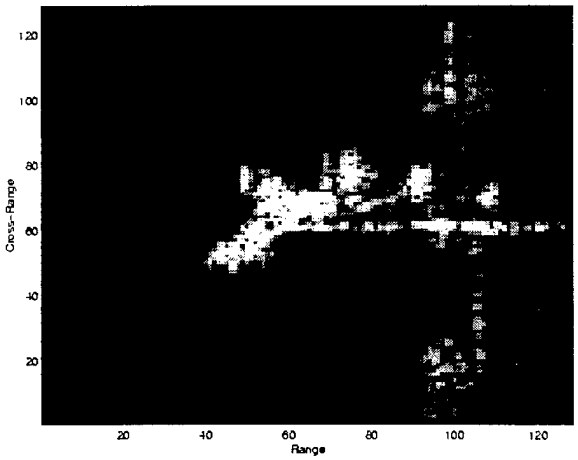

(b) Reference image based on ARDS motion data

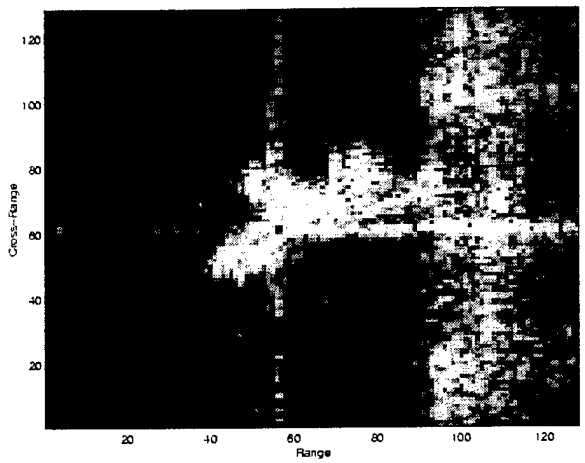

(c) Synthetic image from Xpatch simulation.

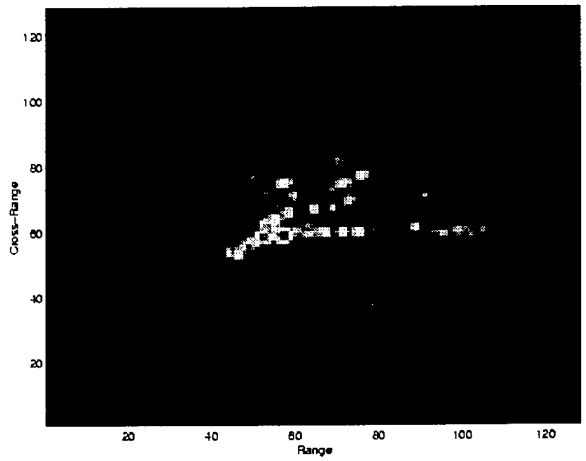

Fig. 1.1.1. A TIRA target at azimuth=56°.

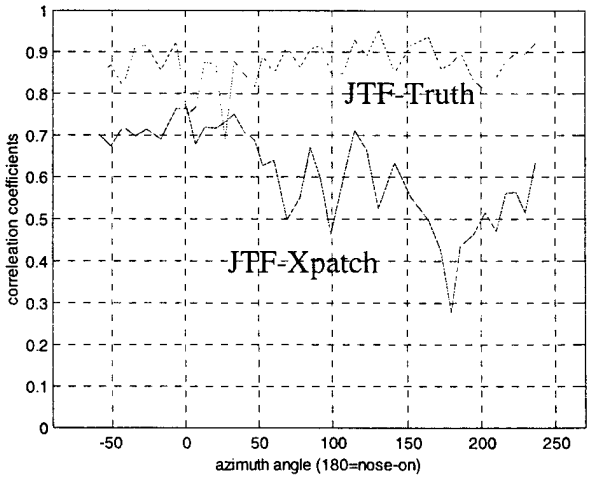

Fig. 1.1.2. Correlation coefficients between JTF and truth images, and between JTF and Xpatch.

1.2. Processing of NATO MERIC Radar Data. We have also processed the MERIC radar data made available to us through the Naval Research Laboratory. Blind motion compensation is more challenging in this case, as the flight path of the aircraft was very close to the radar and the instrument data showed more variations in azimuth and elevation angles during the flight of the aircraft. The task is further complicated by the lack of sufficient instrument data (some of the ARDS pod data had been heavily down-sampled and written into Microsoft Excel form in the MERIC data set). In addition, some of the radar data contain very strong colored noise in the background and considerable effort was spent on denoising the data. Despite these difficulties, the final JTF image quality we have generated is fairly good. Fig. 1.2.1 shows the angular motion parameters of an aircraft for which the radar data are available. The aircraft undergoes an azimuth rotation of about 25 degrees during the 17.5-sec collection period. While there are 35,000 pulses of radar range profiles during this duration, only 18 samples of instrument data are available in the same duration. Consequently, no ground truthing was possible due to the lack of sufficient instrument data. To validate our results, we have generated the Xpatch prediction using a CAD model purchased from viewpoint.com. It is however not the exact model for the aircraft used in the measurement. The model was first converted into an Xpatch-compatible format. It was then edited to remove the landing gear and bomb loads under the wings, as well as to seal up the open seams in the model. Some comparison results are presented in Fig. 1.2.2. Figs. 1.2.2(a) and 1.2.2(b) show respectively the JTF motion compensated image and the Xpatch predicted image near point P of Fig. 1.2.1 in the flight path. The agreement between the MERIC image and the Xpatch simulated image is fairly good, considering the uncertainties in the CAD model. Figs. 1.2.2(c) and 1.2.2(d) show respectively the JTF motion compensated image and the Xpatch predicted image near point Q of Fig. 1.2.1 in the flight path. It is clear that the agreement is quite poor in this case. The blind image formation is quite challenging during this particular portion of the flight. Furthermore, we are not certain of the exact imaging plane for the simulation due to the sparseness of instrument data. An interesting phenomenon was observed from the motion compensated image of a second aircraft. The formed images show Doppler smearing near the nose region. After some research on this aircraft, we have determined that it is very likely due to movement from

a mechanically scanned antenna in the nose cone of the aircraft. This topic is investigated in more detail in 2.3.

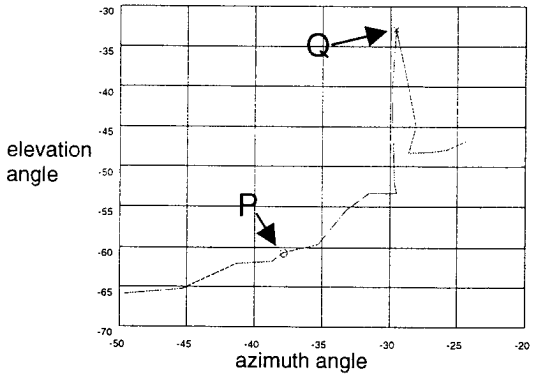

Fig. 1.2.1. Azimuth versus elevation angles of the aircraft with respect to the radar during the flight path.

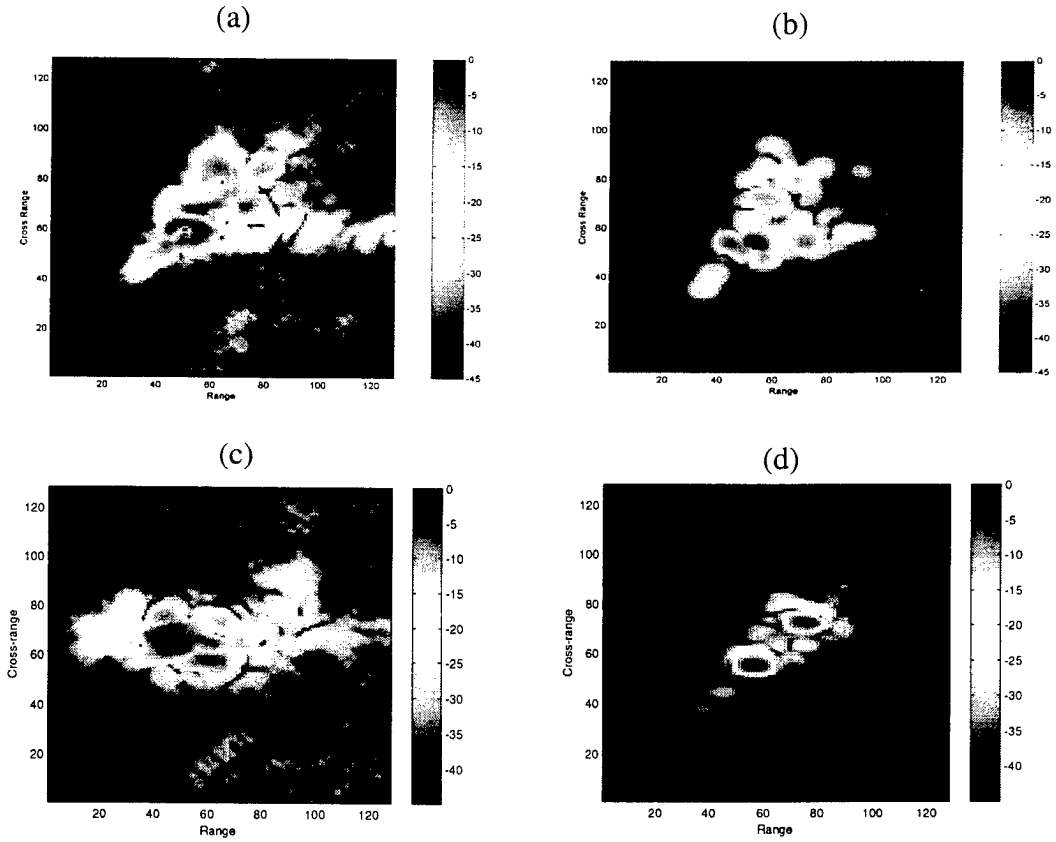

Fig. 1.2.2. Comparison of the MERIC image to Xpatch simulation. (a) JTF motion compensated image at point P. (b) Xpatch simulated image at point P. (c) JTF motion compensated image at point Q. (d) Xpatch simulated image at point Q.

1.3. Processing of Navy SCATR Data. We have also processed the small craft (SCATR) radar data made available to us through the Naval Research Laboratory. In contrast to the air data, the motion of the small boat is strongly dictated by the motion of the ocean surface. As a result, the radar image shows rapid variation in the imaging plane and the interpretation of the images becomes more challenging. Fig. 1.3.1(a) shows the model of the boat. Fig. 1.3.1(b) shows the ISAR image formed using the JTF motion compensation algorithm during a particular dwell duration. The quality of the image is fair. Fig. 1.3.1(c) shows the pose of the target with respect to the radar generated using the data recorded by the GPS sensors carried on the boat. Because the GPS data was not sufficient to fully determine the pose, a number of assumptions were made to generate the pose information. As a result, we were not fully confident that the radar data and the motion data have good correspondence. Nevertheless, we proceeded to interpret the motion data. It is clearly seen from Fig. 1.3.1(c) that the rotational motion of the target over a 3° by 6° AZ-EL angular window follows a rather chaotic path and is not well confined to a 2D plane. Fig. 1.3.1(d) shows the projection of the target model into the corresponding imaging plane. As we can see, during this particular (labeled in red) imaging interval, the image correspond approximately to the sideview of the boat. However, during the subsequent collection intervals, the image plane changes quite rapidly to other views of the target. This issue is similar to the problem we have encountered in air targets. However, it occurs much more frequently and the effect is much more dramatic for small boats. Moreover, it becomes increasingly difficult to find a sufficiently long imaging interval even to form a decent image. The issue of finding good imaging intervals will be further discussed in 3.1.

2.1. Removal of Image Artifacts due to Helicopter Rotor Blades. It is well known that when rotating components exist on a target such as gimbaled antennas or propeller blades, image artifacts are introduced in the Doppler dimension of the ISAR image [2, 3]. These smeared features oftentimes overshadow the target geometrical features and hinder the proper interpretation of the ISAR image. We have developed a technique to remove such Doppler smear and produce a clear ISAR image of the target based on adaptive joint time-frequency processing [4, 5]. The technique entails adaptively searching for the

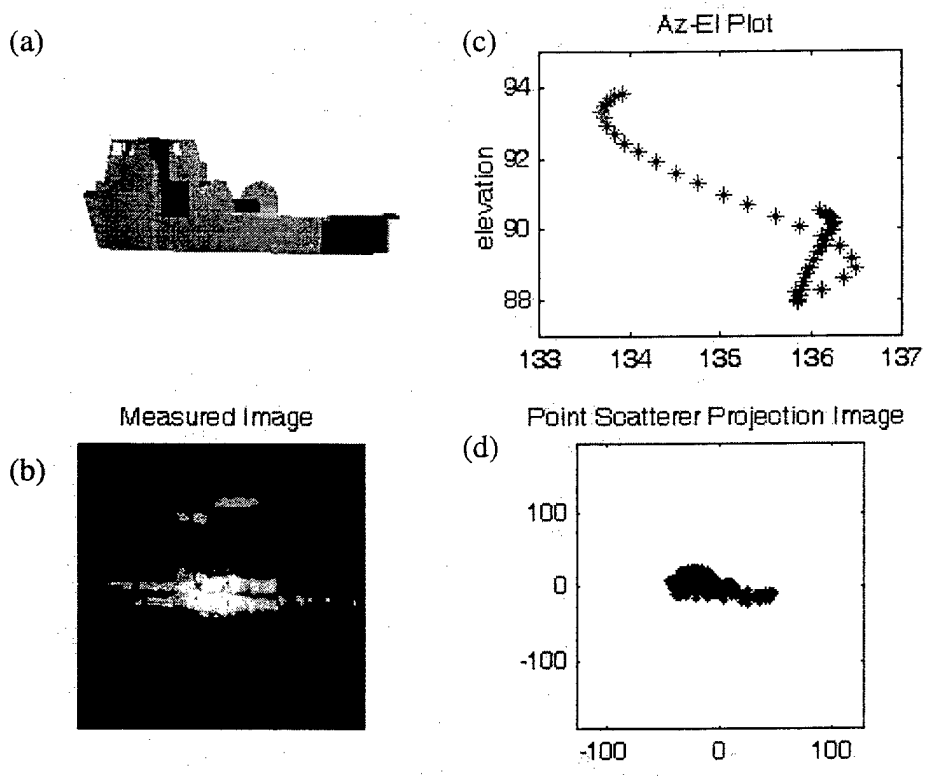

Fig. 1.3.1. Image from the SCATR data. (a) Target CAD model. (b) Image formed using the AJTF algorithm. (c) Target pose data determined from GPS data. (d) Target model projected into the corresponding imaging plane.

linear chirp bases that best represent the time-frequency behavior of the signal. This is accomplished by projecting the signal onto all possible chirp bases and finding the one with the maximum projection value. After the optimal basis is found, the signal component associated with this basis is subtracted from the original signal. By iterating this search procedure, the signal can be fully parameterized with a set of chirp basis functions. Since the Doppler frequency due to the rotating component is both larger and more rapidly varying (in dwell time) than that from the target body, the signal components due to the fast rotating part are associated with those chirp bases having large displacement and slope parameters. On the other hand, the signal components due to the target body motion are represented by those chirp bases with relatively small

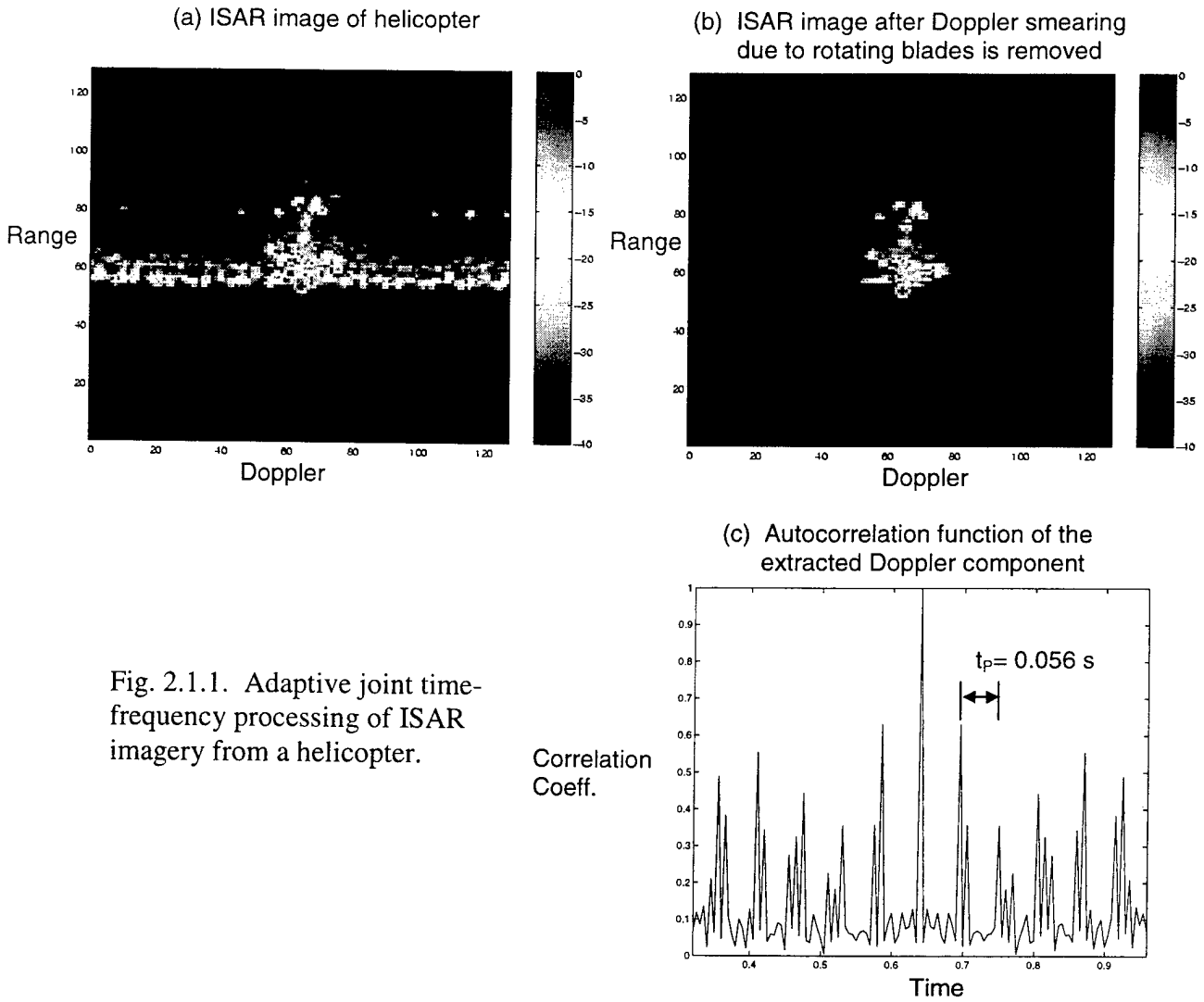

Fig. 2.1.1. Adaptive joint time-frequency processing of ISAR imagery from a helicopter.

displacement and slope parameters. By sorting these chirp bases according to their slopes and displacements, the scattering due to the fast rotating part can be separated from that due to the target body. Consequently a cleaned ISAR image of the target body can be reconstructed by using only those bases associated with the body motion. Furthermore, robust Doppler information extraction can be achieved by applying the period detection algorithm to the component associated with rotating parts only. We have applied this algorithm to both simulated data from the radar prediction code Xpatch and some real measurement results for helicopters and propeller airplanes with good success. The measured data were provided by Dr. Victor Chen of Naval Research Laboratory. An example demonstrating the algorithm is shown in Fig. 2.1.1. Fig. 2.1.1(a) shows the

original ISAR image of a helicopter. The Doppler smearing due to the rotating blades is clearly visible and overlaps with the target features. Fig. 2.1.1(b) shows the image after the adaptive joint time-frequency feature extraction procedure is applied to remove the Doppler component due to the rotating blades. The Doppler smearing is significantly reduced and the target features become much more apparent. The removed Doppler smearing contains useful information on the blade rotation rate and a period detection algorithm can be applied to extract the rotation rate of the blades. Fig. 2.1.1(c) shows the autocorrelation function versus dwell time of the extracted blade contribution. From this plot, we can determine the periodicity of the signal to be 0.056 s. The reciprocal of the period is 17.7 rps and it corresponds to the product of the blade rotation rate and the number of blades for this target. This algorithm can also be extended to deal with jet engine modulation (JEM) and is discussed next.

2.2. Removal of Image Artifacts due to Jet Engine Modulation. Jet engine modulation (JEM) is a well-known phenomenon caused by the high-speed rotation of the aircraft engine. For imaging radars, the typical PRF is much slower than the engine rotation frequency. Thus the resulting ISAR image in the frontal region of an aircraft contains an aliased component along the cross range dimension, as shown by the TIRA image in Fig. 2.2.1(a). Such effect is difficult to predict accurately using simulation [6, 7]. Furthermore, JEM lines are noise-like and can corrupt the geometrical features of the target in the ISAR image. For ISAR-based target recognition, it would be useful to devise an algorithm to separate the JEM lines from the target image before the subsequent classification process. In 2.1, we demonstrated the separation of the rotating blade contribution from the body image in helicopter data. However, JEM possesses new challenges due to the high rotational rate of the jet engine and additional electromagnetic propagation effect through the inlet duct. We have carried out JEM removal on TIRA data using the AJTF algorithm. The model we adopt assumes that the aircraft consists of a slowly rotating body with a constant rotational velocity Ω_b and a fast moving engine component with a different rotational velocity Ω_p. The received radar return as a function of dwell time can thus be written as:

$$E(t_D) = \sum_{k=1}^{N_b} A_k \exp[-j\frac{4\pi f}{c}(R(t_D) + x_k \cos(\Omega_b t_D) + y_k \sin(\Omega_b t_D)] \\ + \sum_{k=N_b+1}^{N} A_k \exp[-j\frac{4\pi f}{c}(R(t_D) + x_k \cos(\Omega_p t_D) + y_k \sin(\Omega_p t_D)] \tag{2.2.1}$$

where N is the total number of point scatterers within one range cell, of which N_b are the body scatterers. Usually Ω_p is much greater than Ω_b. While the first term can be meaningfully mapped into the image plane of the target via the Fourier transform, the second term results in serious Doppler smearing across the cross range domain.

We can also utilize the AJTF technique to separate the fast moving part from the relatively slow moving body. For the component due to target body scattering, the Doppler frequency is

$$f_D^b = \frac{4\pi f}{c}\Omega_b[y\cos(\Omega_b t_D) + x\sin(\Omega_b t_D)] \approx \frac{4\pi f}{c}\Omega_b(y + x\Omega_b t_D) \tag{2.2.2}$$

while the Doppler frequency due to the fast rotating part is

$$f_D^p = \frac{4\pi f}{c}\Omega_p[y\cos(\Omega_p t_D) + x\sin(\Omega_p t_D)] \tag{2.2.3}$$

We see that (2.2.2) is a linear function of dwell time while (2.2.3) is a sinusoidal function. If we parameterize the signal by basis functions that have linear Doppler frequency behavior as a function of dwell time, the two signals can be approximately separated by their displacement and slope parameters. We utilize the AJTF processing technique to carry out the parameterization. The signal component due to the target scattering is reconstructed by using all the bases with small displacement and small slope parameters. Fig. 2.2.1(b) shows the image after the JEM removal processing. Note that the body features are unveiled after the JEM removal. Fig. 2.2.2 shows the correlation between the synthetic images and the measured images from TIRA after JEM removal. We observe that the correlation coefficients in the JEM region are increased after we remove the JEM interference from the body. Further research is needed in this area to more definitively assess the effect of JEM removal in the performance of target classification algorithms.

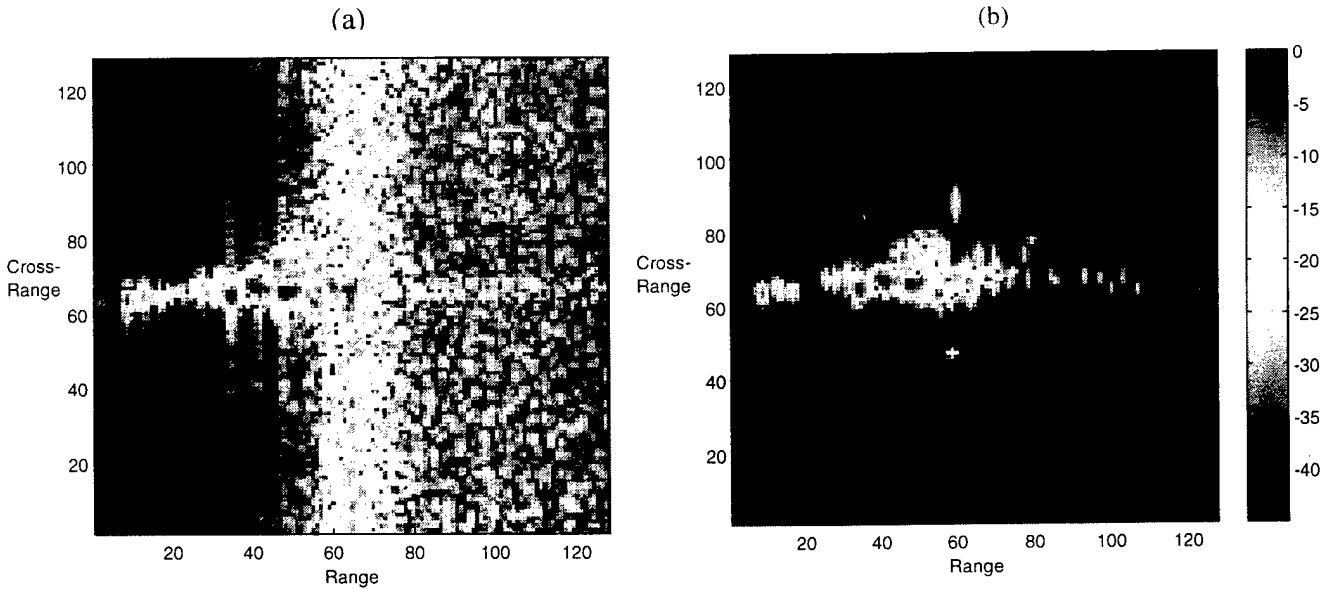

Fig. 2.2.1. TIRA image from a frontal view. (a) Before JEM processing. (b) After JEM removal using the AJTF algorithm.

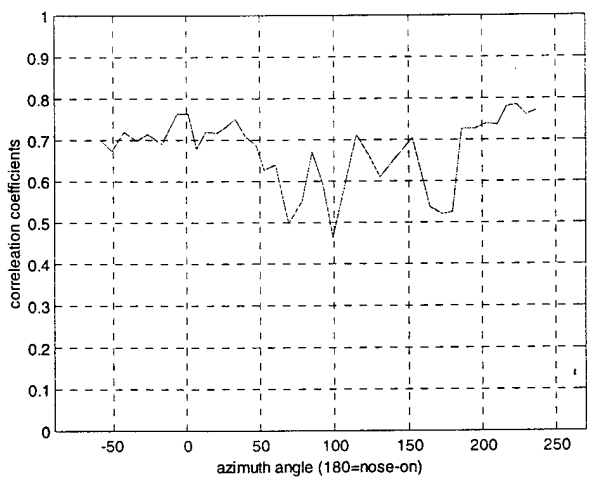

Fig. 2.2.3. Correlation between JTF and Xpatch images after JEM removal.

2.3. Extraction of MicroDoppler Features from ISAR Data Using Adaptive Chirplet Representation. Under the assumption of rigid body motion, traditional high-resolution ISAR imaging is capable of generating a (range)-(cross range) image of the target. When

the target contains non-rigid body motion, the resulting radar image does not preserve the spatial features of the target. In 2.1 and 2.2, we have studied algorithms to remove the artifacts due to the rotating blades of a helicopter and the jet engine modulation (JEM). In this work, we set out to extract the so-called microDoppler features due to the small motions of a non-rigid target [8].

For this purpose, the chirplet basis function proposed in [9] is used. The radar signal as a function of dwell time t is expanded in terms of N basis functions as follows:

$$s(t) = \sum_{k=1}^{N} a_k (\alpha_k / \pi)^{1/4} \exp[-\alpha_k (t - tk)^2 + j2\pi f_k (t - t_k) + j\pi\beta_k (t - t_k)^2] \qquad (2.3.1)$$

Each basis function is a four-parameter chirplet with time location t_k, frequency center f_k, time extent α_k, and chirp rate β_k. The parameters for all the individual chirplets are found adaptively. The chirplet with the highest energy is extracted first. We exhaustively search for the maximum projection from the radar signal onto the set of basis functions in the parameter space. Once the best basis is identified, we then subtract its contribution from the radar signal and continue to search for the next best basis. This process is iterated until we have a good representation the original signal.

The radar data from the PI-walking data collected using the APY-6 radar has been used to test the algorithm. During the data collection, a man walked toward the radar. At least two different motions were present on the walking man: the steady body motion and the swinging arm motion. We first carry out a coarse range alignment by correlating the range profiles. The signal through a particular range cell is then used for JTF processing. Shown in Fig. 2.3.1 is the spectrogram of the radar signal in a particular range cell containing strong micro-Doppler. We immediately recognize the two motion components present in this figure. The horizontal trajectory is due to the body motion, while the sinusoidal curve is due to the arm swing.

We apply the JTF extraction and extract 50 chirplets. After the parameterization, we separate the body and the arm returns. As can be seen in Fig. 2.3.1, the body return should consist of chirplet bases with both small Doppler frequency f_k and small chirp rate β_k. By applying this criterion to the basis functions representing the signal, we can separate the body return from the arm return. The results are shown in Figs. 2.3.2(a) and 2.3.2(b), respectively. Notice that the main features in the two returns are preserved after

the JTF extraction. The Doppler features due to the arm swing shown in Fig. 2.3.2(b) is nearly periodic. This period can be easily estimated from the arm-only data by taking the autocorrelation of the time sequence. The result is shown in Fig. 2.3.3(a). The peaks in the autocorrelation function indicate the period of the motion and it is estimated to be 0.44 sec. Note that without using JTF analysis, accurate detection of the swing period would be more difficult due to the presence of the body return. The autocorrelation calculated from the unfiltered data is shown in Fig. 2.3.3(b). As we can see, the peaks are much less prominent.

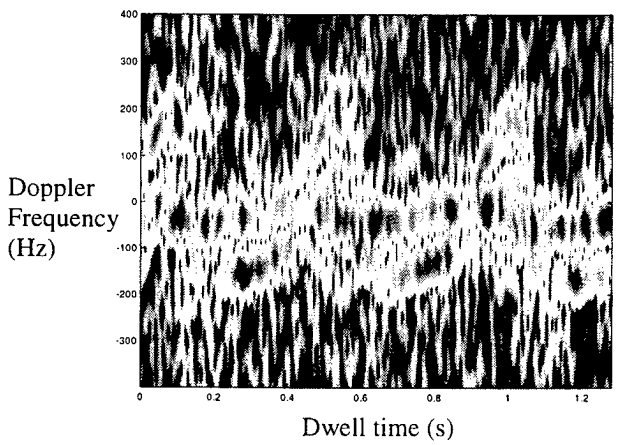

Fig. 2.3.1. Spectrogram of the radar signal showing micro-Doppler

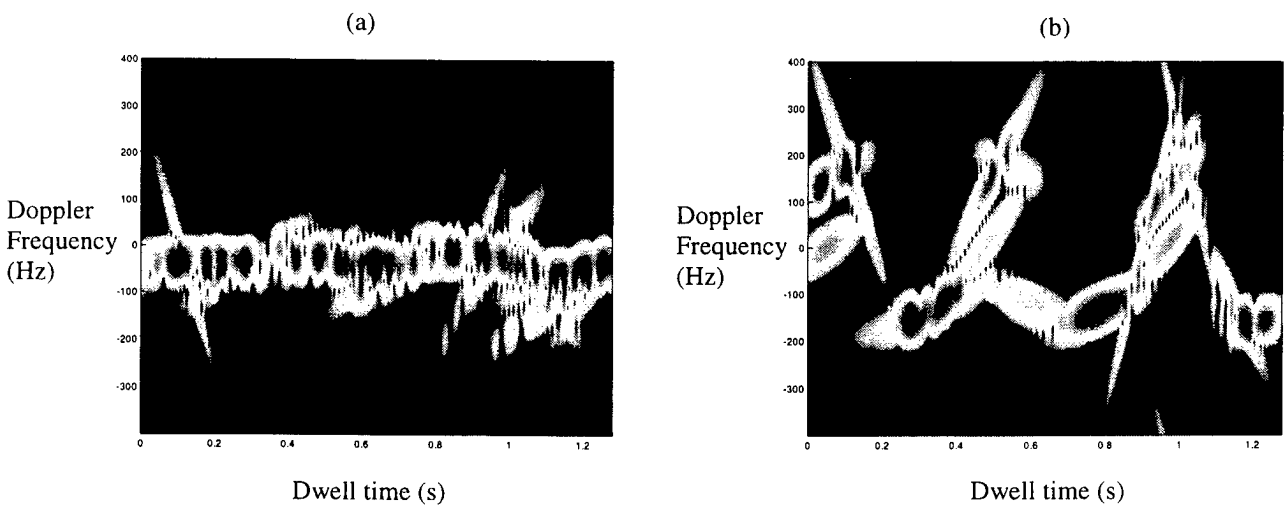

Fig. 2.3.2. Separation of the contribution from (a) the body and (b) the swing arm using the adaptive chirplet representation.

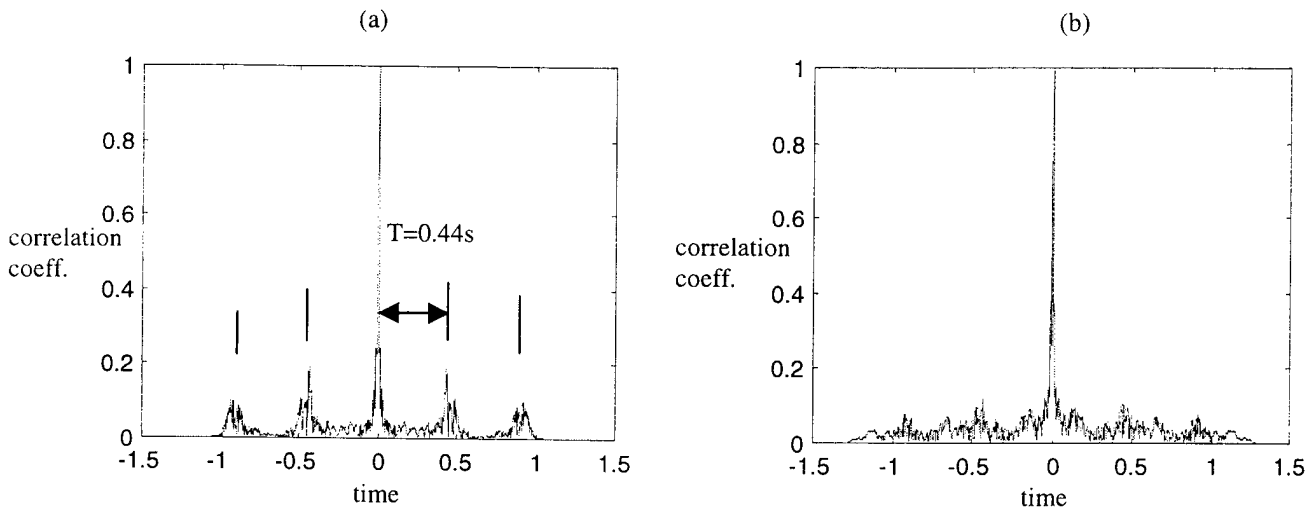

Fig. 2.3.3. Autocorrelation to determine the rate of arm swing. (a) after JTF extraction (b) before JTF extraction.

3.1. Three-Dimensional Motion Detection Using JTF Algorithm. One basic assumption of existing motion compensation algorithms is that the target only undergoes motion in a two-dimensional plane (i.e., it has a steady rotational axis) during the dwell interval needed to form an image. From several independent examinations of measured ISAR data sets recently, it was reported that the presence of three-dimensional motion is quite detrimental to the formation of a well-focused image [10-12]. This is also consistent with our own findings from the TIRA and MERIC data. For some image frames, we found that the motion compensated image and the associated truth images are both quite poor. An example image is shown in Fig. 3.1.1(a). When we examine the motion data from the aircraft instrument, we find that the aircraft motion is not confined to a two-dimensional plane during the imaging interval. Fig. 3.1.1(b) shows the plot of the elevation versus azimuth look angles of the aircraft from the radar. This curve should be linear if the motion is strictly two-dimensional, and in this case, there is clearly three-dimensional motion. In general, we will not be able to form a focused image using an

existing motion compensation assumption, since the assumed model is mismatched to the actual target motion. The ultimate goal in this research is to develop a general motion compensation algorithm to handle targets with arbitrary three-dimensional motion. However, this problem is quite challenging, if not impossible [13]. Instead, we address a less ambitious problem of detecting the presence of three-dimensional motion from raw radar data. It is hoped that the solution here will be a stepping stone to the ultimate three-dimensional motion compensation problem.

Allowing for arbitrary three-dimensional motion in space, we consider the following model as a generalization of the two-dimensional motion model:

$$E(t_D) = \sum_{k=1}^{N} A_k \exp[-j\frac{4\pi f_c}{c}(x_k + y_k\theta(t_D) + z_k\phi(t_D))] \tag{3.1.1}$$

where θ is the azimuth angle of the target with respect to the radar, and ϕ is the elevation angle. In (3.1.1), it is assumed that the translation motion has been removed and that the standard small-angle, small bandwidth approximations apply. This model reduces to the standard two-dimensional motion model when θ and ϕ are linearly related. Our approach to the three-dimensional motion detection problem is to utilize the AJTF algorithm to extract the phase behavior of the radar data at multiple range cells. It can be shown that when the target undergoes only two-dimensional motion during the dwell duration, the relationship between the phase extracted from one range cell and that from another range cell should be linear. For three-dimensional motion, the relationship is in general nonlinear. Therefore, by examining the linearity of the phase relationships from different range cells, we can distinguish two-dimensional motion from three-dimensional motion. Fig. 3.1.2 shows our results from the TIRA data. Fig. 3.1.2(a) shows the degree of three-dimensional motion in the data for 20 different image frames, detected by applying our algorithm to the raw TIRA radar data. As a reference for comparison, Fig. 3.1.2(b) shows the degree of three-dimensional motion for the same 20 frames measured using the instrumentation data. It can be seen that our algorithm correctly detects where significant three-dimensional motions exist. We believe this detection algorithm could be quite useful for determining the "good" imaging intervals from which focused images can be more readily generated. For targets that exhibit very chaotic motions, such as ships on

the ocean, finding such intervals of opportunity may be very critical for target recognition.

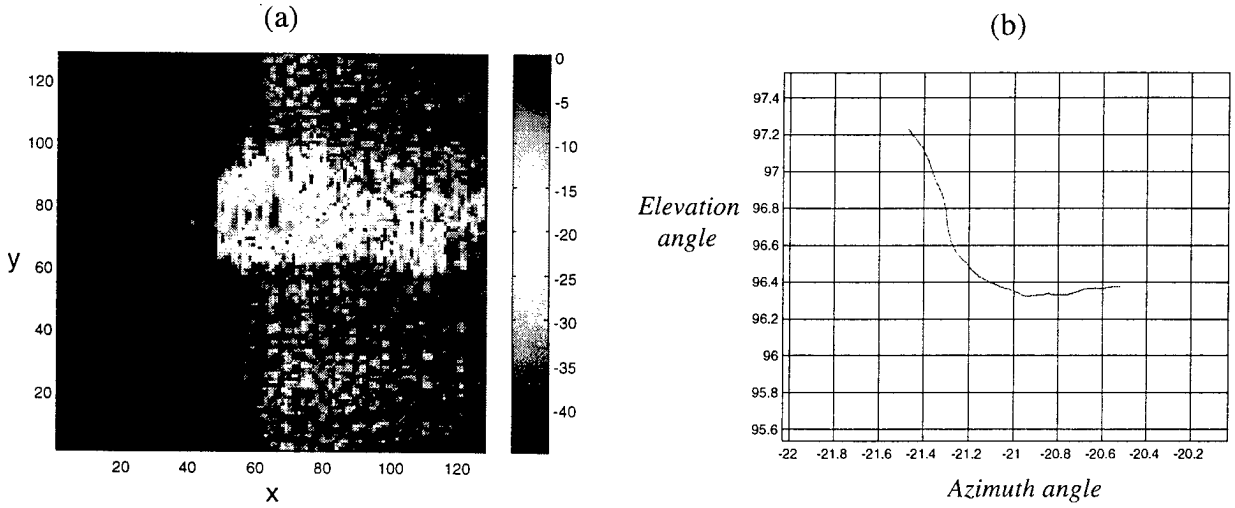

Fig. 3.1.1. Effect of non-steady imaging plane on image quality. (a) A poorly focused image. (b) The corresponding target motion from the instrumentation data.

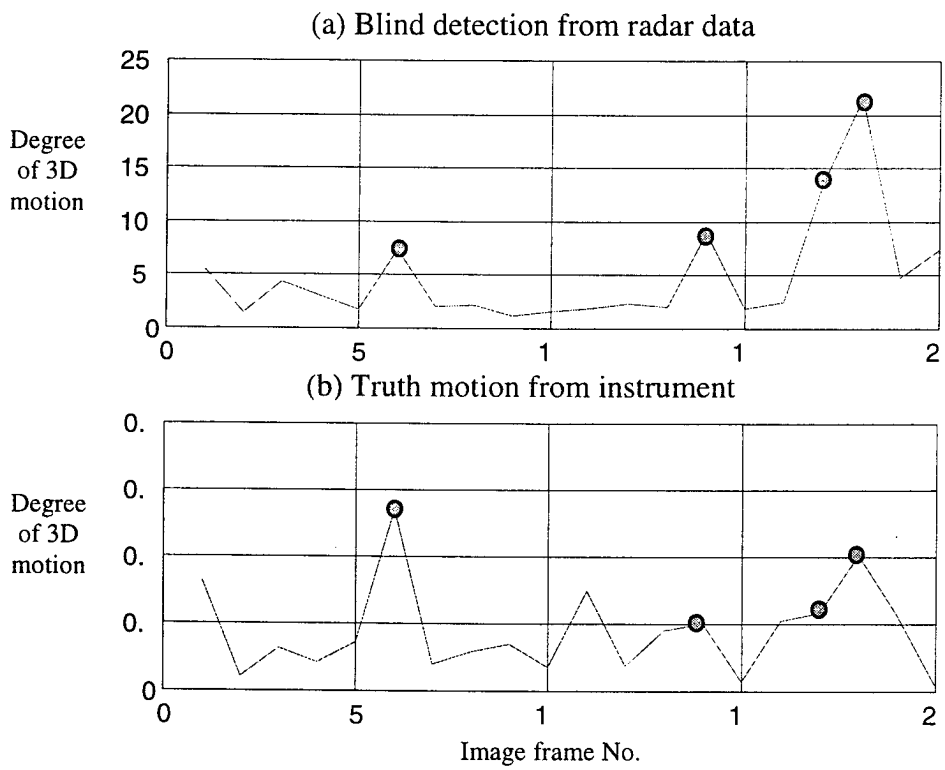

Fig. 3.1.2. Blind detection of three-dimensional motion from TIRA data. (a) Degree of three-dimensional motion over 20 image frames detected using the proposed algorithm. (b) Degree of three-dimensional motion measured from the instrument data.

3.2. 3D ISAR Image Reconstruction of a Target with Motion Data. In the previous topic, 3D target motion was treated as a problem for ISAR imaging in the sense that traditional image formation algorithm with a 2D motion model cannot accommodate the situation. The algorithm developed in 3.1 allows such intervals to be detected so that we can avoid them altogether. In fact, the presence of chaotic target motion actually provides an opportunity for 3D ISAR image formation, since radar data is available in a 2D angular aperture. In this topic, we try to devise an algorithm to form a 3D image of a target. We assume that the motion data of the target is known. 3D ISAR imaging is straightforward based on the Fourier transform of the data in the (frequency)-(azimuth)-(elevation) domain. However, the problem with the Fourier method is data availability. In practice, the available radar data is usually severely undersampled over the 2D angular aperture. Therefore, we apply the adaptive feature extraction (AFE) algorithm to attack this problem.

The adaptive feature extraction algorithm is a model-based signal processing method very similar to the AJTF engine used for ISAR motion compensation. The difference is that we use a different class of basis functions, namely, the radar return from a point scatterer with unknown cross range positions but with known motion. The two orthogonal cross range positions are obtained by a search procedure. The strongest point scatterer is extracted when the projection from the radar signal onto the basis function is maximized. We then subtract the strongest point scatterer and iterate the process for the subsequent, weaker point scatterers.

We have successfully reconstructed a 3D image of an air target from its high-resolution radar data using this algorithm. Fig. 3.2.1 shows the motion data corresponding to multiple flights of the aircraft. From Fig 3.2.1, we notice that the motion data is non-uniformly distributed in the 5 degree by 5 degree (azimuth, elevation) window. After applying the 3D AFE algorithm to the available data, we achieve the results as shown in Fig. 3.2.2. Fig. 3.2.2(a) shows the extracted 3D image. Figs. 3.2.2(b)-(d) show the projected top view, side view and front view of the target, respectively. In these images, the fuselage, two wings and the tail structures are correctly reconstructed. Through the 3D image formation, more features are made available than either the 2D ISAR image or 1D range profiles. This suggests that 3D imaging is desirable for target identification

purpose. This work also provides an important stepping stone toward the ultimate goal of blind 3D image formation without any motion data.

Fig. 3.2.1. Motion data from multiple flights of an air target.

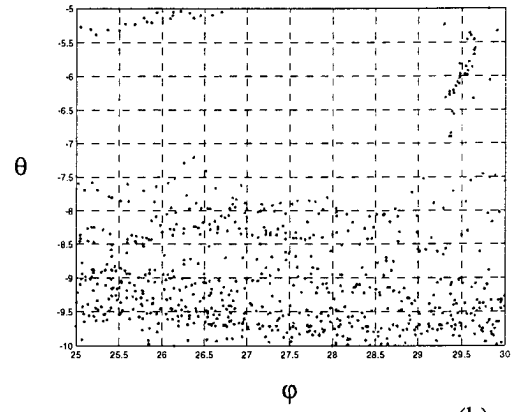

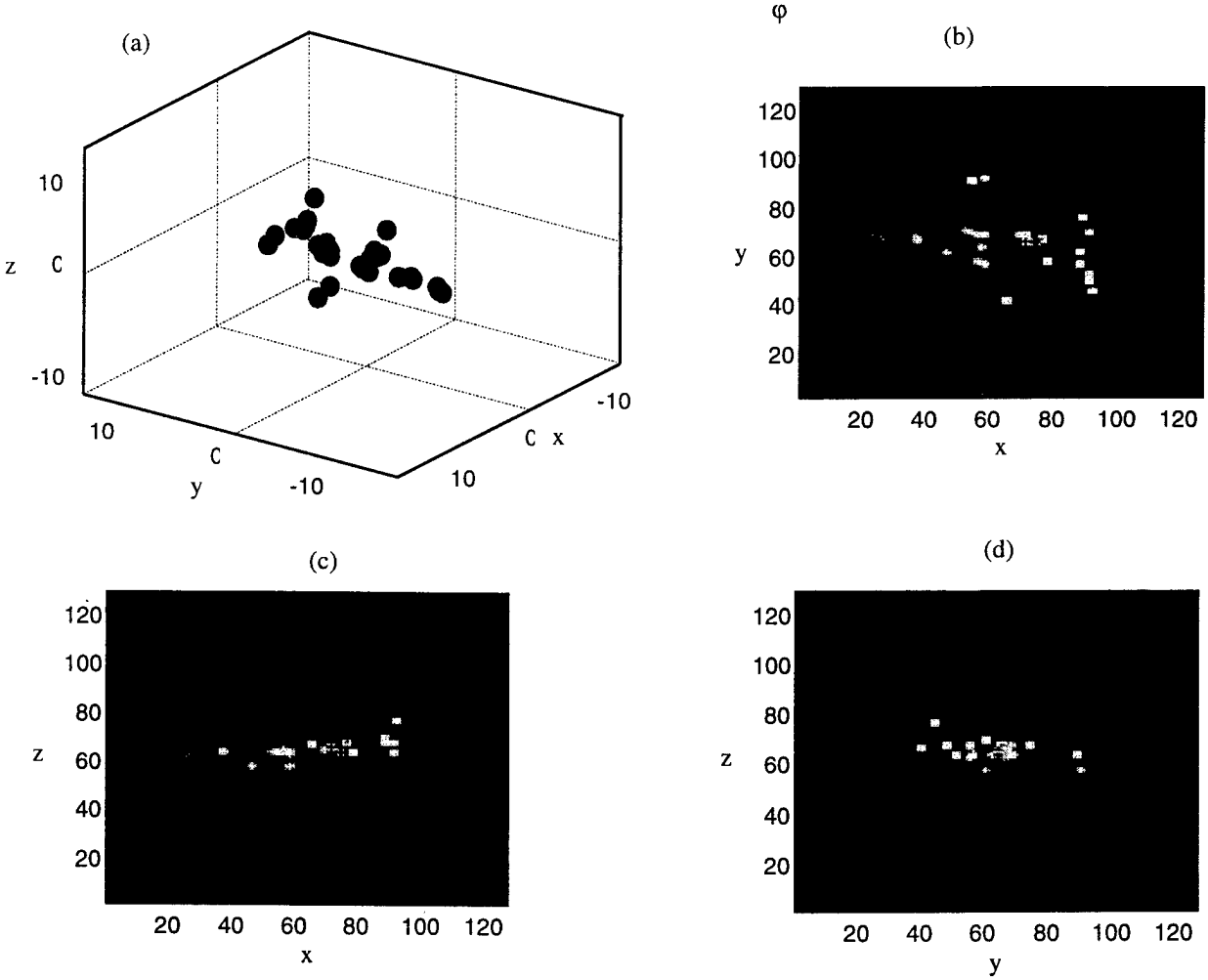

Fig. 3.2.2. Imaging result with 3D AFE applied to measurement data.
(a) Extracted 3-D Image. (b) Top view. (c) Side view. (d) Front view.

3.3. Application of Genetic Algorithms to ISAR Imaging. While the AJTF algorithm has been utilized extensively in our work, a major drawback with this method is the high computational complexity associated with the parameter search procedure. This problem becomes more acute when the order of the motion is high. We have investigated the use genetic algorithms (GA) [14] in the search procedure. In contrast to conventional optimization methods, GA is a population-based, statistical search technique. It borrows such concepts as inheritance and mutation from the biological evolution process. As a global optimization technique, GA is known to be very easy to implement and applicable to many design and inverse problems [15]. For our problem, the objective function is defined as the projection magnitude from the radar signal onto the time-frequency basis functions. Both real-coded and binary-coded GA have been implemented and the performance has been compared with results from the exhaustive search.

Point scatterer simulations are first used to test the use of GA for ISAR motion compensation. Even for a simple phase estimation problem, the objective function shows many local maxima, implying that such problems would be challenging for gradient-based local optimization techniques. Fig. 3.3.1(a) shows that the resulting phases from both the real and binary GA agree well with the original phase function. In Fig. 3.3.1(b), we compare the computational complexity of GA to exhaustive search for different orders of motion. The exhaustive search is known to have an exponential complexity of $O(exp(n))$. As expected, the resulting computation time in logarithmic scale shows up as a straight line in Fig. 3.3.1(b). Also plotted in Fig. 3.3.1(b) are the numerical results from both binary and real-coded GA. It is observed that GA has much lower complexity than exhaustive search. We also found that real-coded GA consistently achieves better accuracy than the binary-coded GA. This is because real-coded GA has the ability to search for any real values within the search range.

We have also applied GA to the NATO TIRA data. Fig. 3.3.2(a) shows the ISAR image from a particular time interval, along with the spectrogram of the radar signal at range cell 64 after third-order translation motion compensation. We see that the point scatterers in the image are not focused. The trajectory in the spectrogram is also tilted. This means that third-order motion model is not sufficient to describe the target motion. After fourth-order translation and rotational motion compensation, the result is shown in

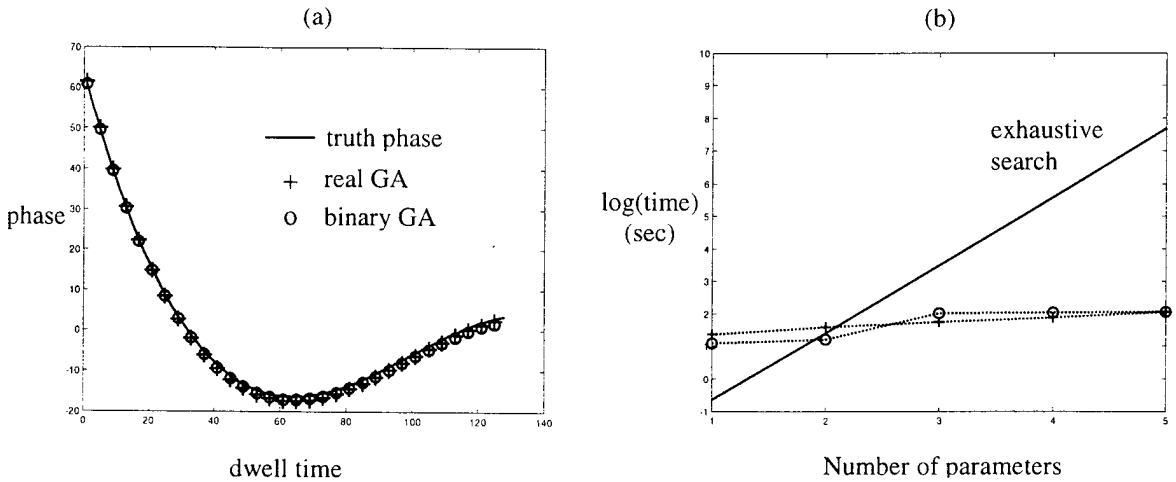

Fig. 3.3.1. (a) GA-estimated phase compared to the original truth phase. (b) Computational complexity of GA compared to exhaustive search as a function of the number of parameters.

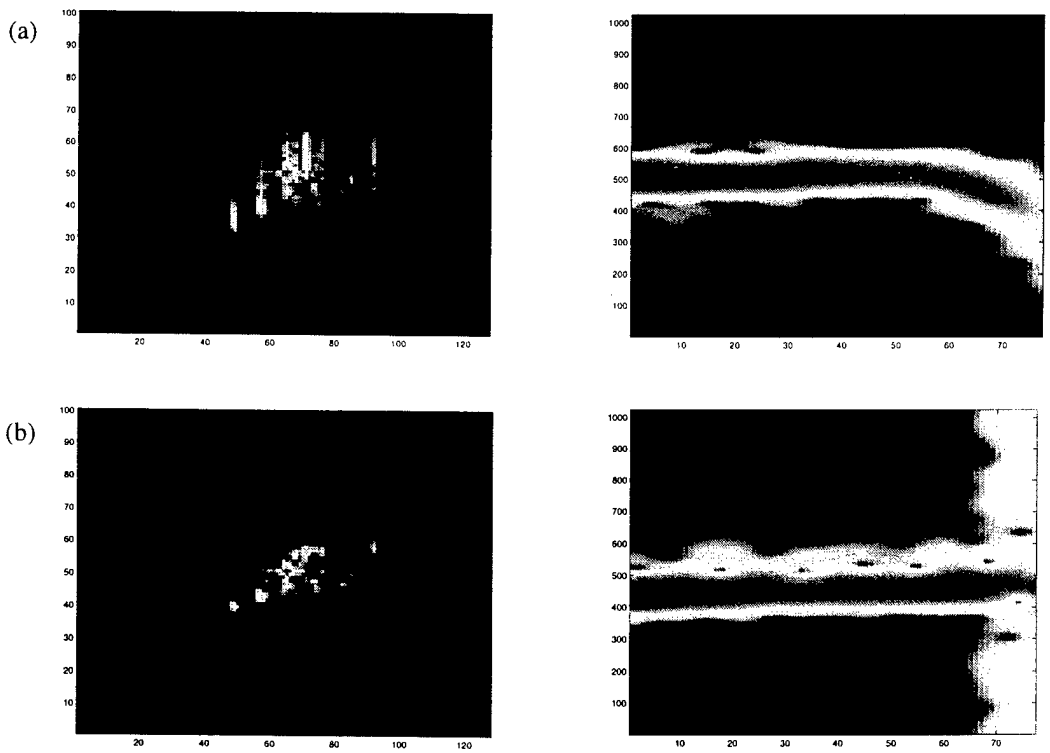

Fig. 3.3.2. (a) Image and spectrogram at range cell 64 using third-order translation motion compensation. (b) Image and spectrogram after fourth-order translation and rotational motion compensation.

Fig. 3.3.2(b). We see much better-focused point scatterers in the ISAR image. The associated spectrogram shows a straight, horizontal trajectory. While real GA took 45 seconds of computation time to obtain the correct phase, the computation time for fourth order exhaustive search is over 50 minutes. Therefore, the time savings of GA over exhaustive search becomes quite significant when the target exhibits highly irregular motion during the imaging interval.

4.1. Clutter Reduction for SAR Images Using Adaptive Wavelet Packet Transform. Synthetic Aperture Radar (SAR) images of ground targets generally consist of target features and clutters from background scattering. In automatic target recognition (ATR) applications, it is desirable to remove the clutter from the target image before ATR processing. The standard way to suppress clutter is to apply an appropriate threshold level to the whole SAR image. However, this approach assumes that the target signal-to-clutter ratio (SCR) is large enough. Otherwise this direct threshold approach results in either target feature loss or remnant clutter residue. In this work, we set out to develop a decluttering algorithm to automatically extract the target image from a SAR image by maximizing the SCR using the adaptive wavelet packet transform (AWPT) [16]. The wavelet packet basis is a generalization of the conventional wavelet basis [17] and has been applied for image compression [18] and moment matrix sparsification [19]. Our approach is to transform the SAR image to a new domain using the wavelet packet basis. Since a typical target image usually consists of point scatterers and more diffused region features, the multi-scaled wavelet basis is well suited to focus the target image. Clutter image, on the other hand, is statistically uncorrelated from pixel to pixel, and the transformed clutter image under the same set of bases remains unfocused. Therefore, we expect that the SCR can be increased by transforming the original image using an appropriately chosen set of wavelet packet basis. The cost function of our AWPT algorithm is chosen to describe how well the target signal is focused in the transform domain. An efficient basis search algorithm is implemented to find the best wavelet packet basis. Our algorithm is tested using the MSTAR SAR data set [20]. Fig. 4.1.1(a) shows an MSTAR image in which the target is a ground vehicle and the clutter is due to vegetation. There are several strong point scatters in the front of the vehicle, but the

scattering from the back part is relatively weak. Fig. 4.1.1(b) shows the result of applying the direct thresholding method to the image. Fig. 4.1.1(c) shows the decluttered image by applying the AWPT algorithm. We choose Daubechies filter with order of 6 as the wavelet filter. By visually comparing Figs. 4.1.1(b) and (c), we note that some crucial features of the target are kept in the AWPT-processed image. In both processing methods, there is some target information loss. Fig. 4.1.1(d) shows the signal-to-clutter ratio versus average target image loss for the two processing methods. It is observed that for a fixed target image loss the AWPT method always achieves a higher SCR value than the direct thresholding method. Similar results are obtained when the algorithm is applied to other MSTAR targets.

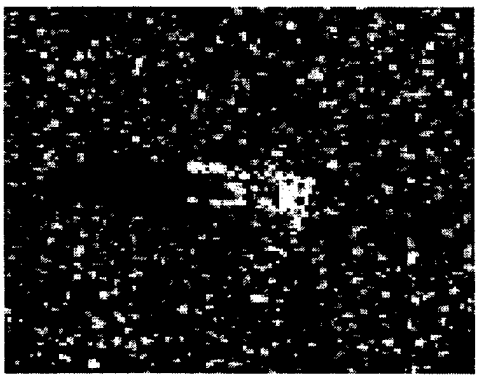

Fig. 4.1.1(a). SAR image of a ground vehicle with clutter.

Fig. 4.1.1(b). Clutter rejection using the direct thresholding method.

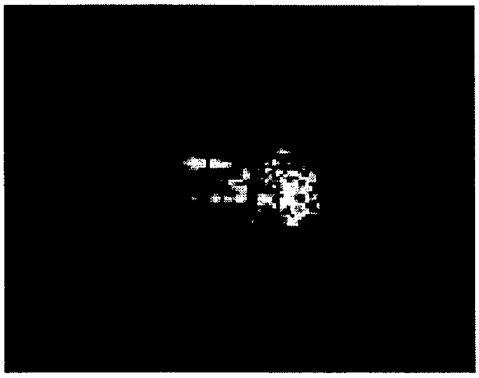

Fig. 4.1.1(c). Clutter rejection using the AWPT approach.

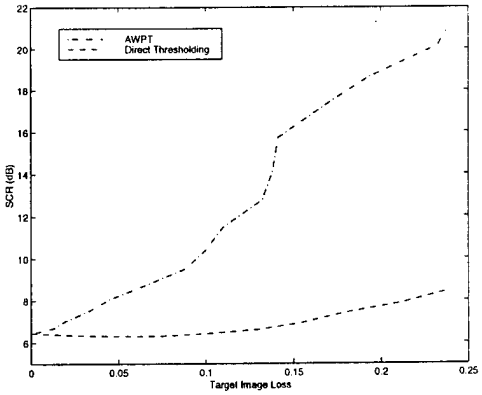

Fig. 4.1.1(d). SCR vs. target image loss for the two processing methods.

4.2. Inverse Scattering Using Genetic Algorithms. As an extension of our research into radar imaging and GA, we have also carried out an exploratory study on applying GA in conjunction with a computational electromagnetics (CEM) solver to image targets with strong multiple scattering effects. Although this is not directly related to the JTF framework, radar imaging can be considered as an approximate, linearized version of the general inverse scattering problem. Therefore, our inverse scattering work provides us with more physical insights into the radar imaging problem. It is well recognized that traditional imaging algorithms suffer from resolution limitation and image artifacts due to multiple scattering phenomena. Rigorously solving the electromagnetic inverse scattering problem, on the other hand, is much more challenging. In this work, we use GA together with a CEM solver to attack the two-dimensional inverse scattering problem. The method of moements (MoM) is used for the forward scattering computation, while GA is used as a search engine to minimize the difference between the measured data and the computed scattered fields from each candidate shape. We use the binary bitmap approach to discretize the search space. To constrain the problem, a geometrical median filter is applied to create more realizable shapes.

We have applied our algorithm to actual measurement data from the public Ipswich data set. Fig. 4.2.1(a) shows the shape and size of three metallic Ipswich objects selected for inversion, namely, the triangular cylinder, the dihedral and the circular cavity. They are labeled as Ips009, Ips004 and Ips011, respectively. We first tested the inversion algorithm using MoM-simulated field data as the input. The search area was chosen to be 15cm×15cm for Ips004 and 12cm×12cm for Ips009 and Ips011. The number of cells within this area was set to 20×20. The reconstructed results in Fig. 4.2.1(b) show the final inverted shapes of the three objects. We observe that the final shapes are in fairly good agreement with the real shapes. The dihedral and the circular cavity contain strong multiple scattering and yet their inverted shapes closely resemble the correct objects. Results for these targets were also generated using the traditional imaging method and they showed strong image artifacts due to multiple scattering.

Next, we applied the inversion algorithm to the actual measured data. Fig. 4.2.1(c) shows the final reconstruction shapes. As we can see, the inverted shape is good for the triangular cylinder, which has no multiple scattering effects. For the dihedral, the

reconstructed shape is not continuous, but is quite similar to the real object. The circular cavity shows the most discrepancy with the real shape. The exterior and the opening of the cavity are correctly inverted, while the interior part of the cavity shape is not as satisfactory. Future work on this topic should be focused on finding ways to cut down the computational load such that this method can be extended to deal with realistic 3D targets. To accelerate the GA process, better geometry constraints should be applied. In addition, the use of an approximate CEM solver such as Xpatch should be investigated to handle large 3D targets.

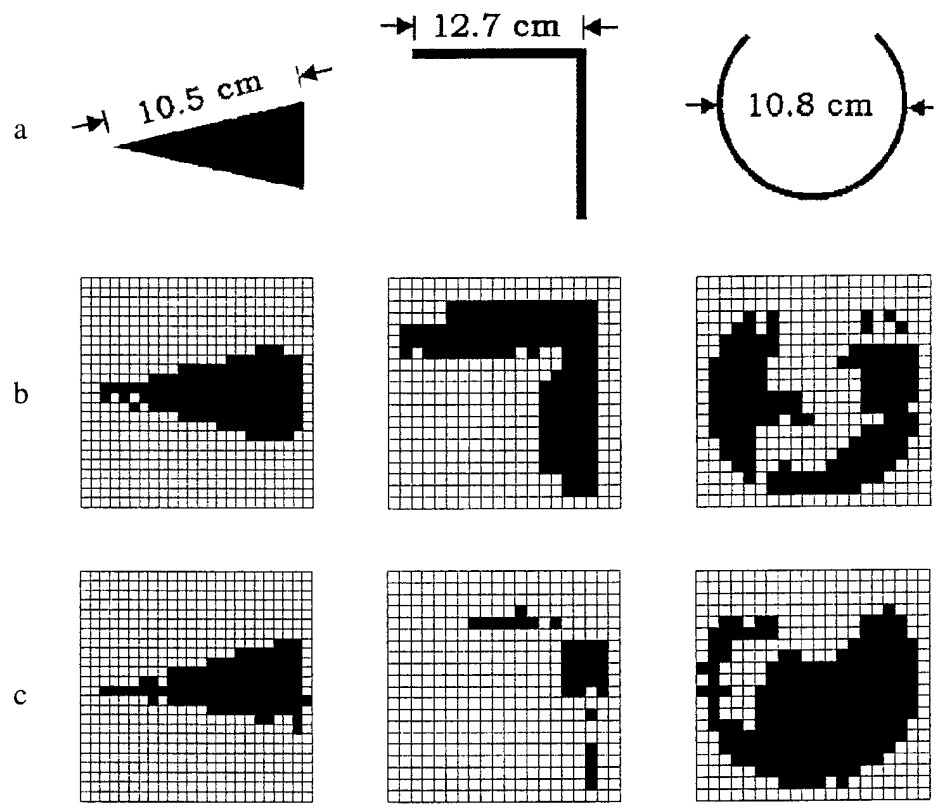

Fig. 4.2.1 Inversion of three Ipswich objects

a Real shapes of Ips009, Ips004 an Ips011
b Inversion based on MoM-simulated field
c Inversion based on measured complex field

C. FOLLOW-UP STATEMENT:

In the past three years, we have processed a number of measurement data sets and have identified several important fundamental problems in radar imaging. We have also developed a number of JTF-based algorithms to address these problems. We are currently investigating the microDoppler phenomenon, which arises in targets that violate the rigid body model of scattering. MicroDoppler can arise in situations where moving components (e.g., rotating antennas, spinning rotor blades) exist on a target, or when the target undergoes strong flexing and vibration due to motion dynamics. We have processed the "PI walking" data from the Navy APY-6 radar. We plan to continue this effort in a new proposed program to apply JTF techniques for analyzing and extracting microDoppler features and to utilize such information to improve ATR performance.

D. REFERENCES:

1. Y. Wang, H. Ling and V. C. Chen, "ISAR motion compensation via adaptive joint time-frequency technique," *IEEE Trans. Aerospace Electron. Syst.*, vol. 34, pp.670-677, Apr. 1998.

2. C. C. Chen and H. C. Andrews, "Target motion induced radar imaging," *IEEE Trans. Aerospace Electron. Syst.*, vol. 16, pp. 2-14, Jan. 1980.

3. A. Ausherman, A. Kozma, J. L. Waker, H. M. Jones and E. C. Poggio, "Developments in radar imaging," *IEEE Trans. Aerospace Electron. Syst.*, vol. 20, pp. 363-400, Apr. 1984.

4. S. Qian and D. Chen, "Signal representation using adaptive normalized Gaussian functions," *Signal Processing*, vol. 36, no. 1, pp. 1-11, Mar. 1994.

5. S. G. Mallat and Z. Zhang, "Matching pursuits with time-frequency dictionaries," *IEEE Trans. Signal Processing*, vol. 41, pp. 3397-3415, Dec. 1993.

6. R. Bhalla, H. Ling, S. W. Lee and D. J. Andersh, "Dynamic simulation of Doppler spectra of targets with rotating parts," *Microwave Optical Tech. Lett.*, vol. 7, pp. 840-842, Dec. 1994.

7. R. Bhalla and H. Ling, "A fast algorithm for simulating Doppler spectra of targets with rotating parts using the shooting and bouncing ray technique," *IEEE Trans. Antennas Propagat.*, vol. AP-46, pp. 1389-1391, Sept. 1998.

8. V. C. Chen, "Analysis of radar micro-Doppler with time-frequency transform," *Proc. of the 10th IEEE workshop on Statistical Signal and Array Processing*, pp. 463-466, Pocono Manor, PA, Aug. 2000.

9. S. Qian, D. Chen, and Q. Yin, "Adaptive chirplet based signal approximation," *Proc. ICASSP*, vol. 3, pp. 1871-1874, May 1998.

10. V.C. Chen and W. J. Miceli, "Analysis of rotation effects on ISAR imaging based on TIRA radar and ARDS data," NATO Sensors and Electronics Technology Symposium on High-Resolution Radar Techniques, Granada, Spain, March 1999.

11. U. Uschkerat, "ISAR imaging using the point scatterer model and real target motion," NATO Sensors and Electronics Technology Symposium on High-Resolution Radar Techniques, Granada, Spain, March 1999.

12. A. W. Rihaczek and S. J. Hershkowitz, "Choosing imaging intervals for identification of small ships," *SPIE Proc. on Radar Processing*, vol. 3810, Denver, CO, July 1999.

13. Private communication, A. W. Rihaczek.

14. D. E. Goldberg, *Genetic Algorithms in Search, Optimization and Machine Learning*, Addison-Wesley, Reading, MA, 1989.

15. Y. Rahmat-Samii and E. Michielssen (eds.), *Electromagnetic Optimization by Genetic Algorithms*, John Wiley & Sons, New York, NY, 1999.

16. M. V. Wickerhauser, *Adapted Wavelet Analysis from Theory to Software,* A.K.Peters, Wellesley, Mass. 1994.

17. C. K. Chui, *An Introduction to Wavelets.* Academic Press, New York, 1992.

18. R. R. Coifman, Y. Meyer, and M. V. Wickerhauser, "wavelet analysis and signal processing." in *Wavelets and Their applications,* pp. 153-178, Jones and Barlett, Boston, 1992.

19. H. Deng and H. Ling, "Fast solution of electromagnetic integral equations using adaptive wavelet packet transform," *IEEE Trans. Antennas Propagat.*, vol. AP-47, pp. 674-682, Apr. 1999.

20. MSTAR SAR data set, clutter and targets, collected by Sandia National Lab, released by DARPA, Apr. 1997.

E. PUBLICATIONS:

I. Books

1. V. C. Chen and H. Ling, *Time-Frequency Transforms for Radar Imaging and Signal Analysis*, 250 pages, Artech House, to be published in Dec. 2001.

II. LIST OF JOURNAL ARTICLES (ONR supported in whole or in part)

1. Y. Wang, H. Ling and V. C. Chen, "ISAR motion compensation via adaptive joint time-frequency technique," *IEEE Trans. Aerospace Electronic Sys.*, vol. AES-34, pp. 670-677, Apr. 1998.

2. R. Bhalla and H. Ling, "A fast algorithm for simulating Doppler spectra of targets with rotating parts using the shooting and bouncing ray technique," *IEEE Trans. Antennas Propagat.*, vol. AP-46, pp. 1389-1391, Sept. 1998.

3. V. C. Chen and H. Ling, "Joint time-frequency analysis for radar signal and image processing," *IEEE Signal Processing Mag.*, Special Issue on Joint Time-Frequency Analysis, vol. 16, pp. 81-93, Mar. 1999.

4. Y. Wang and H. Ling, "Adaptive ISAR image construction from unevenly undersampled data," *IEEE Trans. Antennas Propagat.*, vol. AP-48, pp. 329-331, Feb. 2000.

5. H. Deng and H. Ling, "Clutter reduction for synthetic aperture radar imagery based on adaptive wavelet packet transform," *Progress in Electromag. Research*, vol. 29, pp. 1-23, Mar. 2000.

6. J. Li and H. Ling, "3D ISAR image reconstruction of a target with motion data using adaptive feature extraction," *J. Electromag. Waves Applications*, vol. 15, pp. 1571-1587, Nov. 2001.

7. J. Li, H. Ling and V. C. Chen, "An algorithm to detect the presence of 3D target motion from ISAR data," accepted for publication in *Multidimensional Systems and Signal Processing*, special issue on Radar Signal Processing and Its Applications, Aug. 2001.

8. J. Li and H. Ling, "Use of genetic algorithms in ISAR imaging of targets with irregular motions" submitted for publication in *IEEE Trans. Aerospace Elec. Sys.*, Sept. 2001.

9. Y. Zhou and H. Ling, "Electromagnetic inversion of Ipswich objects using the genetic algorithm," submitted for publication in *Electron. Lett.*, Oct. 2001.

III. LIST OF CONFERENCE PROCEEDINGS (ONR supported in whole or in part)

1. Y. Wang, H. Ling and V. C. Chen, "ISAR imaging of targets with fast rotating parts using adaptive joint time-frequency processing," SPIE AeroSense '98, Wavelet Applications, Orlando, FL, Apr. 1998.

2. H. Ling, "Joint time-frequency processing of electromagnetic backscattered data," SPIE AeroSense '98, Wavelet Applications, Orlando, FL, Apr. 1998.

3. Y. Wang and H. Ling, "ISAR image formation from unevenly undersampled data using adaptive feature extraction," International IEEE AP-S Symposium, pp. 350-353, Atlanta, GA, June 1998.

4. Y. Wang, H. Ling and V. C. Chen, "ISAR feature extraction from targets with rotating components using adaptive joint time-frequency processing," URSI National Radio Science Meeting, p. 23, Atlanta, GA, June 1998.

5. Y. Wang, H. Ling and V. C. Chen, "Application of adaptive joint time-frequency processing to ISAR image enhancement and Doppler feature extraction for targets with rotating parts," SPIE 43rd Annual Meeting, Radar Processing, Technology, and Applications, pp. 156-163, San Diego, CA, July 1998.

6. H. Ling, Y. Wang, J. Li and R. Bhalla, "ISAR image formation of TIRA data using adaptive joint time-frequency processing," NATO Sensors and Electronics Technology Symposium on High Resolution Radar Techniques, Granada, Spain, Mar. 1999.

7. H. Deng and H. Ling, "Clutter reduction for synthetic aperture radar images using adaptive wavelet packet transform," International IEEE AP-S Symposium, pp. 1780-1783, Orlando, FL, July 1999.

8. R. Bhalla, H. Ling and J. Schmitz, "Dynamic signature simulation using the shooting and bouncing ray technique," URSI National Radio Science Meeting, p. 272, Orlando, FL, July 1999.

9. J. Li, Y. Wang, R. Bhalla, H. Ling and V. C. Chen, "Comparison of high-resolution ISAR imageries from measurement data and synthetic signatures," SPIE 44th Annual Meeting, Radar Processing, Technology, and Applications, vol. 3810, pp. 170-179, Denver, CO, July 1999.

10. H. Ling and J. Li, "Application of adaptive joint time-frequency processing to ISAR image formation," 10th IEEE Workshop on Statistical Signal and Array Processing, pp. 476-479, Pocono Manor, PA, Aug. 2000.

11. J. Li and H. Ling, "ISAR motion detection and compensation using genetic algorithms," SPIE AeroSense '01, Radar Sensor Technology, pp. 380-388, Orlando, FL, Apr. 2001.

12. J. Li and H. Ling, "3-D radar image formation from undersampled aspect data using adaptive feature extraction," URSI National Radio Science Meeting, p. 289, Boston, MA, July 2001.

13. Y. Zhou and H. Ling, "Shape reconstruction of metallic objects with strong multiple scattering using genetic algorithm," URSI National Radio Science Meeting, p. 287, Boston, MA, July 2001.

14. J. Li and H. Ling, "MicroDoppler feature extraction from ISAR data using adaptive chirplet representation," submitted to IEEE 2002 Radar Conference, Sept. 2001

IV. LIST OF RELATED PRESENTATIONS

1. "Electromagnetic signature simulation and feature extraction for radar target identification," Naval Research Laboratory, Radar Division Seminar, Washington DC, July 8, 1998.

2. "Signature exploitation research at UT-Austin," Mission Research Corporation, Dayton, OH, Oct. 28, 1998.

3. "Modeling and simulation of scattering and radiation phenomena using scattering centers and radiation centers," Sensor Technologies Integration Laboratory, Air Force Wright Lab, Dayton, OH, Oct. 29, 1998.

4. "Electromagnetic signature simulation and feature extraction for radar target identification," University of Illinois, Signal Processing Seminar, Champaign, IL, Feb. 3, 1999.

5. "Radar image simulation: solving Maxwell's equations for radar target identification," University of Illinois, ECE Department Graduate Seminar, Champaign, IL, Feb. 4, 1999.

6. "Evaluation of Apatch – a platform radiation code based on the shooting and bouncing ray technique," Navy DD-21 Program Electromagnetic Software Evaluation Meeting, Navy SPAWAR System Center, San Diego, CA, Sept. 27, 1999.

7. "Fast postprocessing algorithms for fast CEM solvers," 2000 Electromagnetics Code Consortium Annual Meeting, Boeing Phantomworks, St. Louis, MO, May 9, 2000.

8. "Application of model-based signal processing for antenna design, placement and optimization," Navy H-Infinity Program Workshop, US Naval Academy, Annapolis, MD, Oct. 26, 2000.

9. "Joint time-frequency processing of NATO radar data," kickoff meeting of the Naval International Cooperative Opportunities in Science and Technology (NICOP) program on Time-Frequency ISAR, London, England, Mar. 29, 2001.

10. "Joint time-frequency processing of NATO radar data," NATO Task Group 22 Meeting on Generation of Synthetic Data Bases for Non-Cooperative Air Target Identification, Dayton, OH, Oct. 16, 2001.

V. LIST OF THESES AND DISSERTATIONS

Ph.D.

Y. Wang, "Radar signature prediction and feature extraction using advanced signal processing techniques," Aug. 1999.

H. Deng, "Applications of wavelet packet bases to computational electromagnetics and radar imaging," Aug. 2000.

VI. CONTRACTS AND GRANTS

H. Ling, "Advanced studies of electromagnetic scattering," Wright-Patterson Air Force Base (via DEMACO, Inc.), June 1, 1995 - August 1, 1998.

H. Ling, "Advanced research and development for the MSTAR prediction module," Defense Advanced Research Project Agency (via DEMACO, Inc.), June 1, 1995 - December 31, 1998.

H. Ling, "MURI center for computational electromagnetics research," Air Force Office of Scientific Research (via Univ. of Illinois), December 15, 1995 - May 31, 2001.

W. Vogel, H. Ling and H. Foltz, "An automated cellular base-station siting tool for urban locations," Texas Advanced Technology Program, January 1, 1996 - August 31, 1998.

R. Chen and H. Ling, "Si CMOS process-compatible optical vias for intra- and inter-multi-chip-module optoelectronic interconnects," Texas Advanced Technology Program, January 1, 1996 - August 31, 1998.

H. Ling, "Application of model-based signal processing methods to computational electromagnetics simulators," Office of Naval Research, December 1, 1997 - November 30, 2000.

R. Chen and H. Ling, "Si MOS process-compatible optical interconnects and applications," Texas Advanced Technology Program, January 1, 1998 - December 31, 1999.

H. Ling, "Radar image enhancement, feature extraction and motion compensation using joint time-frequency techniques," Office of Naval Research, April 15, 1998 - September 30, 2001.

H. Ling, "Moving target modeling and simulation," Air Force Research Laboratory (via DEMACO, Inc.), October 1, 1998 - April 30, 1999.

H. Ling, "Electromagnetic scattering from periodic surfaces," Lockheed Martin Corporate Grant, November 15, 1998 - December 31, 1999.

D. T. Jaffe and H. Ling, "High index grisms for mid-infrared spectroscopy," NASA, June 1, 1999 - May 31, 2001.

G. Xu, H. Ling and H. D. Foltz, "Development of wideband vector channel models and testbed for 3rd generation wireless mobile systems," Texas Advanced Technology Program, January 1, 2000 - August 31, 2002.

H. Ling, "Application of model-based signal processing and genetic algorithms for shipboard antenna design, placement and optimization," Office of Naval Research, December 1, 2000 - November 30, 2002.

F. INTERACTIONS/COLLABORATIONS WITH NAVY SCIENTISTS:

Our key collaborator in this program is Dr. Victor Chen of Naval Research Laboratory. Our interactions with Dr. Chen include the exchange of data and algorithms. We have also co-authored a number of publications and an upcoming book on JTF processing. It is expected that our close collaboration will continue since it provides an excellent way for us to stay informed of the problems of interest to the Navy and for us to quickly disseminate our research to the Navy labs. During the past three years, the PI visited NRL a number of times and held a seminar and technical discussions with scientist within the Radar Divison.

The PI participated in an electromagnetic software evaluation meeting held at SPAWAR for the Navy's DD-21 program on Sept. 27, 1999. The PI presented an evaluation of the high-frequency code Apatch for characterizing antenna-platform interactions during the meeting. He also had technical discussions with Dr. William Pala of NRL, Dr. Jeffrey Ho of SPAWAR, and other scientists from government, industry and academic organizations.

Our close association with the Joint Services Electromagnetics Code Consortium (EMCC) is another mechanism where we interact with Navy scientists, including Dr. Helen Wang and Dr. Brett Borden of Naval Air Warfare Center, China Lake, CA and Dr. John Asvestas of NAVAIR, Patuxent River, MD.

G. NEW DISCOVERIES, INVENTIONS, OR PATENT DISCLOSURES:

None.

H. HONORS AND AWARDS:

Dr. Ling was elected to IEEE Fellow for 1999 for his "contribution to the development of radar signature prediction and feature extraction techniques." In 2001, he was named the L. B. Meaders Professor in Engineering at The University of Texas.

APPENDIX

Selected Publications Supported by ONR

Research Grant N00014-98-1-0615

Journal Article [6]

J. of Electromagn. Waves and Appl., Vol. 15, No. 11, 1571–1587, 2001

3D ISAR IMAGE RECONSTRUCTION OF A TARGET WITH MOTION DATA USING ADAPTIVE FEATURE EXTRACTION

J. Li and H. Ling

Department of Electrical and Computer Engineering
The University of Texas at Austin
Austin, TX 78712-1084, USA

Abstract—In this paper, three-dimensional (3D) inverse synthetic aperture radar (ISAR) image reconstruction with known motion data is studied. In traditional two-dimensional (2D) ISAR imaging, a 2D point scatterer model is adequate to consider the target rotation motion with a fixed rotational axis. However, target motions with a varying rotational axis are sometimes encountered in real situations. Under such cases, the use of a 3D point scatterer model is necessary for 3D ISAR image reconstruction. An adaptive feature extraction algorithm is proposed to reconstruct the 3D image of a target with non-uniformly undersampled radar data over the azimuth and elevation aperture. Simulation results based on actual motion data of air targets demonstrate the effectiveness of the algorithm.

1 Introduction

2 3D Point Scatterer Model

3 Adaptive Feature Extraction Algorithm

4 Results

4.1 Testing on the AFE Algorithm

4.2 Resolution and Sensitivity of the AFE Algorithm

4.3 Aircraft Imaging with Real 3D Motion Data

5 Conclusions

Acknowledgment

References

1. INTRODUCTION

Inverse synthetic aperture radar (ISAR) has been identified as an effective tool for target recognition [1, 2]. In the ISAR problem, the radar is stationary and collects back-scattering data from a moving target. The geometry of such a problem is shown in Figure 1, where the target rotates with azimuth angle φ and elevation angle θ and the x-axis is the radar line of sight (LOS). In traditional ISAR imaging, we assume that the target rotates with a fixed rotational axis during the image formation interval. This motion is termed two-dimensional (2D) motion, since the target motion is confined to a 2D plane. Under this case, only 2D ISAR images can be obtained.

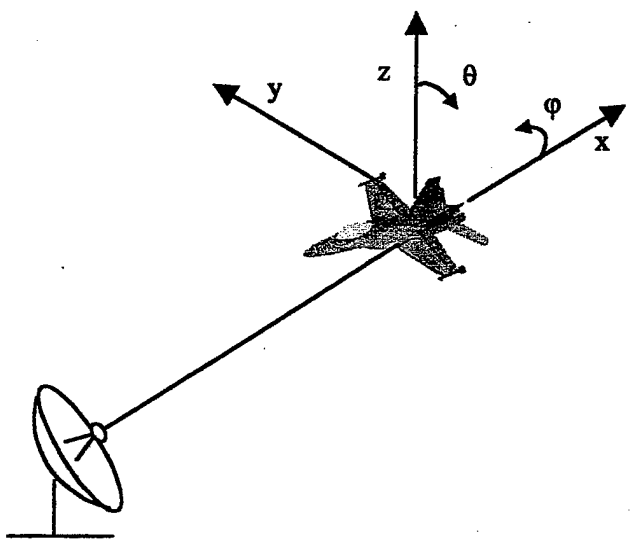

Figure 1. Geometry of an ISAR imaging problem.

When the target has a varying rotational axis during the imaging interval, the target motion is termed three-dimensional (3D) motion. This can occur on a maneuvering target. Three examples of 3D target motion are shown in Figure 2. Figure 2(a) shows a slight deviation from a 2D motion. This can occur when an aircraft undergoes a well-controlled maneuver during the imaging interval [3]. Figure 2(b) shows a severe wave-like 3D motion. This kind of motion is typical of ship targets due to ocean wave modulation [4]. Figure 2(c) shows the target motion data from multiple flight paths. Although each flight path obeys 2D motion, the cumulative data over the angular aperture appear to be 3D.

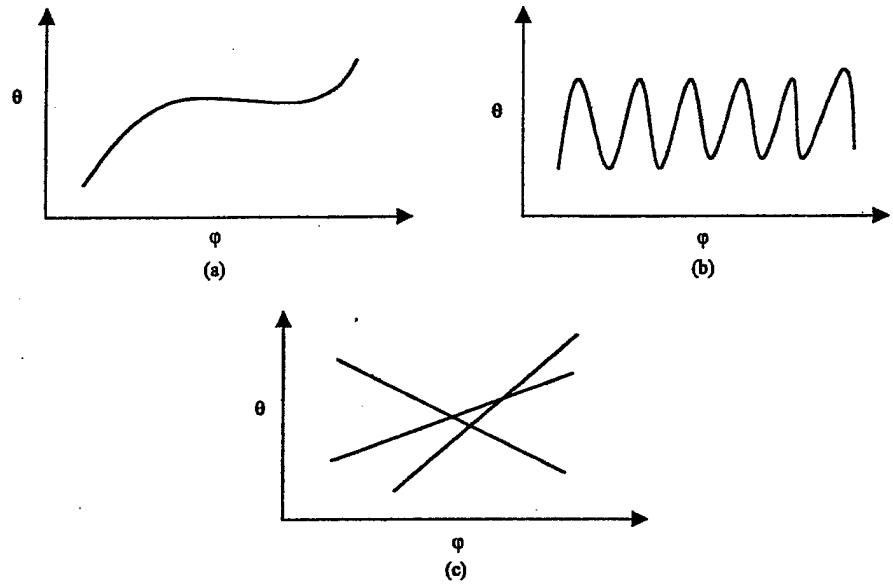

Figure 2. Possible 3D motions encountered in real ISAR data collection. (a) Slight 3D motion deviating from 2D motion. (b) Severe wave-like 3D motion. (c) Multiple flight paths of 2D motion.

For the standard 2D ISAR imaging problem, 3D motion of a target is considered undesirable and its detrimental effect on the 2D ISAR imaging result has been analyzed in [5]. To date, there is no good method to deal with how to image in the presence of unknown 3D motion [6]. However, when the motion data is known, there is an opportunity to produce a 3D image. With the known motion data, the collected radar data is available in the (frequency)-(azimuth)-(elevation) domain. Based on the 3D point scatterer model, 3D ISAR imaging is straightforward based on the Fourier transform.

The problem for 3D ISAR image formation with the Fourier transform is data availability. Governed by the Nyquist sampling theorem, the Fourier transform method requires data that is dense enough in the angular aperture. By examining Figure 2, it is clear that the available radar data in practice are severely undersampled over the 2D angular aperture. This makes the Fourier transform method unsuitable for the 3D ISAR imaging problem.

In this paper, we set out to reconstruct the 3D ISAR image of a target assuming the 3D motion of the target is known. Similar topics have been reported in [7–9]. In [7], a mosaic 3D image is produced from many 2D images formed using a super-resolution algorithm. In [8], the

target height is reconstructed using multiple cuts of elevation data. In [9], a relaxation-based algorithm is used to address the so-called curvilinear SAR problem.

Our approach is to use an adaptive feature extraction algorithm based on a general 3D point scatterer model. It is an extension of our previous work in [10], where only 2D motion is considered. Here, we consider both the case of severe and slight 3D motions. When there is severe 3D motion of the target, our goal is to form a 3D ISAR image. When there is only slight 3D motion that deviates from 2D motion, our goal is to achieve a better 2D ISAR image.

This paper is organized as follows. In Section 2, the 3D point scatterer model is introduced to account for 3D target motion. The adaptive feature extraction algorithm is then described in Section 3. In Section 4, we show the advantages of this algorithm with some simple point scatterer simulations and discuss the limitations of the algorithm. We then apply the algorithm to reconstruct 3D images of an aircraft from realistic ISAR motion data. Conclusions are given in the final section.

2. 3D POINT SCATTERER MODEL

A 2D point scatterer model is usually used in traditional ISAR imaging [1, 2]. In this model, the target consists of ideal point scatterers. After range compression, the radar data can be expressed as

$$E(t_D) = \sum_{i=1}^{Ns} \sigma_i \exp\left\{-j\frac{4\pi f_0}{c}[x_i + y_i\varphi(t_D)]\right\} \tag{1}$$

where f_0 is the radar center frequency and t_D is the dwell time. x and y represent the target range and cross-range positions, respectively. The target is assumed to consist of N_s point scatterers, with the ith point scatterer depicted by position $(x_i,\ y_i)$ and strength σ_i.

The above model is valid only if the target rotational motion is confined to a 2D plane and can thus be described in terms of only one angular parameter φ. When there is 3D motion of the target, a more general 3D model is required:

$$E(t_D) = \sum_{i=1}^{Ns} \sigma_i \exp\left\{-j\frac{4\pi f_0}{c}[x_i + y_i\varphi(t_D) + z_i\theta(t_D)]\right\} \tag{2}$$

In the above expression, a third coordinate z of the target is included to represent the third dimension of the target and another independent angular motion parameter θ is introduced to describe the 3D motion.

If we know the target angular motion parameters (θ, ϕ) as a function of dwell time, then the radar data is actually in the (azimuth)-(elevation) domain. Therefore, we can rewrite equation (2) as

$$E(\varphi, \theta) = \sum_{i=1}^{Ns} \sigma_i \exp\left\{-j\frac{4\pi f_0}{c}[x_i + y_i\varphi + z_i\theta]\right\} \tag{3}$$

Based on (3), we can see that if both θ and φ are evenly sampled over the 2D angular aperture, we can use a 2D fast Fourier transform with respect to θ and φ to form a 3D radar image in the range x and cross ranges y and z domain. If the data is unevenly sampled yet dense enough, we can still use the Fourier transform to process the radar data. However, when the available data is highly undersampled as those shown in Figure 2, the Fourier transform method will not produce any meaningful results. To overcome the undersampling problem, the so-called adaptive feature extraction algorithm is proposed in the next section.

3. ADAPTIVE FEATURE EXTRACTION ALGORITHM

Adaptive feature extraction (AFE) is a model-based signal processing method that has been used in a previous work for 2D ISAR imaging [10]. It is similar to CLEAN [11] and the matching pursuit algorithm [12]. After range alignment, we assume that the range position is resolved via range compression. The two cross range dimensions are obtained by applying AFE based on the 3D point scatterer model to the radar data within a range bin. The basic idea is to extract the strongest point scatterer first. Then the response from this point scatterer is subtracted from the total signal. The process is then iterated for the remaining point scatterers.

Within a particular range bin, for every possible point scatterer position (y, z), we construct a basis function as the radar signal from a unit point scatterer located at position (y, z) using the model depicted in (3)

$$h(t_D) = e^{-j\frac{4\pi f_0}{c}[y\phi(t_D)+z\theta(t_D)]} \tag{4}$$

To find the strongest point scatterer within the range cell, we search for the basis function that gives rise to the maximum projection from the radar data $E(t_D)$ onto the basis. That is, we can find the position of the strongest point scatterer (y_m, z_m) as

$$\{y_m, z_m\} = \arg\max |< E(t_D), h(t_D) >| \tag{5}$$

where the projection is defined as

$$< E(t_D), h(t_D) >= \int E(t_D)h^*(t_D)dt_D \tag{6}$$

After we find the position of the strongest point scatterer, the strength σ_m of that point scatterer is simply the projection from the radar data onto the chosen basis function:

$$\sigma_m =< E(t_D), e^{-j\frac{4\pi f_0}{c}[y_m\phi(t_D)+z_m\theta(t_D)]} > \tag{7}$$

Once we have found the contribution from the strongest point scatterer to the radar signal, it is denoted as

$$E_m = \sigma_m e^{-j\frac{4\pi f_0}{c}(y_m\phi+z_m\theta)} \tag{8}$$

We then subtract E_m from E to find the residual signal:

$$E_{m+1} = E - E_m \tag{9}$$

Finally, this process is iterated to find the subsequent point scatterers one at a time until the energy of the residual signal falls below a preset threshold.

To summarize, the steps in the adaptive feature extraction algorithm are as follows:

Step 1. Set up the searching space for both y and z.

Step 2. Search for maximum projection from the present signal onto the searching space. The two cross range positions and the strength of the strongest point scatterer within the range bin are determined.

Step 3. Remove the response of the point scatterer from the radar signal.

Step 4. Repeat steps 2 and 3 until the energy of the residual signal falls below a predefined threshold.

Step 5. Repeat the above procedures for other range bins.

For this work, the exhaustive search method is used in step 2. It is guaranteed to produce a global maximum for the projection. To further save computation time, we have also explored the use of genetic algorithm instead of the exhaustive search for more efficient global optimization [13].

4. RESULTS

To demonstrate the use of AFE for ISAR image formation of a target with 3D motion, we first compare the result against that from the

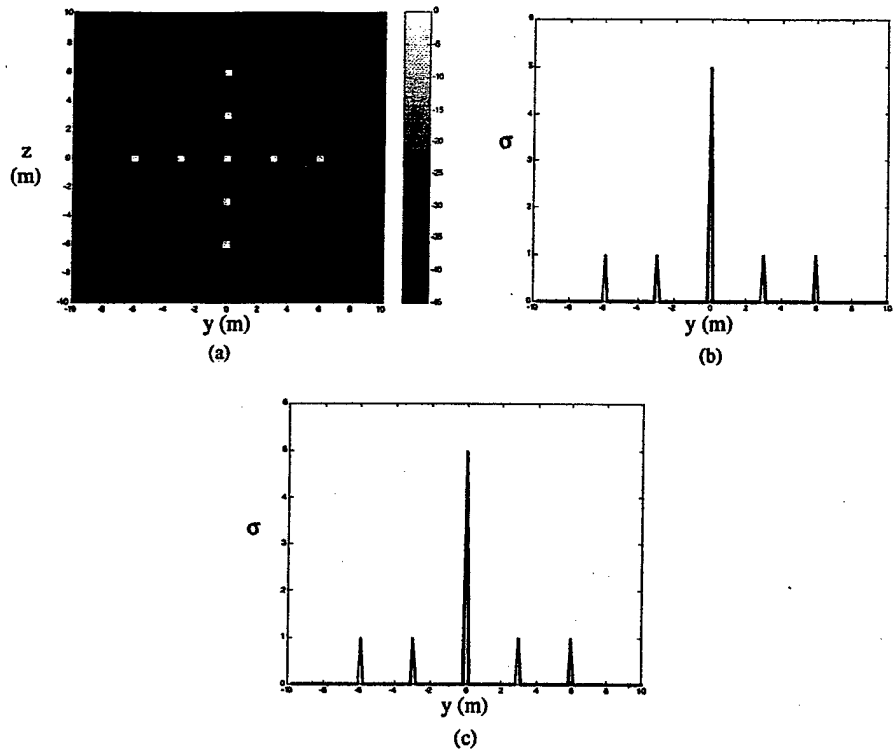

Figure 3. Original 9 point scatterers within in one range cell. (a) $(y,\ z)$ distribution. (b) y projection. (c) z projection.

Fourier transform. We then study the resolution and noise sensitivity of the algorithm. After establishing the advantages and limitations of the AFE algorithm, we reconstruct 3D images from some simulated radar data based on real motion data from an air target.

4.1. Testing on the AFE Algorithm

To test the algorithm, we consider radar data from a fixed range cell and study how to resolve the two cross range dimensions using AFE. A target consisting of nine point scatterers of equal strength in the $(y,\ z)$ plane at a fixed range is shown in Figure 3(a). The two projections of the point scatterers along the y and the z axes are shown in Figures 3(b) and 3(c) respectively. With the point scatterer model and assumed 3D motion, we generate simulated radar data based on equation (2). The center frequency is 10 GHz and the bandwidth is 1 GHz in our simulation. We then apply the AFE algorithm to the simulated radar

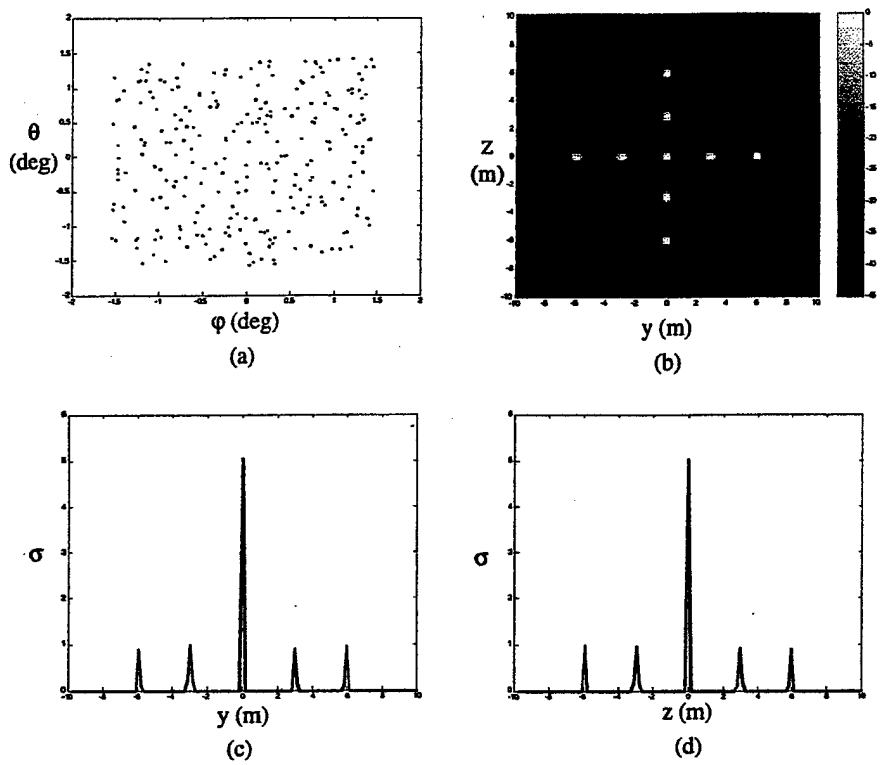

Figure 4. Reconstruction result using AFE. (a) Motion data in a 3 deg by 3 deg aperture. (b) $(y,\ z)$ image. (c) y projection. (d) z projection.

data.

The first case considered is severe 3D motion as shown by the azimuth-elevation data in Figure 4(a). In this figure, 256 data points over a 3-degree azimuth by 3-degree elevation aperture are randomly distributed. The AFE reconstructed image in the $(y,\ z)$ plane is illustrated in Figure 4(b). The two projections along the y and the z axes are shown in Figures 4(c) and 4(d) respectively. We can see that they agree well with the reference images in Figures 3(a)–3(c). The small errors are due to finite position resolution in the searching space.

Next, we generate the image via the Fourier transform. The result of the $(y,\ z)$ image is shown in Figure 5. It is obtained by a brute-force Fourier transform over the non-uniform angular aperture. The sidelobes are so high that the positions of the point scatterers cannot

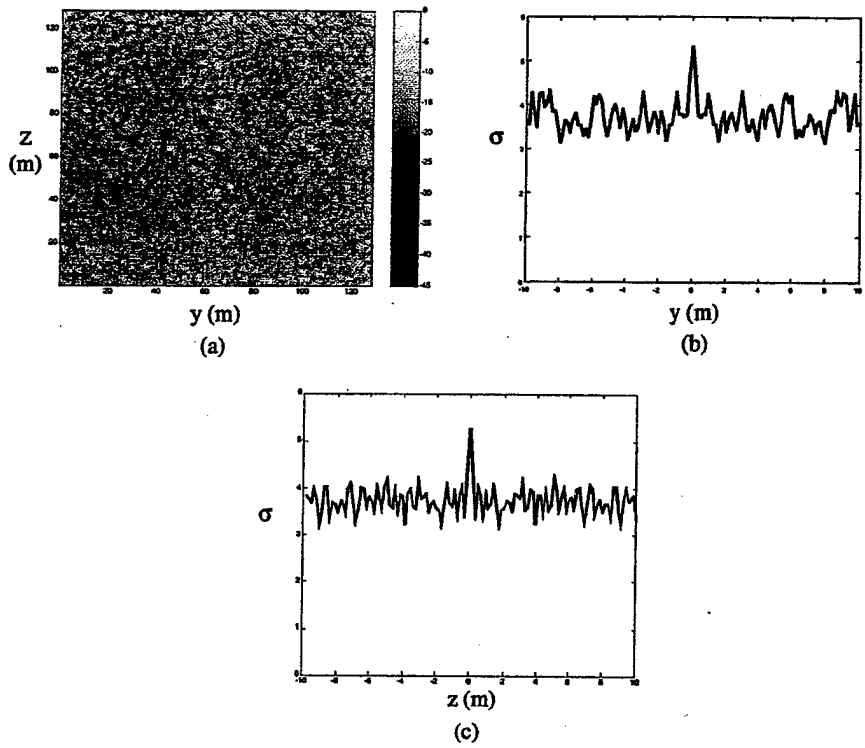

Figure 5. Reconstruction result using the Fourier transform. (a) $(y,\ z)$ image. (b) y projection. (c) z projection.

be easily recognized in the $(y,\ z)$ image or the two projections. This is due to the large aliasing effect associated with the undersampled data. The Nyquist sampling in angle is about 0.07 degree, while the actual average sampling of the data is about 0.19 degree. We cannot expect a good image to be obtained by the Fourier transform method. Therefore, AFE is a much better choice than the Fourier transform to process the undersampled radar data at hand.

The second case considered is slight 3D motion as shown in Figure 6(a). The motion parameters in this figure are taken from the real motion data of an in-flight aircraft. The azimuth and elevation angles are obtained through coordinate transformation of the original roll, yaw and pitch motions of an instrumented aircraft. As we can see, there is a slight 3D motion that deviates from the idealized 2D motion, which should be a line in the θ-φ aperture. In this case, we apply AFE based on both the correct 3D motion model in (2) and the approximate

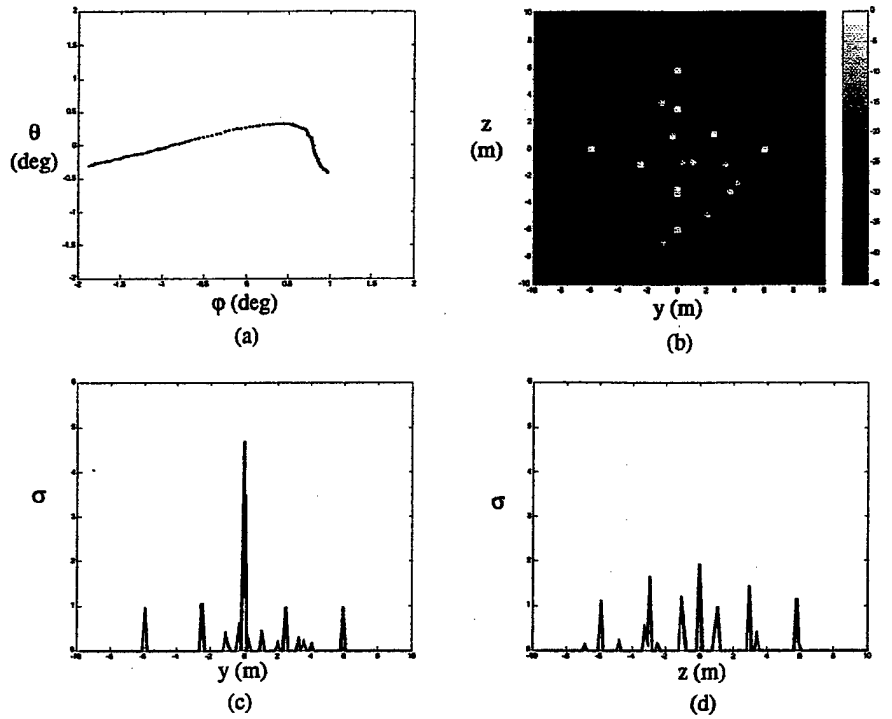

Figure 6. AFE reconstruction from data with a slight 3D motion. (a) Motion data. (b) $(y,\ z)$ image. (c) y projection. (d) z projection.

2D motion model in (1). In the former case, the AFE search is over the $(y,\ z)$ space, while in the latter case, the search is a one-dimensional one over the y dimension only. Figure 6(b) shows the $(y,\ z)$ image resulting from the 3D motion model. The two projections along the y and the z axes are shown in Figures 6(c) and 6(d). At first glance, the image in Figure 6(b) does not look like the original image in Figure 3(a) at all. However, we can see that the y projection in Figure 6(c) agrees fairly well with the original y projection in Figure 3(b). On the other hand, the z projection in Figure 6(d) is very different from the original z projection in Figure 3(c). The reason for the poor performance is that the variation in φ is only one-fifth of the variation in θ, which makes the image resolution in z much lower than the image resolution in y. The resolution of the AFE algorithm will be discussed in more detail in 4.2.

Figure 7 shows the AFE result based on the 2D motion model. Only the y projection is available from the one-dimensional AFE

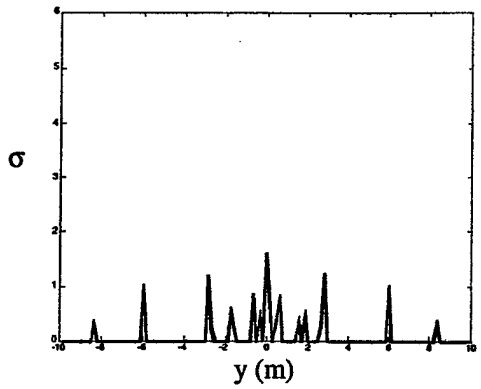

Figure 7. AFE reconstruction from data with a slight 3D motion based on a 2D motion model.

search. The y positions from this figure do not reflect the true y positions of the 9 point scatterers shown in Figure 3(b). The mistake here is due to model mismatch. Although the variation in the elevation angle θ is only one-fifth of the variation in the azimuth angle φ, this slight 3D motion cannot be ignored in processing the radar data. Therefore, the full 3D motion model in conjunction with the AFE algorithm is needed for image formation in the presence of 3D motions.

4.2. Resolution and Sensitivity of the AFE Algorithm

As we saw in the last section, even though the AFE algorithm can overcome the undersampling problem, the resulting image resolution is still controlled by the aperture size. To further illustrate this, the 3 degree by 3 degree aperture in Figure 4(a) is scaled to a 0.3 degree by 3 degree aperture in Figure 8(a), while still populating the aperture with 256 data samples. The same 9 point scatterers and radar parameters are used to simulate the radar data. Only the motion data is different. The AFE reconstruction results are shown in Figures 8(b)–8(d). As we can see by comparing Figures 8 to 3, the image resolution in the y direction remains essentially unchanged, while the image resolution in the z dimension gets much worse. Therefore, the AFE resolution in position is inversely proportional to the angular aperture. This is exactly the same as the Fourier transform.

Like many other model-based signal processing techniques, the adaptive feature extraction algorithm is sensitive to data error. We study the algorithm sensitivity by adding some noise to the data. Two types of errors are considered. The first is the radar data error. Figure 9(a) shows the reconstructed image when the radar data is

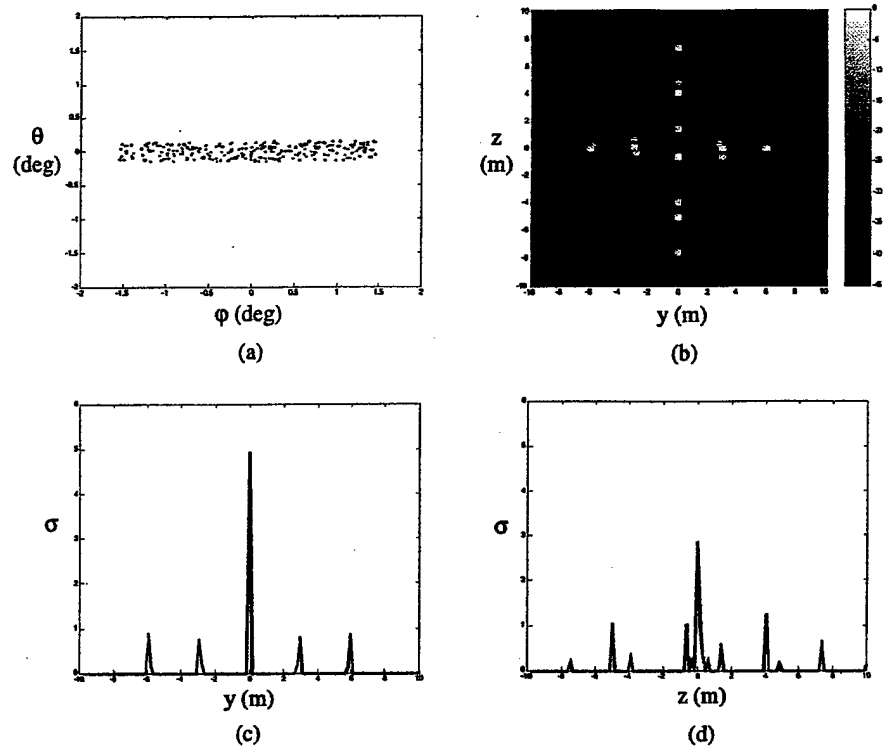

Figure 8. Reconstruction result using AFE. (a) Motion data in a 3 deg by 0.3 deg aperture. (b) (y, z) image. (c) y projection. (d) z projection.

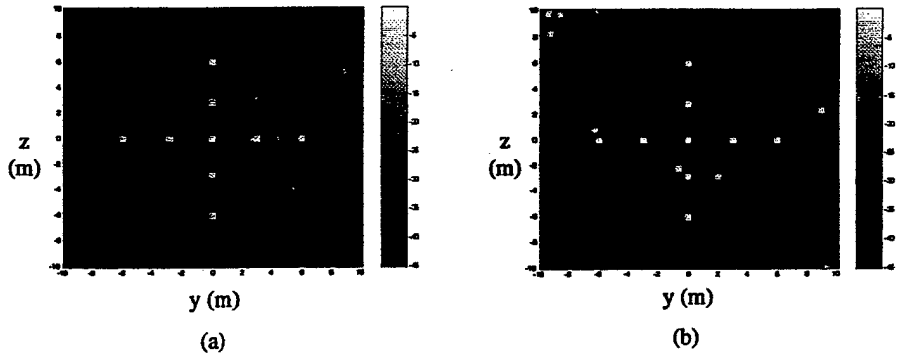

Figure 9. Reconstruction using noisy data. (a) $-20\,\mathrm{dB}$ white noise in the radar data. (b) 1% randomness in the angular positions.

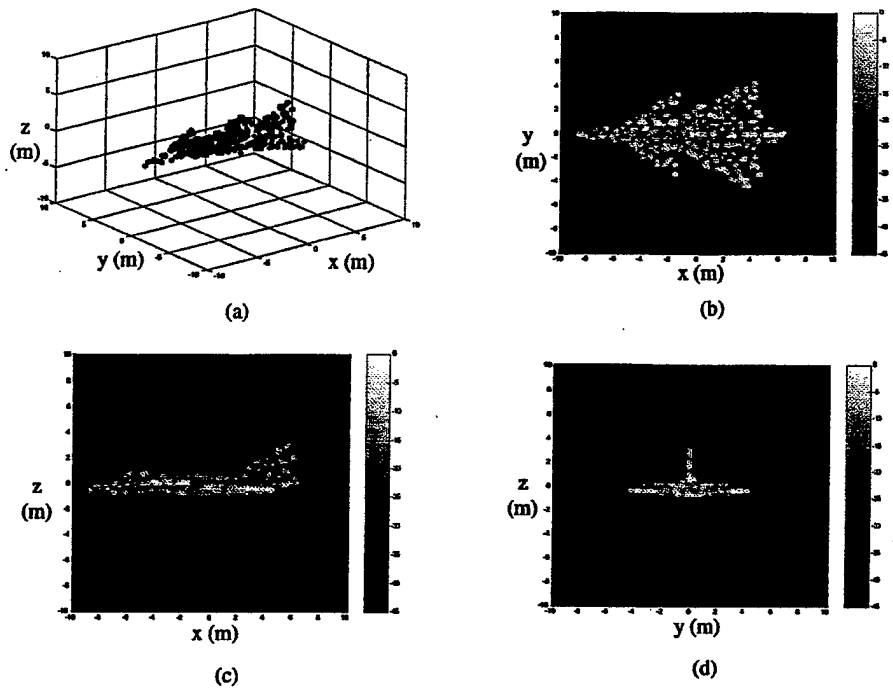

Figure 10. Point scatterer representation of an aircraft. (a) 3D point scatterer representation. (b) Top view. (c) Side view. (d) Front view.

contaminated with −20 dB of white noise. The second source of error is the motion parameter error. Figure 9(b) shows that the result with 1% random error in the motion parameters. Our experience shows that the algorithm is more sensitive to error in the motion parameters than that in the radar data. To alleviate the angular motion error, we suggest preprocessing the motion data according to *a priori* knowledge of the motion. For example, we can limit the motion data to low-order polynomial functions of dwell time if we believe the motion of the target is smooth.

4.3. Aircraft Imaging with Real 3D Motion Data

A full simulation is done with point scatterers from an aircraft model. 401-point scatterers with equal strength are used to model our example aircraft as shown in Figure 10(a). The three projections of the original target corresponding to the top view, side view, and front view of the aircraft are shown in Figures 10(b)–10(d). The 3D motion data

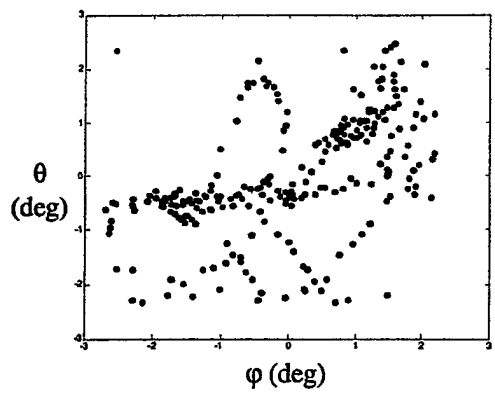

Figure 11. 3D motion data from an air target.

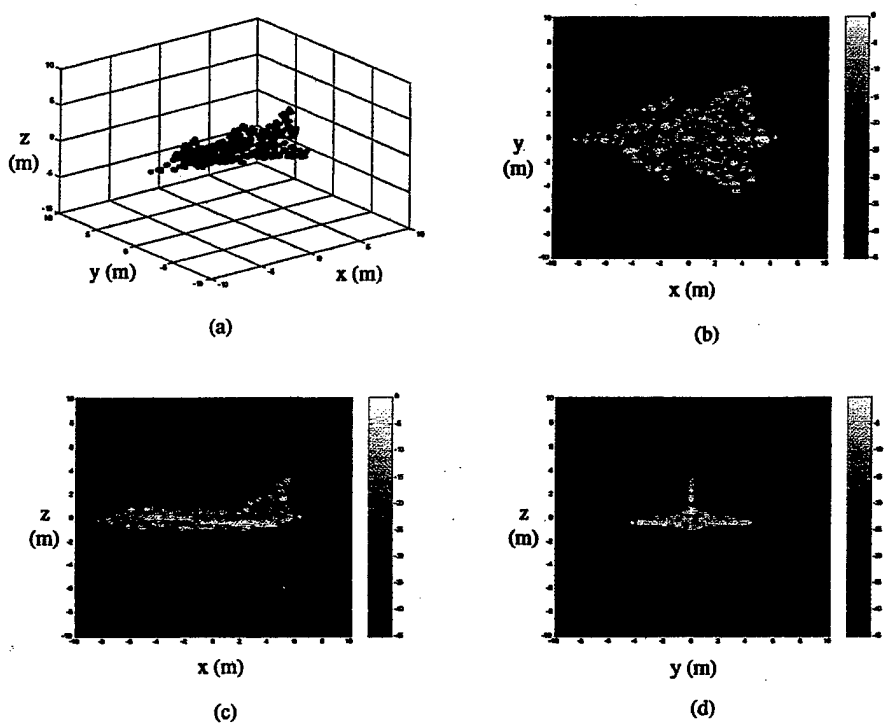

Figure 12. 3D image reconstructed by AFE based on the 3D motion model. (a) 3D view of the top 600 extracted point scatterers (b) Top view. (c) Side view. (d) Front view.

in Figure 11 shows a 5 degree by 5 degree angular window in both azimuth and elevation. They are from the actual flight paths of an aircraft. To simulate the radar data, the same radar parameters in the previous examples are used. Our goal is to reconstruct a 3D image from the range profiles simulated at these angles. Again, the highly non-uniform, undersampled distribution of the radar data in the angular aperture requires the use of the 3D motion model and the AFE algorithm in order to reconstruct a 3D image.

For 3D image construction, we need to find the positions and strengths of the point scatterers in 3D space. The range location x_s is directly obtained from the range profiles. Then for every range cell within the range profile, a collection of point scatterers with two cross-range locations $(y_s,\ z_s)$ and point scatterer strength σ_s are extracted from the AFE iterations. The computation time is about 15 minutes on a PC with a P III 750 MHz processor. The result is an image $\sigma_s(x_s,\ y_s,\ z_s)$, representing the scattering strength of scatterers in 3D space. We sort the scatterers according to their strengths and keep the top 600 point scatterers. The positions of those point scatterers are shown in Figure 12(a). The top view, side view, and front view of the reconstructed 3D image are shown in Figures 12(b)–12(d), respectively. They agree very well with the three projections from the original 3D point scatterers in Figure 10. Such features as the fuselage, the wings, and the vertical tail fin are correctly constructed. Our algorithm has also been tested on real radar data of an air target.

5. CONCLUSIONS

The problem of 3D ISAR imaging of a target with known motion data is discussed in this paper. The 3D motion model is necessary to form a 3D image of the target with 3D motion. The adaptive feature extraction algorithm along with the 3D motion model is proposed to process non-uniform, undersampled radar data collected over a 2D angular aperture. The advantages of the AFE algorithm are clearly demonstrated when compared to either the Fourier transform or the AFE based on 2D motion model. We find that the resolution of the AFE image is limited by the aperture size in the corresponding motion direction. The sensitivity of the method is also discussed. Simulation with a 3D point scatterer model of an aircraft shows that the resulting 3D images carry much more information than the range profiles or the 2D ISAR images alone. One advantage of the algorithm is that the data collection scheme is very flexible. Therefore, it is a viable tool for target feature extraction when the 3D motion data associated with the target are available.

The significance of this work is twofold. First, when there is known target motion, 3D motion is taken into account based on the 3D motion model. It is not treated as an error term as in traditional 2D ISAR imaging. Second, when there is unknown target motion, this work provides us with an intermediate step toward blind 3D ISAR image formation. Instead of doing the more challenging 3D motion compensation directly, we might first estimate the 3D motion from the radar data. We can then use this method to form a 3D image.

ACKNOWLEDGMENT

This work is supported by the Office of Naval Research under contract No. N00014-98-1-0615.

REFERENCES

1. Chen, C. C. and H. C. Andrews, "Target motion induced radar imaging," *IEEE Trans. Aerospace Electron. Syst.,* Vol. 16, No. 1, 2–14, Jan. 1980.
2. Ausherman, A., A. Kozma, J. L. Waker, H. M. Jones, and E. C. Poggio, "Developments in radar imaging," *IEEE Trans. Aerospace Electron. Syst.,* Vol. 20, No. 4, 363–400, July 1984.
3. Chen, V. C. and W. J. Miceli, "Effect of roll, pitch and yaw motions on ISAR imaging," *SPIE Proc. Radar Processing,* Vol. 3810, 149–158, Denver, CO, July 1999.
4. Rihaczek, A. W. and S. J. Hershkowitz, "Choosing imaging intervals for identification of small ships," *SPIE Proc. Radar Processing,* Vol. 3810, 139–148, Denver, CO, July 1999.
5. Carrara, W. G., R. S. Goodman, and R. M. Majewski, *Spotlight Synthetic Aperture Radar — Signal Processing and Algorithms,* Artech House, Boston, MA, 1995.
6. Stuff, M. A., "Three-dimensional analysis of moving target radar signals: methods and implications for ATR and feature-aided tracking," *SPIE Proc. Algorithms for Synthetic Aperture Radar Imagery VI,* Vol. 3721, 485–496, Orlando, FL, Aug. 1999.
7. Mayhan, J. T., K. M. Cuomo, and J. E. Piou, "High resolution 3D 'snapshot' ISAR imaging," to appear in *IEEE Trans. Aerospace Electron. Syst..*
8. Xiao, S. and D. C. Munson, "Spotlight-mode SAR imaging of a three-dimensional scene using spectral estimation techniques," *Proc. IEEE Inter. Geosci. and Remote Sensing Symp.,* Vol. 2, 642–644, Seattle, WA, July 1998.

9. Li, J., Z. Bi, and Z.-S. Liu, "Autofocus and feature extraction in curvilinear SAR via a relaxation-based algorithm," *IEE Proc. Radar, Sonar Navig.,* Vol. 146, No. 4, 201–207, Aug. 1999.
10. Wang, Y. and H. Ling, "Adaptive ISAR image construction from nonuniformly undersampled data," *IEEE Trans. Antennas and Propagat.,* Vol. 48, 329–331, Feb. 2000.
11. Tsao, J. and B. D. Steinberg, "Reduction of sidelobe and speckle artifacts in microwave imaging: the CLEAN technique," *IEEE Trans. Antennas and Propagat.,* Vol. 36, No. 4, 543–556, Apr. 1988.
12. Mallat, S. G. and Z. Zhang, "Matching pursuits with time-frequency dictionaries," *IEEE Trans. Signal Processing,* Vol. 41, No. 12, 3397–3415, Dec. 1993.
13. Li, J. and H. Ling, "ISAR motion detection and compensation using genetic algorithms," *SPIE Proc. Wavelet Applications VIII,* Vol. 4391, 380–388, Orlando, FL, Apr. 2001.

Junfei Li was born in Wuhan, China in 1971. He received the B.S. and M.S. degrees in Electrical Engineering from Northwestern Polytechnical University, Xi'an, China, in 1992 and 1995 respectively. He was with the Institute of Remote Sensing Applications, Beijing, China as a Research Engineer from 1995 to 1998. He is currently a Ph.D. candidate and working as a Graduate Research Assistant at the University of Texas at Austin. His present interests include radar imaging, digital signal processing, RF, and microwave engineering.

Hao Ling was born in Taichung, Taiwan, on September 26, 1959. He received the B.S. degrees in electrical engineering and physics from the Massachusetts Institute of Technology, in 1982, and the M.S. and Ph.D. degrees in electrical engineering from the University of Illinois at Urbana-Champaign, in 1983 and 1986, respectively. He joined the faculty of the University of Texas at Austin in September 1986 and is currently a Professor in the Department of Electrical and Computer Engineering and holder of the L. B. Meaders Professorship in Engineering. Dr. Ling's principal area of research is in computational electromagnetics. He has actively contributed to the development and validation of numerical and asymptotic methods for characterizing the radar cross section from complex targets. His recent research interests also include radar signal processing, fast algorithms for radar image simulation and automatic target identification.

An Algorithm to Detect the Presence of 3D Target Motion from ISAR Data

Junfei Li*, Hao Ling* and Victor Chen+

*Department of Electrical and Computer Engineering
The University of Texas at Austin
Austin, TX 78712-1084
fei@ece.utexas.edu

+Airborne Branch
Naval Research Laboratory
Washington, DC 20375

Abstract. We present an algorithm to detect the presence of 3D target motion from ISAR data. Based on the 3D point scatterer model, we first examine the effect of 3D motion on ISAR imaging. It is shown that existing motion compensation algorithms cannot properly focus targets exhibiting 3D motion during the imaging interval. An algorithm is then derived to blindly detect the degree of 3D target motion from raw radar data. It is based on measuring the linearity of phases between two or more point scatterers on the target. The phase estimation is implemented using the adaptive joint time-frequency technique. Examples are provided to demonstrate the effectiveness of the 3D motion detection algorithm with both simulation and real ISAR data. The detection results are corroborated with the truth motion data from on-board motion sensors and correlated with the resulting ISAR images.

Key words: radar imaging; motion compensation; 3D motion detection

1. Introduction

High-resolution inverse synthetic aperture radar (ISAR) imaging is regarded as an effective tool in automatic target recognition [1-2]. Ideally, the desired target motion is uniform rotation without translational motion, under which a two-dimensional (2D) Fourier transform brings the radar data in the (frequency)-(dwell time) domain into the (range)-(Doppler frequency) domain. Otherwise, motion compensation is needed as an intermediate step to form a focused ISAR image.

Since target motion can always be decomposed into translational motion and rotational motion, a typical motion compensation algorithm consists of two steps. First, a point on the target is focused through translational motion compensation. When there is non-uniform rotational motion, other points on the target are not necessarily focused. Rotational motion compensation is then applied to focus these other points. Existing motion compensation algorithms usually assume that the rotational motion of a target is confined to a 2D plane during the dwell duration [1-7]. We shall use the term *2D motion* to refer to target rotational motion of this type. Under the 2D motion assumption, rotational compensation of a second point on the target will focus the whole target. When there is *3D motion*, i.e., when the rotational motion is not confined to a 2D plane, rotational compensation of a second point cannot focus the whole target.

Recently, several independent research groups have reported that, for aircraft undergoing fast maneuvers or ships on rough seas, the motion of a target may be highly chaotic and does not always obey the 2D motion model [8-10]. As a result, the image formed using the standard motion compensation algorithms is blurred. In [8] and [9], the effect of 3D motion on ISAR imaging is discussed. However, target motions are assumed

to be known from other auxiliary sensor data that are usually not accessible in real operational environment. In [10], the imaging interval is adaptively chosen based on the resolved target feature in the radar image to overcome the 3D motion issue. It requires sound knowledge of the target under consideration, which is often not known to the end users of ISAR data.

The objective of this paper is to develop an algorithm to detect the presence of 3D motions during the imaging interval from ISAR data. Based on the 3D point scatterer model, we first examine the effect of 3D motion on existing imaging algorithms. We then develop an algorithm to blindly detect the existence of 3D motion. For this purpose, only the estimation of phases of several prominent point scatterers is needed. It can be accomplished by the joint time-frequency analysis [6]. With the detection algorithm, we have the ability to distinguish the time intervals when the target undergoes smooth 2D motion from those containing more chaotic 3D motion. As a result, the good imaging intervals where focused images are more easily formed can be automatically determined.

The paper is organized as follows. First, the ISAR imaging problem is formulated in terms of a point scatterer model in Section 2. In Section 3, the 2D motion assumption in existing motion compensation algorithms is analyzed. We show the reason why 3D motion is a problem for ISAR imaging. Section 4 discusses the 3D motion detection algorithm in detail. Examples from both simulation and measurement data are presented in Section 5. The conclusions are given in the last section.

2. 2D and 3D Motion Models

The standard model used in ISAR processing is the point scatterer model given as

$$E(f,t_D)=\sum_{i=1}^{Ns}\sigma_i(x_i,y_i)\exp\{-j\frac{4\pi f}{c}[r(t_D)+x_i+y_i\varphi(t_D)]\} \tag{1}$$

where f is the radar frequency and t_D is the dwell time. The radar echo data $E(f,t_D)$ is in the (frequency)-(dwell time) domain. x and y represent the target range and cross-range positions, respectively. The target consists of N_s point scatterers, with the ith point scatterer depicted by position (x_i,y_i) and strength $\sigma(x_i,y_i)$. The target motion includes both the translational motion described by $r(t_D)$ and the rotational motion described by $\varphi(t_D)$. When there is no translational motion and the rotational motion is uniform, it is seen that a 2D Fourier transform brings the radar data $E(f,t_D)$ into a radar image $\sigma(x,y)$. Otherwise, motion compensation is a critical step in ISAR imaging.

The above model is what we call a 2D problem since the target rotational motion is confined to a 2D plane and describable in terms of only one angular parameter φ. When there is 3D motion of the target, a more general 3D model is required:

$$E(f,t_D)=\sum_{i=1}^{Ns}\sigma_i(x_i,y_i,z_i)\exp\{-j\frac{4\pi f}{c}[r(t_D)+x_i+y_i\varphi(t_D)+z_i\theta(t_D)]\} \tag{2}$$

In the above expression, a third coordinate z of the target is included to represent the 3D target and another independent angular motion parameter θ is introduced to describe the 3D rotational motion (see Fig. 1). It is possible to perform 3D target imaging if the target motion is known exactly [11], [12]. In practical ISAR scenarios, however, we have no access to the target motion. Our objectives here are to examine the effect of 3D motion on ISAR imaging and devise an algorithm to detect the presence of 3D motion from the radar data itself, i.e., without any additional knowledge of the target motion.

3. Problem of Existing Motion Compensation Algorithms with 3D Target Motion

First, we show that the more general 3D model degenerates into the 2D model under two conditions. The first case is when there is a linear relationship between φ and θ, i.e.,

$$\theta(t_D) = b\varphi(t_D) \tag{3}$$

This allows us to cast equation (2) into the form

$$E(f, t_D) = \sum_{i=1}^{Ns} \sigma_i(x_i, y_i, z_i) \exp\{-j\frac{4\pi f}{c}[r(t_D) + x_i + (y_i + bz_i)\varphi(t_D)]\} \tag{4}$$

Comparing (4) with (1), we see that if we define $y_i' = y_i + bz_i$, then the rotational motion is in fact a two-dimensional one and the resulting 2D image $\sigma(x_i, y_i')$ is the projection from the 3D target $\sigma(x_i, y_i, z_i)$ onto the 2D motion plane.

The second case is when the z dimension of the target is so small that the third phase term in (2) can be neglected. For example, suppose a radar operates at a frequency of 10 GHz and the θ variation is limited to 0.5 degree. If the target thickness in the z-dimension is less than 0.2 m, then the third phase term is less than $\pi/4$ and the 2D model is adequate.

From the above consideration, we see that the 2D model is applicable if either the rotational motion is 2D or the target is of 2D in extent. When there exists 3D motion on a full 3D target, any motion compensation algorithms based on the 2D model is not expected to focus the target well. We will now examine this issue in more detail. Since the translational motion compensation is independent of the models in (1) and (2), only the rotational motion compensation needs to be investigated. With 2D rotational motion present, the phase of a point scatterer i due to the rotational motion is

$$P_i(t_D) = y_i \varphi(t_D) \tag{5}$$

Here, the constant $4\pi f/c$ has been suppressed for simplicity. As we can see from (5), the phases of all the point scatterers are linearly related to each other (through the ratio of their cross range positions). If we make one of the phases a linear function of time, then all the phases are linearized simultaneously, and the whole target can be focused after the Fourier transform. This is the basis of most 2D rotational motion compensation algorithms based on the point scatterer model [3-6]. This concept is illustrated in Figure 3. Figure 3(a) shows the phase functions of two point scatterers under 2D rotational motion. Figure 3(b) shows that both points can be made linear functions of time after we force one of them to be a linear function.

With 3D motion, the phase of a point scatterer due to the rotational motion is

$$P_i(t_D) = y_i \varphi(t_D) + z_i \theta(t_D) \tag{6}$$

In this case, the phases of the point scatterers are no longer linearly related. If we make one of the phases a linear function of time, the phases of the other point scatterers are not automatically made linear functions of time, as was the case of 2D motion. Figure 3(c) shows the phase functions of two point scatterers with 3D motion. As we can see from Figure 3(d), after one point is forced to be of linear phase, the phase of the other point remains nonlinear.

Figure 4 illustrates some simulation results of the effect of the rotational motion compensation based on the model in (1) on the final images under 2D and 3D target motion. The adaptive joint time-frequency (AJTF) algorithm reported in [6] is used for motion compensation. Ten points in 3D space are used to simulate the radar data. Figure 4(a) shows an assumed 2D rotational motion. Figure 4(b) shows the image after the

translational motion compensation. The image shows one point being focused in range cell 25 while other points are unfocused due to the rotational motion. Figure 4(c) shows the image after the 2D rotational motion compensation in which a point scatterer in range cell 57 is selected for focusing. All the point scatterers are focused in the image. The situation with an assumed 3D target motion is shown in Figures 4(d)-4(f). Figure 4(d) shows the assumed 3D motion. Figure 4(e) shows the image after translational motion compensation. Figure 4(f) shows the final image after the 2D rotational motion compensation. The two points in range cells 25 and 57 are focused, as expected. Another point scatterer in range cell 99 is also focused as it happens to be in the same 2D motion plane as the point scatterer in range cell 57. As we can see, it is not possible to focus all the points simultaneously with an existing algorithm based on the 2D motion model.

4. 3D Motion Detection Algorithm

Since existing motion compensation algorithms cannot handle 3D target motion, it is desirable to develop a general compensation algorithm that can accommodate 3D motion. However, this is a difficult task (see [13] for background on this problem) and outside the scope of this work. Our goal here is to develop an algorithm to detect the presence of 3D motion from radar data. If we can reliably detect those time intervals where 2D target motions are predominant, we can use the existing 2D motion compensation algorithms to form well-focused ISAR images.

As discussed in the last section, 2D motion can be represented by a linear relationship between θ and φ. Therefore, we set out to detect the existence of a nonlinear

relationship between θ and φ in our 3D motion detection algorithm. First, we write the relationship between θ and φ into a linear and a nonlinear part as follows:

$$\theta(t_D) = b\varphi(t_D) + m(t_D) \tag{7}$$

where b is the linear constant and $m(t_D)$ is the nonlinear part which indicates deviation from 2D target motion, or the degree of 3D motion. Next we try to gather target motion information by analyzing the phases of two point scatterers on the target. Let us write the relationship between the phase functions P_1 and P_2 of two point scatterers as:

$$P_2(t_D) = aP_1(t_D) + n(t_D) \tag{8}$$

The relationship is again decomposed into the linear part, where a is the linear constant, and the nonlinear part $n(t_D)$. Our goal is to derive a relationship between $m(t_D)$ and $n(t_D)$ so that the presence of m can be detected by observing n.

After the standard translational motion compensation, the time-varying phase of a point scatter is in the form of

$$P_i(t_D) = \Delta y_i \varphi(t_D) + \Delta z_i \theta(t_D) \tag{9}$$

where Δy_i and Δz_i are differential positions of point scatterer i relative to the reference point chosen during translational motion compensation. Substituting (7) into (9) and then evaluating (9) at point scatterers 1 and 2, we have

$$P_1(t_D) = (\Delta y_1 + b\Delta z_1)\varphi(t_D) + \Delta z_1 m(t_D) \tag{10a}$$

$$P_2(t_D) = (\Delta y_2 + b\Delta z_2)\varphi(t_D) + \Delta z_2 m(t_D) \tag{10b}$$

We next substitute (10) into (8), which leads to

$$a[(\Delta y_1 + b\Delta z_1)\varphi(t_D) + \Delta z_1 m(t_D)] + n(t_D) = (\Delta y_2 + b\Delta z_2)\varphi(t_D) + \Delta z_2 m(t_D) \tag{11}$$

Notice that if there is only 2D motion, then the phases of the two point scatterers must be linear. This means if $m=0$, then $n=0$. By using this fact and equating the coefficients of $\varphi(t_D)$ in (11), the constant a can be derived:

$$a = \frac{\Delta y_2 + b\Delta z_2}{\Delta y_1 + b\Delta z_1} \tag{12}$$

By substituting (12) into (11), we finally arrive at

$$m(t_D) = \frac{\Delta y_1 + b\Delta z_1}{\Delta z_2 \Delta y_1 - \Delta y_2 \Delta z_1} n(t_D) \tag{13}$$

Equation (13) states that once the nonlinear phase term n is known, it is proportional to nonlinear motion m. Therefore, the steps to determine the degree of 3D target motion are as follows. First, we extract the phases of two point scatterers from the radar data. Next we find the nonlinear phase function n using a minimum least squares fit of equation (8). Once n is known, we use equation (13) to decide on the degree of 3D motion. The remaining issues are: (i) how to determine the phase functions of the point scatterers, (ii) how to define the degree of nonlinearity and the degree of 3D motion once n is known, and (iii) how to compare the degree of 3D motion from one imaging interval to another. These three issues are discussed in the following subsections.

4.1. Phase Estimation Using Adaptive Joint Time-Frequency Projection

After the translational motion compensation, the radar signal contains only rotational motion. To estimate the phase of a prominent point scatterer, we utilize the adaptive joint time-frequency (AJTF) projection technique discussed in [6]. We begin with the radar data in the (range)-(dwell time) domain. Within a fixed range cell, the data can be written as

$$E_s(t_D) = \sum_{i=1}^{Nr} \sigma_i \exp(-j\frac{4\pi f_c}{c}(y_i\varphi(t_D) + z_i\theta(t_D)) \tag{14}$$

where f_c is the center frequency. Among the N_r point scatterers within the range cell, we express the phase behavior of the strongest one as a polynomial function:

$$\phi_M(t_D) = (f_1 t + f_2 t^2 + f_3 t^3 + ..) \tag{15a}$$

and consider

$$h(t) = \exp[-j\varphi_M(t_D)] \tag{15b}$$

as a basis for the radar signal. The phase parameters are then found by searching for the maximum projection from the radar signal onto the basis function:

$$< f_1, f_2, f_3, ... >= \arg\max | \int E(t_D)h^*(t_D)dt_D | \tag{16}$$

Equation (16) means that the phase function parameters are estimated to give a maximum projection from the radar data onto the basis function for that prominent point scatterer. In the search procedure, the first term f_1 can be obtained by using the fast Fourier transform, while all other higher order terms f_2, f_3, ... are obtained using exhaustive search. Figure 5 illustrates the process of AJTF phase estimation. Figure 5(a) shows the radar signal in one range cell with three point scatterers in the joint (dwell time)-(Doppler frequency) plane. The tilted trajectory of the prominent point scatterer 1 implies there exist higher-order terms in the phase function. Figure 5(b) shows the basis function $h(t_D)$. During the search, we change the position (f_1), tilting (f_2) and curvature (f_3, ...) of h until the projection of h onto the radar signal is maximized.

4.2. Measure of Nonlinearity between Two Phase Functions

We notice that in (8), the two phase functions are formulated with a linear relationship plus a nonlinear residual part. After the two phase functions are estimated using the AJTF technique, a least-squares fitting can be performed to generate the best-fit linear part. The actual phases deviates from this linear relationship. The deviation n is integrated over the dwell time to represent the degree of phase nonlinearity over the imaging interval as follows:

$$N_{12} = \int | n_{12}(t_D) | \, dt_D \tag{17}$$

The process is illustrated in Figure 6. The solid line is the actual relationship between the two phase functions P_1 and P_2. The dotted line is the linear approximation of the relationship. The area of the shadowed region is N_{12}.

In a similar fashion, we define the degree of 3D motion as the deviation from a linear relationship between θ and φ over the dwell interval as follows:

$$M = \int | m(t_D) | \, dt_D \tag{18}$$

Based on (13), we see that M and N_{12} are directly related:

$$N_{12} = \beta_{12} M \tag{19a}$$

where

$$\beta_{12} = \left| \frac{\Delta z_1 \Delta y_2 - \Delta y_1 \Delta z_2}{\Delta y_1 + b \Delta z_1} \right| \tag{19b}$$

Thus by finding the observable N_{12}, we can obtain the degree of 3D motion M to within a proportionality constant.

4.3. 3D Motion Comparison among Different Imaging Intervals

As indicated by (19), the phase nonlinearity of two point scatterers N is proportional to the degree of 3D motion M, so we can use the detected phase nonlinearity as a measure of 3D motion. However, we notice that the constant of proportionality is dependent on the point scatterer positions. A problem arises when we need to compare the detection result from one imaging interval to that from another imaging interval. Since we cannot guarantee that we track the same set of points from frame to frame, the proportionality constant can change from frame to frame, and we cannot reliably observe M from N across frames. To overcome this difficulty, we track more than two point scatterers within each frame and compute N_{ij} for each pairing of scatterers i and j ($i \neq j$). Then we generate an average value $<N_{ij}>$ from all the possible phase relationships. From (19), we have

$$< N_{ij} >=< \beta_{ij} > M \tag{20}$$

We postulate that, from a statistical point of view, $<\beta_{ij}>$ approaches a constant that is independent of frames if we average over a sufficient number of point scatterers. If this is true, $<N_{ij}>$ should become a good indicator of M.

We test the effectiveness of this approach on the detection result by simulation. We input a set of motion parameters and generate the phase functions based on the 3D motion model. 20 point scatterers from an airplane model is used. We then randomly choose a number of point scatterers and use their phase functions to compute $<N_{ij}>$. We examine how the results vary as different number of point scatterers is used. We find that the results begin to converge after about 5 scatterers. Fig. 7 shows a plot of $<N_{ij}>$ versus the frame number if we use 5 point scatterers (10 phase pairs). If we increase the number

of point scatterers to 10 (45 phase pairs), there is only minor change in the detection output. Therefore, $<N_{ij}>$ can be used to indicate the degree of 3D motion given a sufficient number of point scatterers.

5. Results

To demonstrate the effectiveness of the 3D motion detection algorithm, we test our algorithm on radar data from two targets. The first target is an aircraft, which flew in a large clockwise circle during a 9-minute interval. We also have access to the target motion data through the GPS (global positioning system) and INS (inertial navigation system) sensors carried on-board the aircraft [14-16]. Figure 8 shows our processing flow chart. The GPS/INS data is used to establish the truth target motion. The raw radar data is used as input to the 3D motion detection algorithm. We can also generate the ISAR images using our AJTF motion compensation algorithm [6]. We are therefore able to both compare the detection result with the truth motion, and observe the effect of the 3D motion on the ISAR image quality.

We first test the 3D motion detection algorithm on simulated radar data. To generate the simulation data, we use the actual motion data from the GPS/INS sensors in conjunction with a point scatterer model. From the aircraft model, 60 point scatterers are selected to simulate the radar data based on the actual motion data and equation (2). Five range cells are then chosen for phase analysis in the detection procedure. Figure 9(a) shows the detected degree of 3D motion for 20 image frames from the simulated radar data. For comparison, Figure 9(b) shows the degree of 3D motion obtained based on the truth motion data. The frames with significant 3D motion are highlighted with circles and

the frames with 2D motion are highlighted with diamonds. It is seen that the two results agree fairly well.

Next, we test the detection algorithm using the actual radar measurement data. Figure 10(a) shows the detected 3D motion from the radar data over 20 frames. The corresponding imaging interval for each frame is 2.3 seconds while the total flight duration is 5 minutes. The four frames with the most significant 3D motion based on our detection algorithm are labeled as circles. They are frames 6, 14, 17 and 18. Figure 10(b) shows the degree of 3D motion obtained based on the truth motion data. We observe that the truth motion data indeed contains a high degree of 3D motion at those four frames detected by our algorithm.

To further examine the quality of the ISAR images when 3D motion is present, we generate images using our motion compensation algorithm in Figures 11 to 14. Figure 11(a) shows the plot of θ vs. ϕ derived from the truth motion data for frame 18, which is a frame found to contain substantial 3D motion. The actual motion is shown in the solid curve and the dashed line is the best-fit 2D motion approximation. It is clear that the solid curve deviates significantly from the dashed line and the actual motion cannot be well approximated with 2D motion. Figure 11(b) shows the resulting image obtained after the motion compensation, and is blurred in the Doppler dimension (vertical axis). As expected, the 2D motion compensation algorithm cannot focus all the points due to the 3D target motion. Figures 12 (a) and 12(b) show the same conclusion for frame 14, which is another frame identified as having significant 3D motion. In Figure 13, we show the results for frame 2, which has very little 3D motion. As we can see from Figure 13(a), the actual motion can be well approximated by a line in the θ-ϕ plot. The image shown

Figure 13(b) is well focused. In particular, the point scatterers on the target show nearly equal range and Doppler extent, contrary to the previous two images. The aircraft bodyline is clearly recognizable.

From Figure 10, we notice that there exists a discrepancy in frame 11, where the detection result does not indicate any 3D motion while the truth motion data shows a significant amount of 3D motion. The truth motion is shown in Figure 14(a), confirming the presence of 3D motion. One explanation is that those prominent points used by the detection algorithm lie nearly on a 2D plane so that they still can be focused. As we have discussed in Section 3, the 2D model is applicable if either the motion is 2D or the target is of 2D in extent. It is likely that the latter condition is met for this frame. This is confirmed by the image shown in Figure 14(b). We see that the image quality is actually not so bad. Therefore, our detection algorithm objectively reflects the quality of the images generated by the 2D motion compensation.

A second data set is used to test our 3D motion detection algorithm. This data set consists of the ISAR data collected from a small ship on the ocean. Because of the surface movement of the sea, the target is believed to have considerable 3D motion during the imaging intervals. The 3D motion detection result is shown in Figure 15(a) with the peaks corresponding to regions with 3D motion. The total data duration is 20 seconds and the imaging dwell time is 0.64 second per frame. For this data set, reliable truth target motion is not available. Instead, we generate the motion compensated images shown in Figures 15(b) to 15(d) to demonstrate the effect of 3D motion on ISAR image quality. The image frame with the largest detected 3D motion, frames 3, is shown in Figure 15(b). It is poorly focused. Figure 15(c) shows the image from frame 14, which

is the frame with the second highest detected 3D motion. The frame with the smallest 3D motion based on our algorithm, frame 20, is shown in Figure 15(d). It shows a well-focused ISAR image. This test confirms the effectiveness of our algorithm in detecting good imaging intervals from those imaging intervals containing large 3D motion.

6. Conclusions

In this paper, we set out to develop an algorithm to detect the presence of 3D target motion from ISAR data. Based on the 3D point scatterer model, we first examined the effect of 3D motion on ISAR imaging. It was shown that the existing motion compensation algorithms could not properly focus targets exhibiting 3D motion during the imaging interval. We then derived an algorithm to blindly detect the degree of 3D target motion from raw radar data. It is based on measuring the linearity of phases between two or more point scatterers on the target. The phase estimation was implemented using the adaptive joint time-frequency technique. Examples were provided to demonstrate the effectiveness of the 3D motion detection algorithm with both simulation and real ISAR data. The detection results were corroborated with the truth motion data from on-board motion sensors and correlated with the resulting ISAR images. With the detection algorithm, we have the ability to distinguish the time intervals when the target undergoes smooth 2D motion from those containing more chaotic 3D motion. As a result, the good imaging intervals where focused images are more easily formed can be automatically selected.

Acknowledgment

This work is supported by the Office of Naval Research under contract No. N00014-98-1-0615.

References

[1] C. C. Chen and H. C. Andrews, "Target motion induced radar imaging," *IEEE Trans. Aerospace Electron. Syst.*, vol. 16, no. 1, pp. 2-14, Jan. 1980.

[2] A. Ausherman, A. Kozma, J. L. Waker, H. M. Jones and E. C. Poggio, "Developments in radar imaging," *IEEE Trans. Aerospace Electron. Syst.*, vol. 20, no. 4, pp. 363-400, July 1984.

[3] W. G. Carrara, R. S. Goodman and R. M. Majewski, *Spotlight Synthetic Aperture Radar - Signal Processing and Algorithms*, Artech House, Boston, MA, 1995.

[4] S. Werness, W. Carrara, L. Joyce and D. Franczak, "Moving target imaging algorithms for SAR data," *IEEE Trans. Aerospace Electron. Syst.*, vol. 26, no. 1, pp. 57-67, Jan. 1990.

[5] D. E. Wahl, P. H. Eichel, D. C. Ghiglia and C. V. Jakowatz, "Phase gradient autofocus- a robust tool for high resolution SAR phase correction," *IEEE Trans. Aerospace Electron. Syst.*, vol. 30, no. 3, pp. 827-835, July 1994.

[6] Y. Wang, H. Ling and V. C. Chen, " ISAR motion compensation via adaptive joint time-frequency techniques," *IEEE Trans. Aerospace Electron. Syst.*, vol. 34, no. 2, pp. 670-677, Apr. 1998.

[7] Z. Liu, R. Wu and J. Li, "Complex ISAR imaging of maneuvering targets via the Capon estimator," *IEEE Trans. Signal Processing*, vol. 47, no. 5, pp. 1262-1271, May 1999.

[8] V. C. Chen and W. J. Miceli, "Effect of roll, pitch and yaw motions on ISAR imaging," *SPIE Proc. Radar Processing, Technology and Applications VI*, vol. 3810, pp. 149-158, Denver, CO, July 1999.

[9] J. Li, Y. Wang, R. Bhalla, H. Ling and V. C. Chen, "Comparison of high-resolution ISAR imagery from measured data and synthetic signatures," *SPIE Proc. Radar Processing, Technology and Applications VI*, vol. 3810, pp. 170-179, Denver, CO, July 1999.

[10] A. W. Rihaczek and S. J. Hershkowitz, "Choosing imaging intervals for identification of small ships," *SPIE Proc. Radar Processing, Technology and Applications VI*, vol. 3810, pp. 139-148, Denver, CO, July 1999.

[11] S. Xiao and D. C. Munson, "Spotlight-mode SAR imaging of a three-dimensional scene using spectral estimation techniques," *Proc. IEEE Inter. Geosci. and Remote Sensing Symp.*, vol. 2, pp. 642-644, Seattle, WA, July 1998.

[12] J. T. Mayhan, K. M. Cuomo and J. E. Piou, "High resolution 3D 'snapshot' ISAR imaging," *IEEE Trans. Aerospace Electron. Syst.*, vol. 37, no. 2, pp. 630-641, Apr. 2000.

[13] M. A. Stuff, "Three-dimensional analysis of moving target radar signals: methods and implications for ATR and feature-aided tracking," *SPIE Proc. Algorithms for Synthetic Aperture Radar Imagery VI,* vol. 3721, pp. 485-496, Aug. 1999.

[14] K. Rosenbach and J. Schiller, "Non co-operative air target identification using radar imagery: identification rate as a function of signal bandwidth," *IEEE 2000 Inter. Radar Conference*, pp. 457-462, Alexandria, VA, May 2000.

[15] T. Sparr, S. E. Hamran and E. Korsbakken, "Estimation and correction of complex target motion effects in inverse synthetic aperture imaging of aircraft," *IEEE 2000 Inter. Radar Conference*, pp. 457-462, Alexandria, VA, May 2000.

[16] H. Ling and J. Li, "Application of adaptive joint time-frequency processing to ISAR image formation," *Proc. of the 10th IEEE workshop on Statistical Signal and Array Processing*, pp. 476-479, Pocono Manor, PA, Aug. 2000.

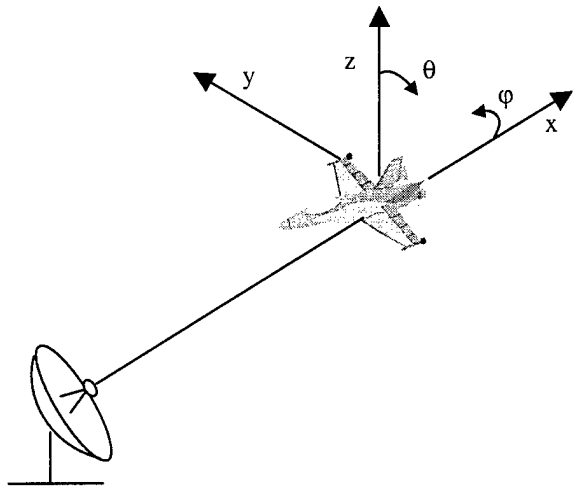

Fig. 1 Geometry of an ISAR problem.

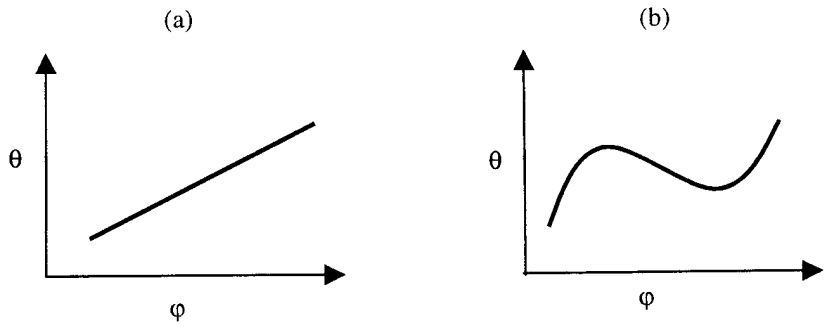

Fig. 2 Illustration of 2D motion vs. 3D motion.

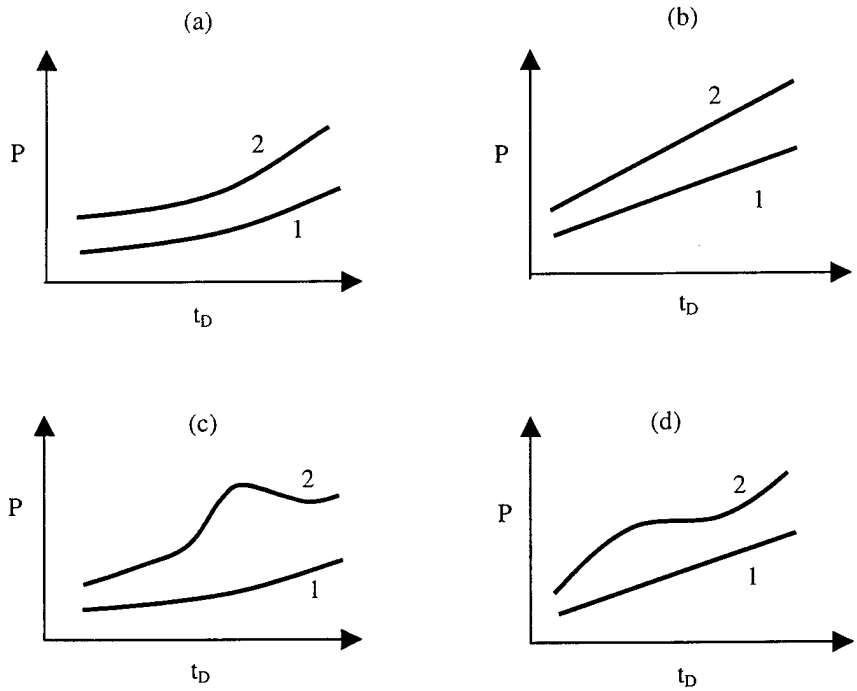

Fig. 3 Phase linearization achieved by rotational motion compensation (a) Phases of two point scatterer with 2D rotational motion. (b) Both phases are linearized with rotational motion compensation. (c) Phases of two point scatterers with 3D motion. (d) Only one phase is linearized with rotational motion compensation.

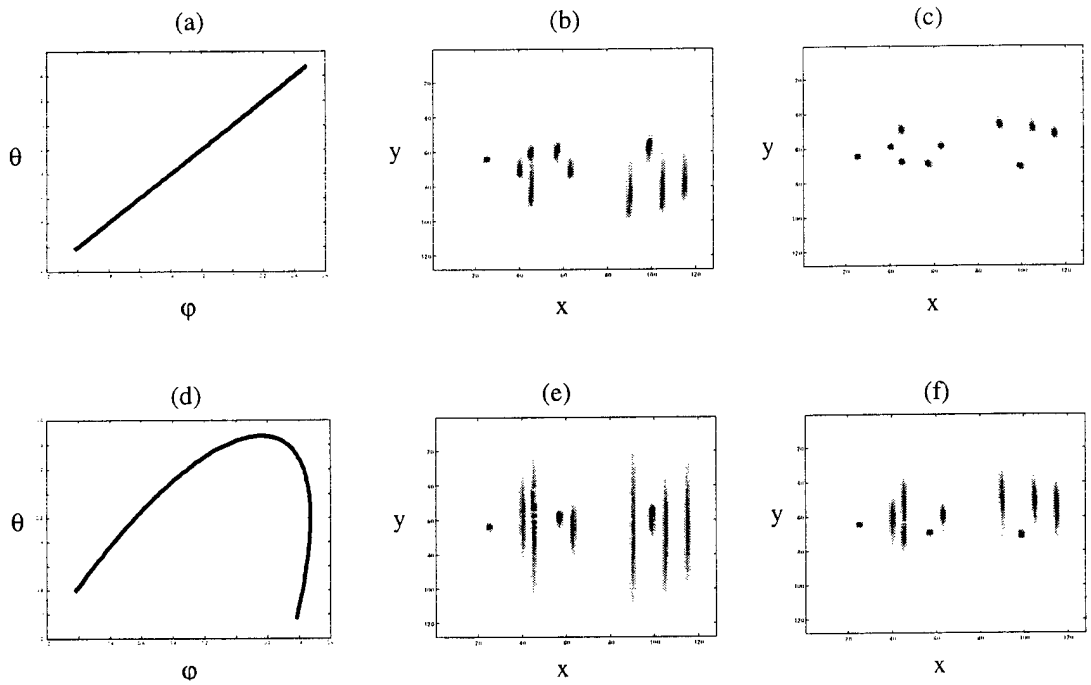

Fig. 4 Problem with a typical motion compensation algorithm (a) Target undergoes a 2D motion. (b) Image after translational motion compensation. (c) Image after rotational motion compensation. (d) Target undergoes a 3D motion. (e) Image after translational motion compensation. (f) Image after rotational compensation.

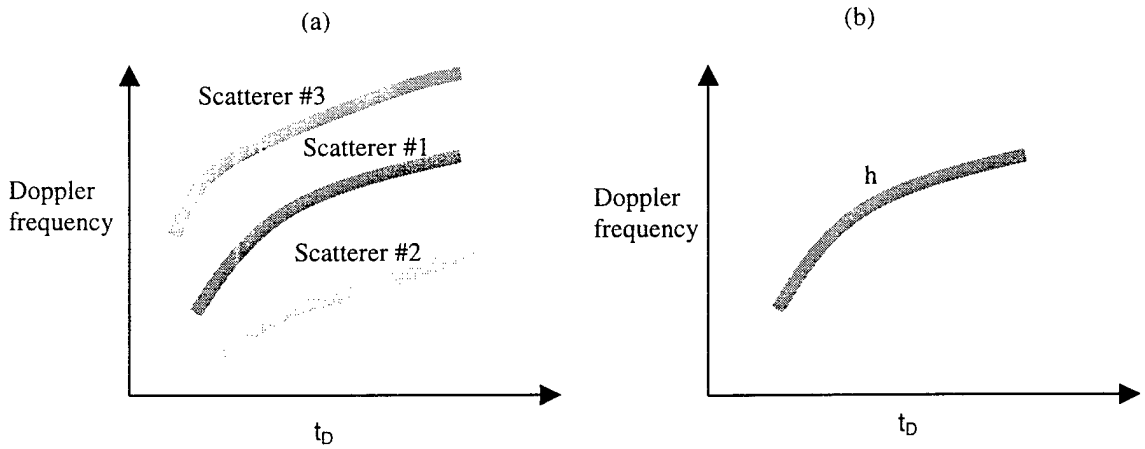

Fig.5 (a) (Dwell time)-(Doppler frequency representation of radar signal in a range cell with three point scatterers. (b) The basis function that is best matched to the dominant point scatterer is found by the AJTF project method.

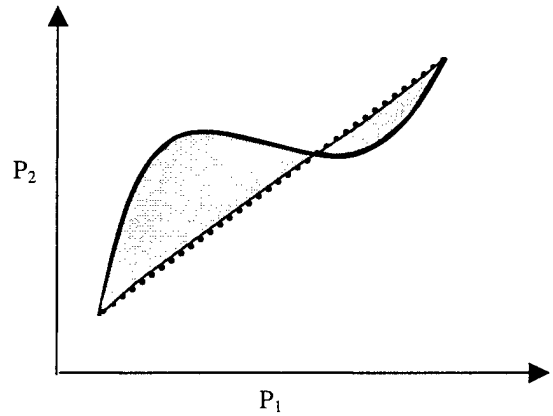

Fig. 6 Measure of the nonlinearity of two phase functions.

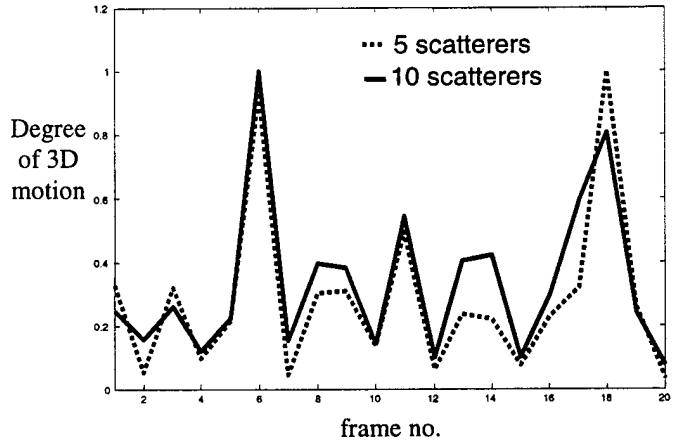

Fig. 7 Effect of the number of point scatterers used on 3D motion detection result.

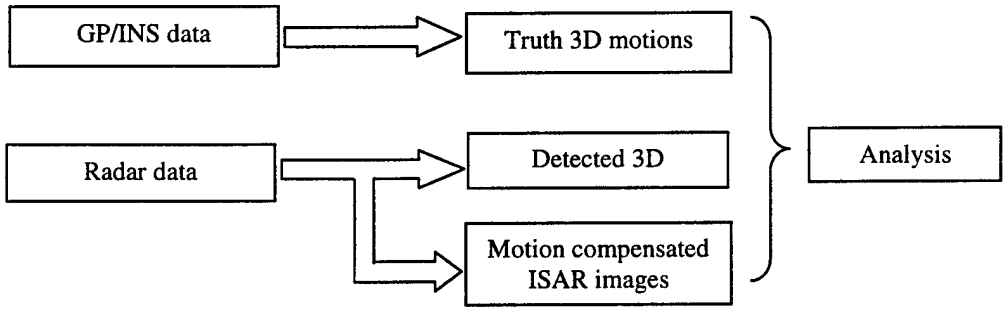

Fig. 8 Data processing flow chart.

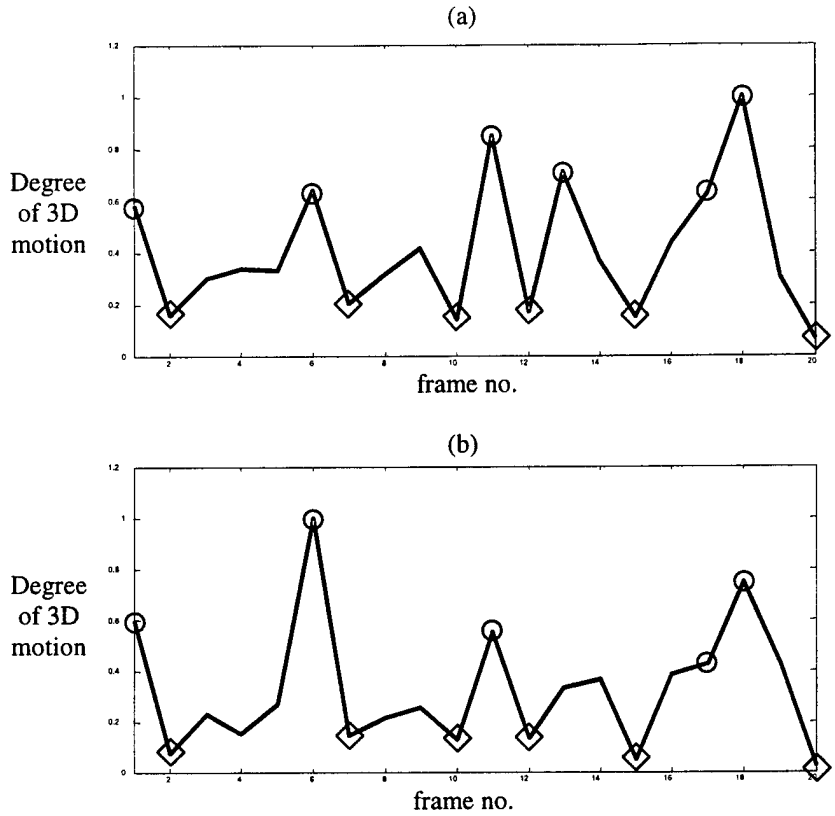

Fig. 9 (a) Detected 3D motion from simulated radar data.
(b) Degree of 3D motion from truth motion data.

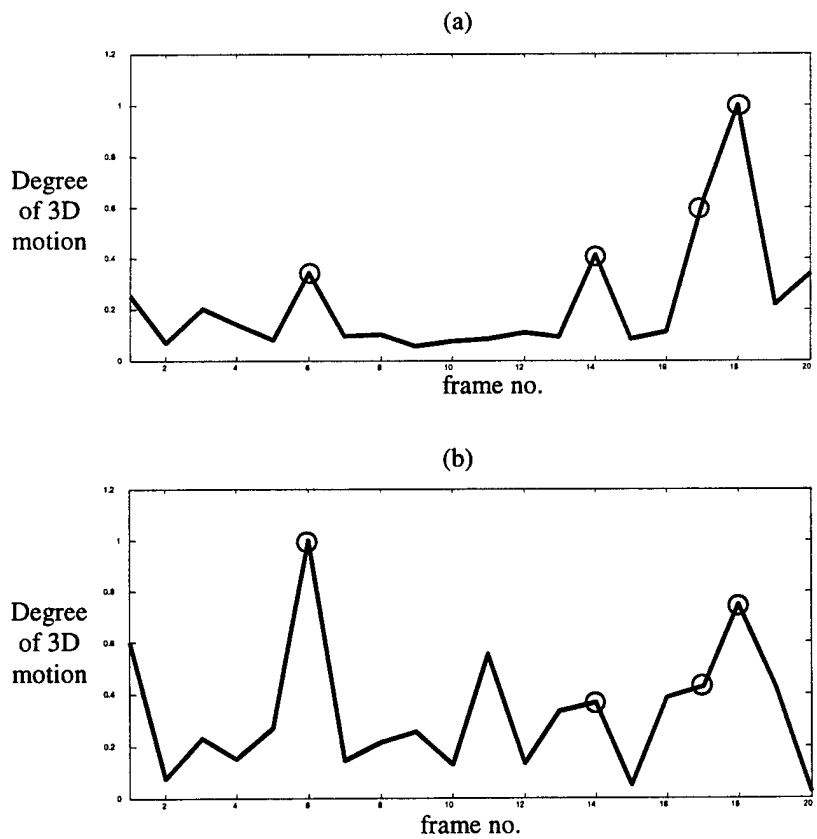

Fig.10 (a) Detected 3D motion from aircraft radar data.
(b) Degree of 3D motion from truth motion data.

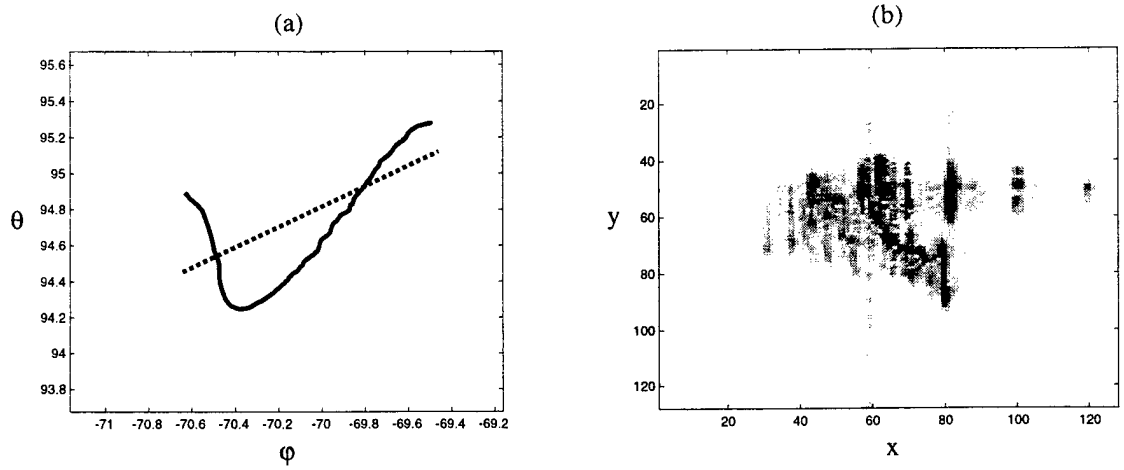

Fig. 11 3D motion and resulting ISAR image (frame 18).

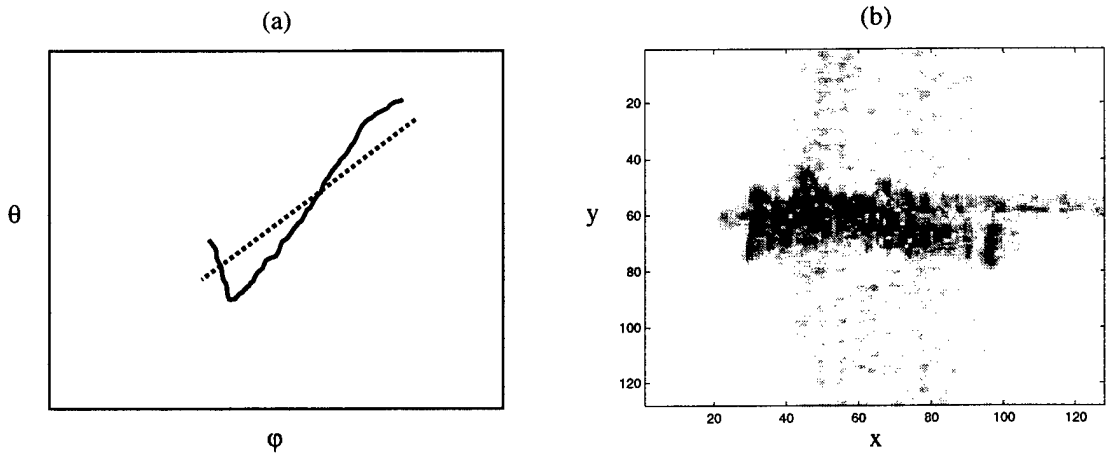

Fig. 12 3D motion and resulting ISAR image (frame 14).

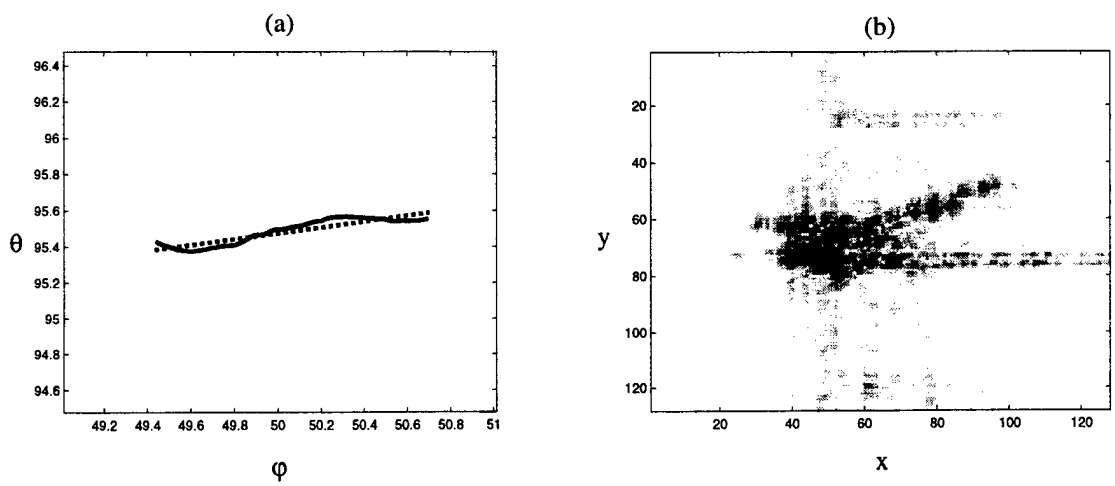

Fig.13 2D motion and resulting ISAR image (frame 2).

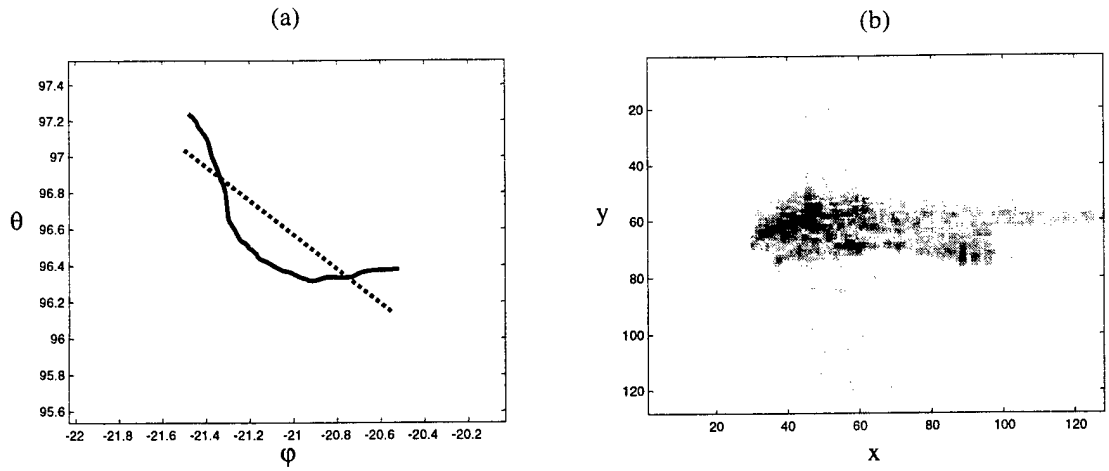

Fig. 14 Frame no.11 showing focused ISAR image with 3D motion.

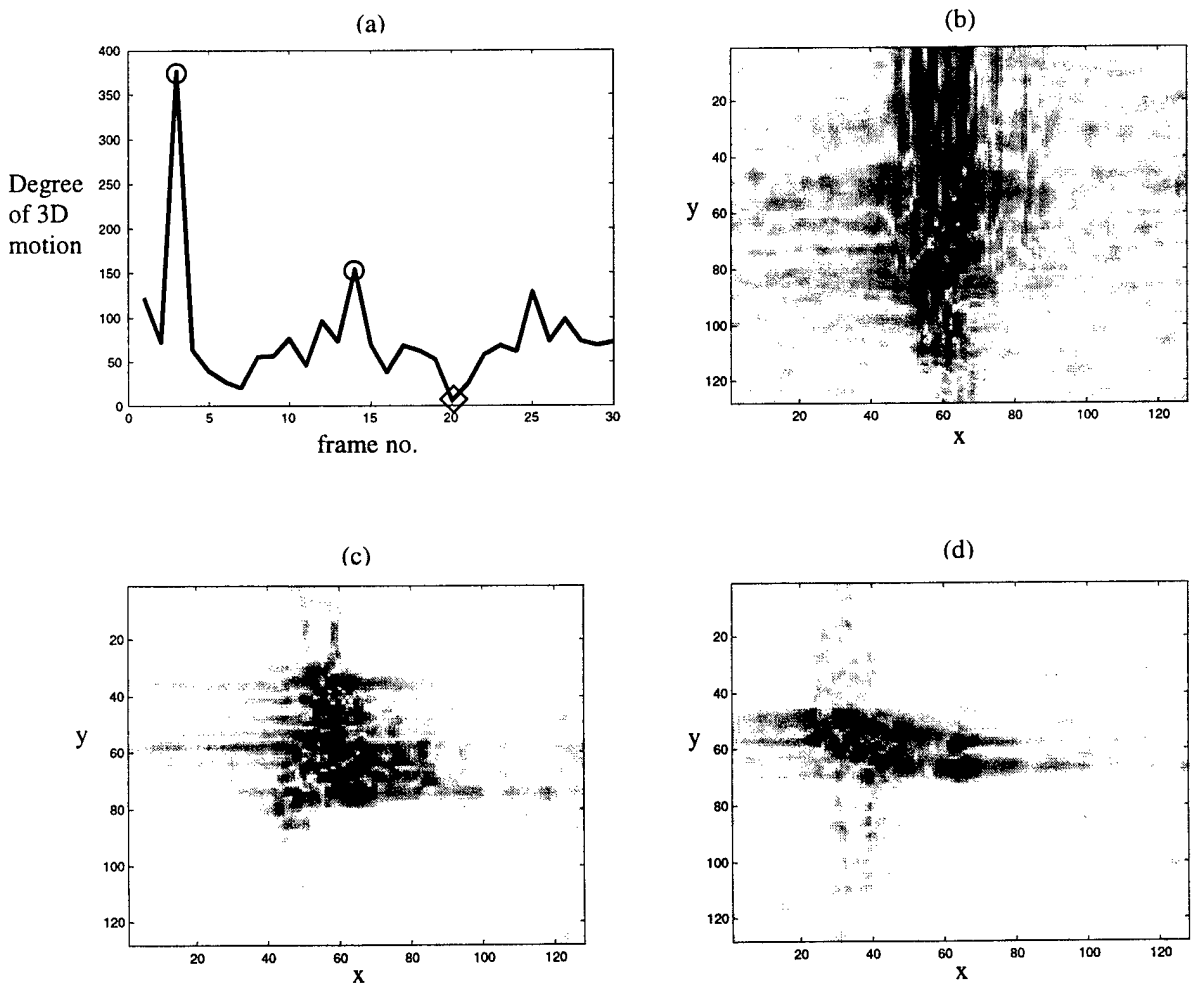

Fig. 15 3D motion detection result from radar data of a ship (a) Detected 3D motion. (b) ISAR image from frame 3. (c) ISAR image from frame 14. (d) ISAR image from frame 20.

Use of Genetic Algorithms in ISAR Imaging of Targets with Irregular Motions

Junfei Li and Hao Ling

Department of Electrical and Computer Engineering
The University of Texas at Austin
Austin, TX 78712-1084

Abstract In this paper, genetic algorithms (GA) are proposed for inverse synthetic aperture radar (ISAR) imaging of an unknown target. The adaptive joint time-frequency (AJTF) analysis is used to achieve translation and rotational motion compensation through motion parameterization. GA is used as an alternative to exhaustive search in the parameter search process. While maintaining the same accuracy, GA has lower computational complexity, especially for targets with highly irregular motions. Simulation and measurement data results demonstrate the feasibility of GA in ISAR imaging of targets with high-order motions.

Keywords genetic algorithms, exhaustive search, inverse synthetic aperture radar, adaptive joint time-frequency

1. Introduction

Inverse synthetic aperture radar (ISAR) system usually collects radar data from a target moving on the ground, in the air, or over the ocean. In the ISAR problem shown in Figure 1, the radar is stationary while the target moves with both translation motion and rotational motion. In the microwave frequency range, ISAR has been identified as an effective tool for target identification [1].

Target motion is an essential part in ISAR imaging. On the one hand, target motion is needed to generate Doppler (or cross-range) resolution [2]. On the other hand, unwanted motion causes image blurring. When the target has uniform rotational motion only and the radar data is collected over a small angular aperture, a simple Fourier transform will bring the raw radar data into a two-dimensional ISAR image. However, actual targets observed by operational radar rarely have such an ideal motion. Therefore, motion compensation is needed to generate focused ISAR imagery. There exist many different motion compensation algorithms to deal with target motion [3-5]. Most of the algorithms start with coarse range alignment based on the correlation of the range profiles. Then the phase information within one range cell is utilized to achieve fine motion compensation.

Phase estimation is critical in fine motion compensation. Compared to the amplitude, the phase of the radar signal is much more sensitive to the change in range. Based on the concept of signal parameterization reported in [6, 7], an adaptive joint time-frequency (AJTF) algorithm was proposed in [8] for phase estimation of a prominent point scatterer. In this method, the target motion is modeled as a polynomial function and an exhaustive search procedure is used to find the motion parameters that are embedded in the phase of the prominent point scatterer. While the performance of this algorithm is very good [9], the main bottleneck in this procedure is the computational complexity associated with the parameter search. When the target motion is highly irregular, the number of parameters needed to model the motion becomes large and the use of the exhaustive search becomes prohibitively expensive.

In this paper, our objective is to reduce the computation time associated with the motion parameter search in the AJTF procedure. Our proposed approach is to incorporate genetic algorithms (GA) [10] into the AJTF search process. (Some preliminary work on this topic was reported in [11].) In contrast with conventional optimization methods, GA is a population-based, statistical search technique. It borrows such concepts as inheritance and mutation from the biological evolution process [12]. As a global optimization technique, GA is known to be very easy to implement and applicable to many design and inverse problems [13].

This paper is organized as follows. In Sections 2 and 3, we outline the methodology. The AJTF analysis for ISAR motion compensation is described in Section 2. Genetic algorithms are introduced in Section 3. The next two sections include results and analysis. In Section 4, simulations with point scatterers are provided to validate the use of GA for phase estimation. Measurement data processing results are shown in Section 5. Finally, conclusions are given in Section 6.

2. ISAR Motion Compensation Using the Joint Time-Frequency Projection

A two-dimensional point scatterer model relates the radar data to a moving target through the following equation

$$E(f,t_D) = \sum_i \sigma_i \exp\{-j\frac{4\pi f}{c}[r(t_D) + x_i + y_i\varphi(t_D)]\} \tag{1}$$

where f is the frequency and t_D is the dwell time. In this model, the radar data is comprised of the sum of responses from a collection of point scatterers. (x_i, y_i) denotes the point scatterer position while σ_i denotes the scatterer strength. The target motion includes both translation motion $r(t_D)$ and rotational motion $\varphi(t_D)$.

After range compression is done by Fourier transforming the data with respect to frequency, the original radar data is converted into a set of range profiles. Range alignment is then carried out via amplitude correlation of the range profiles to place all the point scatterers in their correct range bins. The radar signal through one range cell r can thus be expressed in the form of

$$E_r(t_D) = \sum_i \sigma_i \exp\{-j\frac{4\pi f_0}{c}[\Delta r(t_D) + x_i + y_i\varphi(t_D)]\} \tag{2}$$

where f_0 is the center frequency of the radar and the index includes only those point scatterers in the particular range cell. The residual translation motion is depicted as $\Delta r(t_D)$. After such coarse alignment procedure, the residual translation motion is smaller than the range resolution. However, it can still be larger than the radar wavelength. Therefore, it is important to include this term in (2).

Both of the residual translation motion $\Delta r(t_D)$ and the rotational motion $\varphi(t_D)$ can be expanded into polynomial functions of the dwell time as

$$\begin{aligned} \Delta r(t_D) &= a_1 t_D + a_2 t_D{}^2 + a_3 t_D^3 \ldots \\ \varphi(t_D) &= b_1 t_D + b_2 t_D{}^2 + b_3 t_D^3 \ldots \end{aligned} \tag{3}$$

where any coefficients beyond the first order are detrimental to ISAR image formation. To solve the ISAR motion compensation problem, we need to determine these motion parameters and to remove the unwanted nonlinear phase terms from the radar data.

This task can be accomplished using the AJTF procedure [8]. The essential idea of this procedure is to find the basis function that most resemble the strongest signal component in equation (2). For our problem, a basis function in the form of

$$h(t_D) = \exp[-j\frac{4\pi f_0}{c}(f_1 t_D + f_2 t_D^2 + f_3 t_D^3 ..)] \tag{4}$$

is used. The best basis is found by searching for parameters $f_1, f_2, f_3, \ldots$ that maximize the projection from the radar signal onto the basis, i.e.,

$$< f_1, f_2, f_3, \cdots >= \arg\max |< E_r(t_D), h(t_D) >| \tag{5}$$

where the projection is formulated as the inner product of the two functions as

$$< E_r(t_D), h(t_D) >= \int E_r(t_D) h^*(t_D) dt_D \tag{6}$$

In (5), the linear coefficient f_1 can be found efficiently with the fast Fourier transform (FFT). Coefficients for the nonlinear phase terms, $f_2, f_3, \ldots$, must be determined through a more time-consuming search.

Figure 2 depicts the concept of AJTF processing for ISAR translation motion compensation. After range alignment, the range profiles are shown in Figure 2a. Range cell i contains a prominent point scatterer and Figure 2b shows the joint (dwell time)-(Doppler frequency) representation of the radar signal through this range cell. A signal with linear phase behavior shows up as a straight horizontal line in the joint time-frequency plane. Both scatterers shown in Figure 2b are tilted and curved due to the higher-order residual motion. Also shown in the figure is the basis function h. To get the maximum projection, different values of $f_1, f_2, f_3, \ldots$ are tried until the basis function approaches the strongest scatterer. After the motion parameters of the prominent point scatterer are found in this manner, we can carry out the translation motion compensation by multiplying the radar data with the conjugate of this basis. Since all the point scatterers share the same translation motion in equation (2), this operation will remove the translation motion of the whole target.

After the translation motion compensation, we can rewrite equation (2) as

$$\hat{E}_r(t_D) = \sum_i \sigma_i \exp\{-j\frac{4\pi f_0}{c}[\Delta x_i + \Delta y_i(b_1 t_D + b_2 t_D{}^2 + b_3 t_D^3 ...)]\} \tag{7}$$

where $(\Delta x_i, \Delta y_i)$ is the differential position of the ith scatterer relative to the prominent point scatterer chosen for translation motion compensation in the previous step. To accomplish the rotational motion compensation, a second prominent point scatterer, usually in a range cell different from the first one, is chosen for phase analysis. The same search procedure as described before is used to find the rotational motion parameters in (7). Then to achieve rotational motion compensation, we can simply define a new dwell time variable t'_D:

$$t_D^{'} = t_D + \frac{1}{b_1}(b_2 t_D{}^2 + b_3 t_D{}^3 + ...) \tag{8}$$

and resample the radar data uniformly in terms of this new time variable:

$$\hat{E}_r(t_D^{'}) = \sum_i \sigma_i \exp[-j\frac{4\pi f_0}{c}(\Delta x_i + \Delta y_i b_1 t_D^{'})] \tag{9}$$

This resampling procedure is applied to the entire data set to linearize the phase of the all the point scatterers on the target. From equation (9), it is clear that Fourier transforming the data with respect to t'_D will resolve the point scatterers in the cross range dimension.

3. Use of Genetic Algorithms for Phase Parameter Search

As we have discussed in the last section, ISAR motion compensation can be formulated as a parameterization process for both translation motion and rotational motion. In [8], a brute-force search procedure is employed to carry out the parameterization. This means that we exhaustively search the solution space for the maximum projection. Genetic algorithms (GA) are investigated here to search for the

motion parameters to reduce the computation time. We should point out that although a structured tree-search is an easy and straightforward way to decrease the computational complexity, it does not always lead to a global optimum.

GA is a global optimization method based on concepts from ecological systems [10, 12, 14]. The flowchart of a typical GA process is illustrated in Figure 3. It starts by setting up the parameters for both the physical problem and the GA implementation. GA operates on a population of many individuals. The initial population is randomly generated within the searching space. The goodness of the solution is then evaluated based on an objective function. For our problem, the objective function is defined as the projection magnitude from the radar signal onto the basis function (see equation (5)). If we are satisfied with the solution, the process is done. Otherwise, a new generation is produced for the next evaluation-reproduction iteration. To make up individuals in the new generation, some good parents are selected from the previous generation and two operations called crossover and mutation are applied to produce children in the next generation. Whether or not crossover and mutation occur is determined randomly. The crossover and mutation probabilities are chosen based on the tradeoff between two conflicting requirements. Increasing the variation in the new generation brings a chance for better solutions, but it tends to lose the features of the good solutions from the previous generation.

Roughly speaking, there are two kinds of GA. One is binary-coded GA [10]. The other is real-coded GA [15]. In the former, the physical parameters to be searched are first discretized into binary bits. There is a one-to-one mapping between a physical parameter C and its N-bit binary representation $c_1, c_2, \ldots, c_N$ as follows:

$$C = \frac{C_{\max} - C_{\min}}{2^N - 1} \sum_{i=1}^{N} c_i 2^{i-1} + C_{\min} \tag{10}$$

where the $[C_{min}, C_{max}]$ is the valid search space for C. A candidate solution of the problem is expressed in the form of a chromosome, which is the collection of bits representing all the parameters. For crossover, a random break point in the chromosome is picked. The bits before the point from one parent are combined with the bits after the point from another parent to form one child. Another child is generated in the reverse fashion. For mutation, a single bit is randomly picked and its valued is inverted. The crossover and mutation operations for binary-coded GA are depicted in Figure 4a.

In real-coded GA, there is no coding-decoding process and the algorithm directly operates on the physical parameters. For crossover, a linear combination is usually used as follows

$$\begin{cases} C_1 = \alpha P_1 + (1-\alpha) P_2 \\ C_2 = (1-\alpha) P_1 + \alpha P_2 \end{cases} \tag{11}$$

where two children (C_1, C_2) are reproduced from two parents (P_1,P_2). α is a random number between 0 and 1 to ensure that the new parameters will not fall out of range. For mutation, a child C that is different from the parent P is needed. For this purpose, a solution P_e is picked up randomly from the searching space and linearly combined with P to generate C as in equation (11). The crossover and mutation operations for real-coded GA are depicted in Figure 4b.

The basic theory in GA, the schemata theory, seems to favor the use of binary-coded GA [14]. Most work on GA has followed this path. Recently, researchers have also experimented with real-coded GA and have observed some advantages in convenience

and accuracy [16]. In the next section, we will test both binary-coded and real-coded GA in our phase estimation problem.

The GA process is usually stopped using criteria based on the performance of the available solutions in the present generation. In our case, we do not know the true maximum projection value. Therefore, we choose to stop the GA process when the projection value does not increase after a certain number of generations.

4. Point Scatterer Simulation

Point scatterer simulations are first used to test the use of GA for ISAR motion compensation. In the first example, we assume two point scatterers with amplitudes 1 and 0.2. They are located within one range cell and contain third-order translation motion (i.e., the coefficients a_1, a_2 and a_3 in equation (3) are significant while all higher-order coefficients are zero). We run both binary-coded GA and real-coded GA to search for a_2 and a_3 for this simple phase estimation problem. The population size is 50. In both cases, the crossover probability is 0.8 and the mutation probability is 0.3. For exhaustive search, the search for a_2 and a_3 is carried out on a 128 by 128 grid. We choose a 7-bit representation in binary-coded GA and search in the same discrete space as in the exhaustive search. The actual objective function surface is plotted in Figure 5a. We observe many local maxima, indicating this would be a challenging problem for a local optimization method. Figure 5b shows the GA convergence curve, with the real-coded GA result in solid line and the binary-coded GA result in dashed line. Since GA is a statistical approach, we do not get exactly the same result from each GA run. To decrease the statistical variation, the results in Figure 5b are obtained by averaging over 20 GA

runs. We can see that after about 150 generations the two projection curves nearly converge to the truth value of 1. We also observe that real-coded GA produces a slightly higher projection value. Figure 5c shows the resulting phase from a single GA run after 200 generations. The estimated phase from binary-coded GA is plotted in circles, the phase from real-coded GA in crosses, and the original phase function in solid line. We see very good agreement among the three results, meaning good accuracy from the two GA results.

In the second example we compare the computational complexity of GA to exhaustive search for different orders of motion. As we have pointed out earlier, the main problem with exhaustive search for motion parameter extraction is the computational load. This problem becomes more acute when the order of the motion is high. Again, we use two point scatterers with amplitudes 1 and 0.2. We generate the radar data from these two point scatterers with some preset motion. We then apply exhaustive search, binary-coded GA, and real-coded GA for the phase estimation problem with different orders of motion. The same GA parameters as in the previous example are used and the results are averaged over 20 runs. The exhaustive search is known to have an exponential complexity of $O(exp(n))$. As expected, the resulting computation time in logarithm scale shows up as a straight line in Figure 6a. For GA, no theoretical complexity formulation is available in general. (The complexity of $O(n \log n)$ is claimed for selected test functions in [17].) We run both binary-coded GA and real-coded GA up to sixth-order motion (i.e., search for 5 parameters) and plot the results in Figure 6a. It is observed that both binary-coded GA and real-coded GA have much lower complexity than exhaustive search. The difference in complexity between the two GA is only minor. The projection values from

binary-coded GA and real-coded GA are next plotted in Figure 6b as circles and crosses, respectively. We see that the real-coded GA results are closer to the truth value of 1.0 than the binary-coded GA results, especially for higher-order motions. Since binary-coded GA searches on a finite grid as in exhaustive search, it can never get solutions that surpass the exhaustive search result. On the other hand, real-coded GA has the ability to search for any real values within the search range. Consequently, real-coded GA has more chance of finding a better solution. The same trend is also observed with measurement data and will be discussed further in the next section.

In the last simulation example, we show that the correct phase estimation from GA can be utilized to achieve ISAR motion compensation. For this purpose, four point scatterers, with two in one range cell and two in another range cell, are assumed to carry both translation and rotational motion up to third order. The aligned range profiles are shown in Figure 7a. The dwell time vs. Doppler frequency spectrograms of the original radar signal in range cells 1 and 2 are shown in Figures 7b and 7c respectively. Figure 7d shows the resulting cross range image using the Fourier transform directly. Without motion compensation, the four point scatterers are not well resolved. After we apply real-coded GA to the data in range cell 1, the estimated phase function is shown in Figure 8a. This corresponds to the translation motion of the target. After removing this motion, the resulting signal has spectrograms for range cells 1 and 2 shown in Figures 8b and 8c respectively. As expected, only one point is focused in Figure 8d. We next estimate the phase of a second strong point scatterer by running GA for range cell 2. The resulting phase function is shown in Figure 9a. Time resampling is done to linearize this curve.

Now all the point scatterers appear as horizontal lines in Figures 9b and 9c. Figure 9d shows the resulting image. The four point scatterers are all well resolved in this figure.

5. Measurement Data Processing

We next apply GA on some measurement data. The data were collected from an in-flight aircraft using a ground radar. 128 pulses are processed to form an ISAR image. This corresponds to an imaging interval of about 2.5 seconds. GA is evaluated for fine motion compensation. For the first data set, the image without any fine motion compensation is shown in Figure 10a. This image is unfocused due to the residual motion. We select a range cell with a dominant scatterer (range cell 79) and apply GA to estimate the phase based on a third-order translation motion model. The resulting images from binary-coded and real-coded GA are shown in Figures 10b and 10c, respectively. We observe that the two GA images are as focused as the reference image in Figure 10d obtained using exhaustive search. The corresponding projection values are 2401 and 2595, as compared to the exhaustive search result of 2401. We continue this comparison using 19 other imaging intervals. Figure 11a shows the projection values (normalized with respect to the exhaustive search result) for the 20 frames. For 19 out 20 frames, real-coded GA gives larger projection values than exhaustive search. The resulting images are either on par or slightly better focused than those obtained from exhaustive search. For binary-coded GA, 7 frames have lower projection values and are of inferior image quality to those from exhaustive search. The other 13 frames have exactly the same projection values as the exhaustive search result. Similar to our conclusion earlier based on the simulation data, our experience with the measurement data indicates that real-coded GA

consistently outperforms binary-coded GA in terms of accuracy. The computation time using Matlab codes on a Pentium III 750MHz PC is summarized in Figure 11b. While there is little change in the computational time for exhaustive search from one frame to another, the times for binary-coded and real-coded GA exhibit large variations in these single run results due to the statistical nature of GA. The average times for the binary-coded and real-coded GA are 19.5 seconds and 11.5 seconds, respectively. This is compared to the 45.5 seconds from exhaustive search. Finally, we note that for these 20 frames the third-order model is adequate to model the translation motion. Inclusion of higher-order translation motion or rotational motion does not improve the image quality for this data set.

For a second data set, we first apply third-order translation motion compensation using real-coded GA. The resulting image is shown in Figure 12a. It is seen that the selected dominant point scatterer at range cell 64 is not well focused. This means that the target contains higher motion that cannot be fully compensated by the third order motion model. This fact is also revealed by the spectrogram of the compensated signal in Figure 12b, as we observe a curved JTF trajectory for the scatterer. Next, a fourth-order motion model is tried and the real-coded GA result is shown in Figure 13a. From this figure, the reference point scatterer is better focused and the spectrogram of the signal is straightened in Figure 13b. Fifth-order translation motion is also attempted, and the result does not show much improvement. However, we observe that other point scatterers in Figure 13a are still smeared. This is confirmed by the spectrogram of the signal at a different range cell (number 71) shown in Figure 13c, which shows that the signal trajectory is curved in the spectrogram. Thus rotational motion must exist in this data. We

next apply fourth-order rotational motion compensation using real-coded GA. As shown in Figure 14a, the whole target is much better focused after the compensation. The spectrograms of the signal at both range cells become straightened in Figures 14b and 14c. While real-coded GA takes 45 seconds for the phase estimation problem, the computation time for fourth-order exhaustive search is estimated to be over 50 minutes based on the complexity curve in Figure 6a. Therefore, the time savings of GA over exhaustive search is quite significant in this real-world example.

6. Conclusions

In this paper, genetic algorithms have been applied to ISAR motion compensation. Based on the adaptive joint time-frequency analysis, GA is used in the phase estimation of prominent point scatterers on the target. The resulting parameterized phases are then used for translation and rotational motion compensation. Both binary-coded GA and real-coded GA have been implemented and tested using simulation and measurement data. It is found that real-coded GA outperforms binary-coded GA in terms of accuracy in the phase estimation problem. It is also shown that the computational complexity of the GA search is much less than that of exhaustive search. The time savings can become especially significant when the target exhibits highly irregular motion.

Acknowledgement

This work is supported by the Office of Naval Research under contract No. N00014-98-1-0615.

References

[1] A. Ausherman, A. Kozma, J. L. Waker, H.M. Jones and E. C. Poggio, "Developments in radar imaging," *IEEE Trans. Aerospace Electron. Syst.* vol. 20, pp.363-400, Apr. 1984.

[2] C. C. Chen and H. C. Andrews, "Target motion induced radar imaging," *IEEE Trans. Aerospace Electron. Syst.*, vol. 16, pp.2-14, Jan. 1980.

[3] W. G. Carrara, R. S. Goodman and R. M. Majewski, *Spotlight Synthetic Aperture Radar - Signal Processing and Algorithms*, Artech House, Boston, MA, 1995.

[4] A. W. Rihaczek and S. J. Hershkowitz, *Radar Resolution and Complex-Image Analysis*, Artech House, Boston, MA, 1996.

[5] S. Werness, W. Carrara, L. Joyce and D. Franczak, "Moving target imaging algorithms for SAR data," *IEEE Trans. Aerospace Electron. Syst.*, vol. 26, no. 1, pp. 57-67, Jan. 1990.

[6] S. G. Mallat and Z. Zhang, "Matching pursuits with time-frequency dictionaries," *IEEE Trans. Signal Processing*, vol. 41, no. 12, pp. 3397-3415, Dec. 1993.

[7] S. Qian and D. Chen, "Signal representation using adaptive normalized Gaussian functions," *Signal Processing*, vol. 36, no. 1, pp. 1-11, Mar. 1994.

[8] Y. Wang, H. Ling and V. C. Chen, "ISAR motion compensation via adaptive joint time-frequency technique," *IEEE Trans. Aerospace Electron. Syst.*, vol. 34, pp. 670-677, Apr. 1998.

[9] J. Li, Y. Wang, R. Bhalla, H. Ling and V. C. Chen, "Comparison of high-resolution ISAR imageries from measurement data and synthetic signatures," *SPIE 44th Annual Meeting, Radar Processing, Technology, and Applications*, vol. 3810, pp. 170-179, Denver, CO, July 1999.

[10] D. E. Goldberg, *Genetic Algorithms in Search, Optimization and Machine Learning*, Addison-Wesley, Reading, MA, 1989.

[11] J. Li and H. Ling, "ISAR motion detection and compensation using genetic algorithms," *Proc. of SPIE Wavelet Applications VIII*, vol. 4391, pp. 380-388, Orlando, FL, Apr. 2001.

[12] M. Mitechell and C. E. Taylor, "Evolutionary computation: an overview," *Annual Review of Ecology and Systematics*, vol. 30, pp. 593-616, 1999.

[13] Y. Rahmat-Samii and E. Michielssen (eds.), *Electromagnetic Optimization by Genetic Algorithms*, John Wiley & Sons, New York, NY, 1999.

[14] J. H. Holland, *Adaptation in Natural and Artificial Systems: an Introductory Analysis with Applications to Biology, Control, and Artificial Intelligence*, The University of Michigan Press, Ann Arbor, MI, 1975.

[15] D. E. Goldberg, "Real-coded genetic algorithms, virtual alphabet, and blocking," *Complex Systems*, vol. 5, pp. 139-167, 1991.

[16] F. Herrera, M. Lozano, and J. L. Verdegay, "Tackling real-coded genetic algorithms: operators and tools for behavioral analysis," *Artificial Intelligence Review*, vol. 12, pp. 265-319, 1998.

[17] R. Salomon, "Genetic algorithms and the $O(n \ln n)$ complexity on selected test functions," *Proc. Artificial Neural Networks in Engineering (ANNIE'95)*, pp. 325-330, ASME Press, New York, NY, 1995.

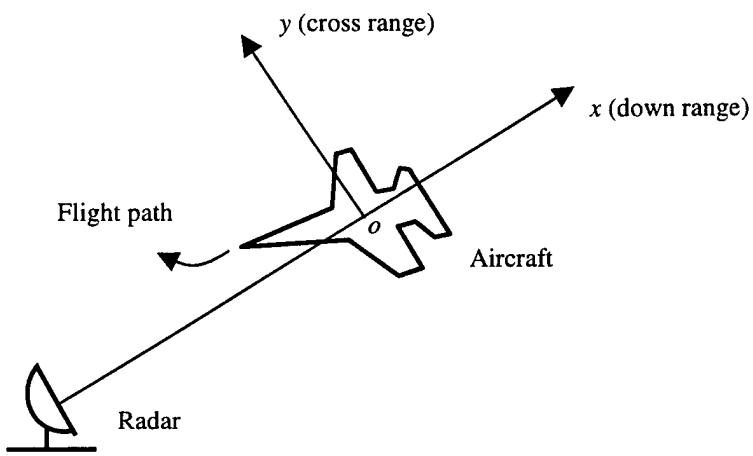

Fig. 1. Geometry of the ISAR imaging problem.

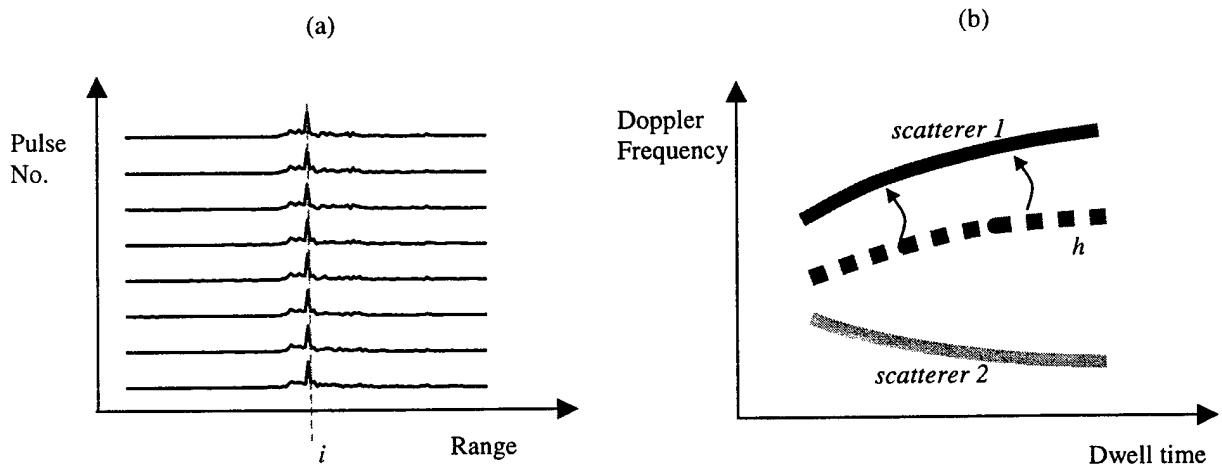

Fig. 2. The concept of AJTF analysis for ISAR motion compensation. (a) Correlator-aligned range profiles with a strong point scatterer in range cell *i*. (b) Joint (dwell time)-(Doppler frequency) representation of the signal in range cell *i*. The basis function *h* that is best matched to the strongest scatterer is determined via parameter search.

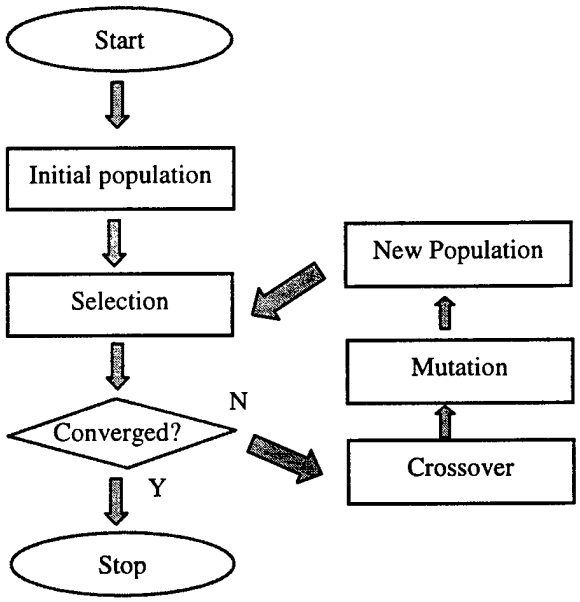

Fig. 3. Flowchart of GA.

(a)

Crossover $\left.\begin{array}{r}\mathbf{10111101}\\ \mathit{01101010}\end{array}\right\}\begin{array}{l}\mathbf{1011}\mathit{1010}\\ \mathit{0110}\mathbf{1101}\end{array}$

Mutation $\mathbf{10\underline{1}11101} \rightarrow \mathbf{10\underline{0}11101}$

(b)

Crossover $\left.\begin{array}{r}C_1\\ C_2\end{array}\right\}\begin{array}{l}\alpha P_1 + (1\text{-}\alpha) P_2\\ (1\text{-}\alpha) P_1 + \alpha P_2\end{array}$

Mutation $C \rightarrow \alpha P + (1\text{-}\alpha) P_e$

Fig. 4. Examples of crossover and mutation operations in binary and real-coded GA. (a) Binary-coded GA. (b) Real-coded GA.

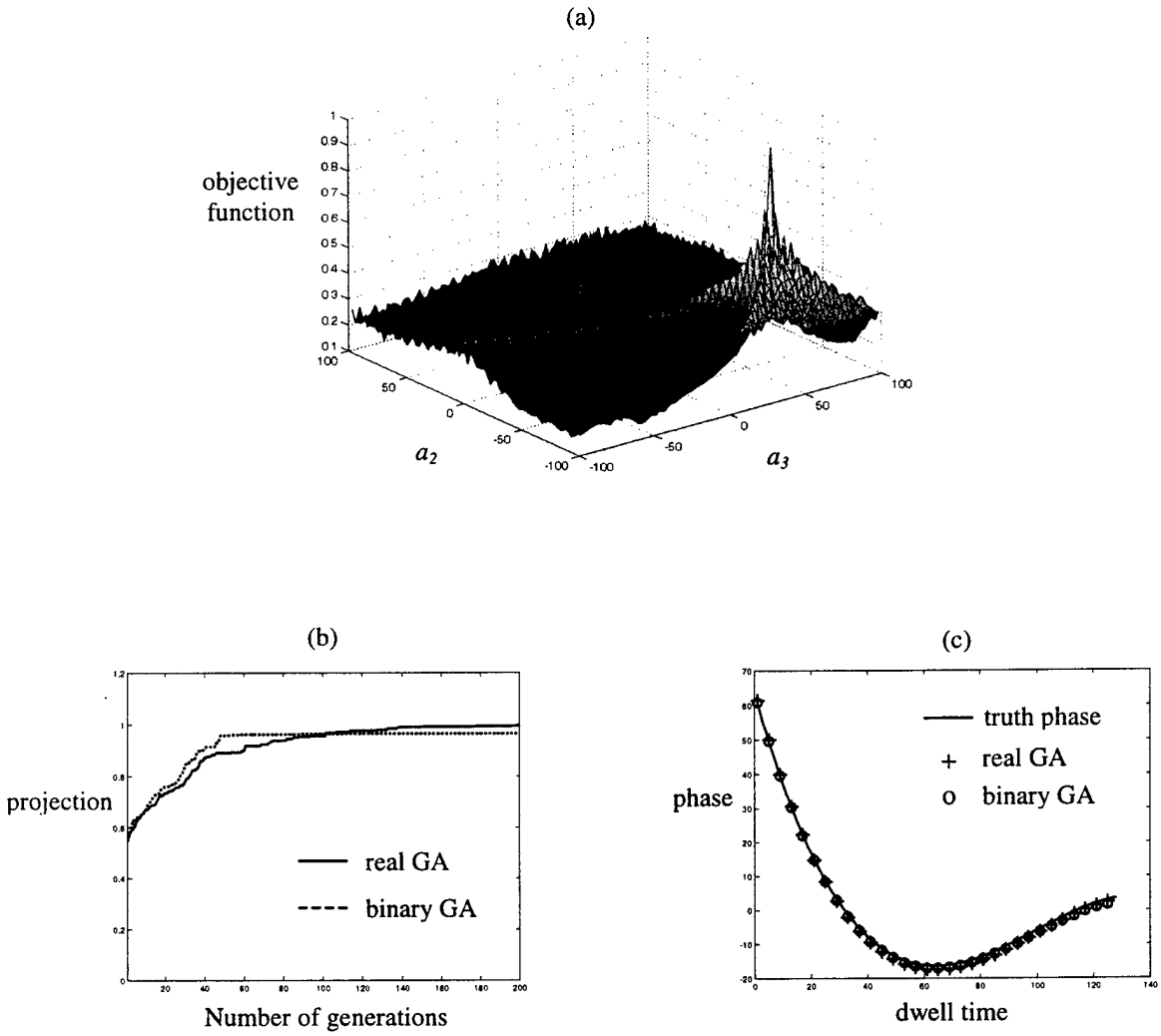

Fig. 5. GA for third-order phase estimation. (a) Multi-modal objective function. (b) GA convergence curves. (c) GA-estimated phase compared to the original truth phase.

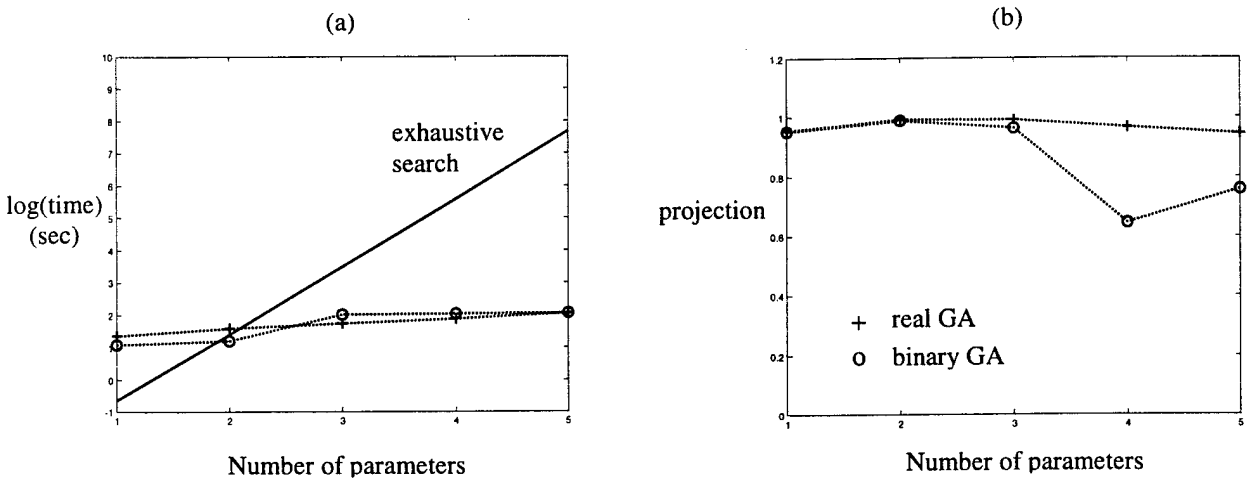

Fig. 6. Performance of GA compared to exhaustive search. (a) Computational complexity as a function of the number of parameters. (b) Accuracy.

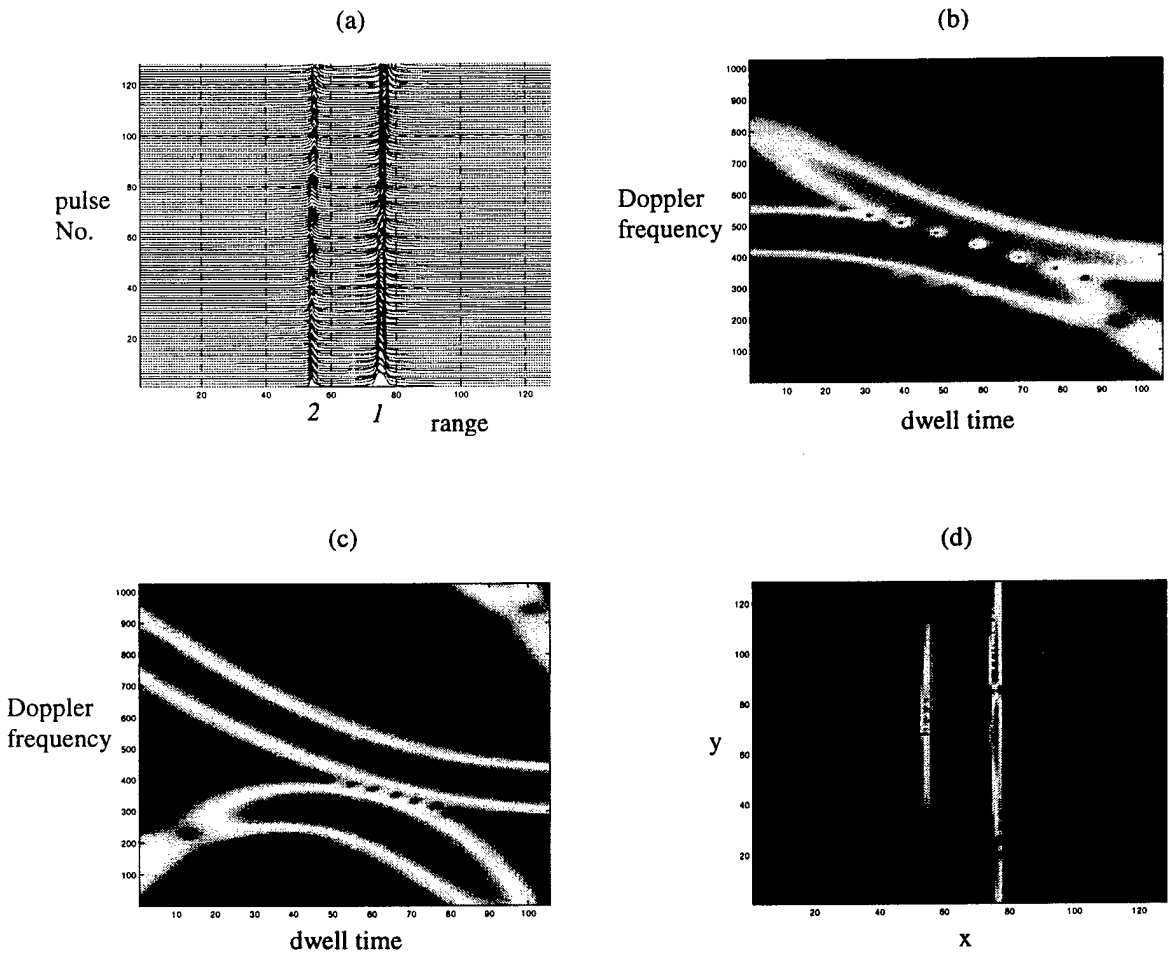

Fig. 7. Point scatterer testing using four scatterers in two range cells. (a) Range profiles prior to the fine motion compensation. (b) Spectrogram of the signal in range cell 1. (c) Spectrogram of the signal in range cell 2. (d) Resulting image via FFT processing.

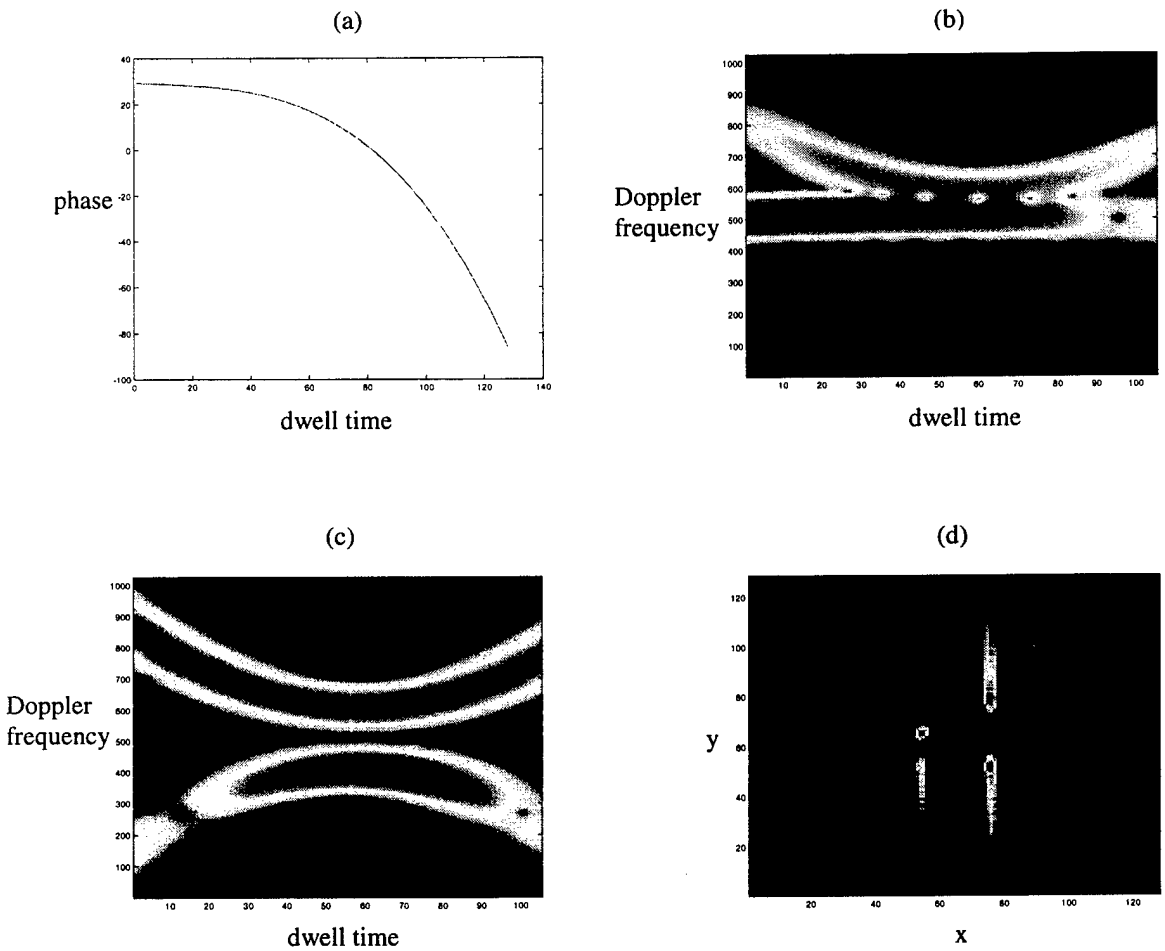

Fig. 8. Translation motion compensation using real-coded GA. (a) GA-estimated phase due to the translation motion. (b) Spectrogram of the signal in range cell 1. (c) Spectrogram of the signal in range cell 2. (d) Resulting image.

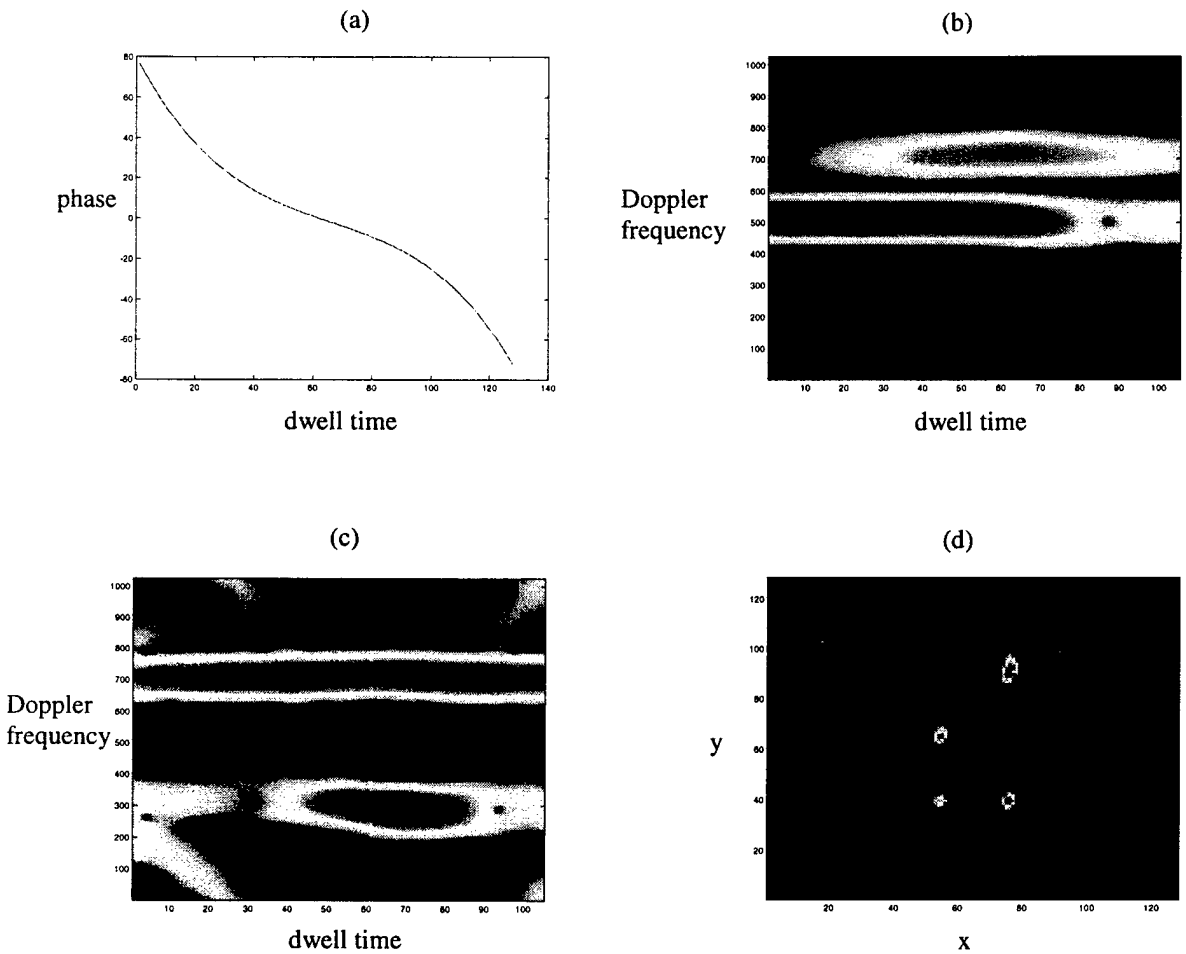

Fig. 9. Rotational motion compensation using real-coded GA. (a) GA-estimated phase due to the rotational motion. (b) Spectrogram of the signal in range cell 1. (c) Spectrogram of the signal in range cell 2. (d) Resulting image.

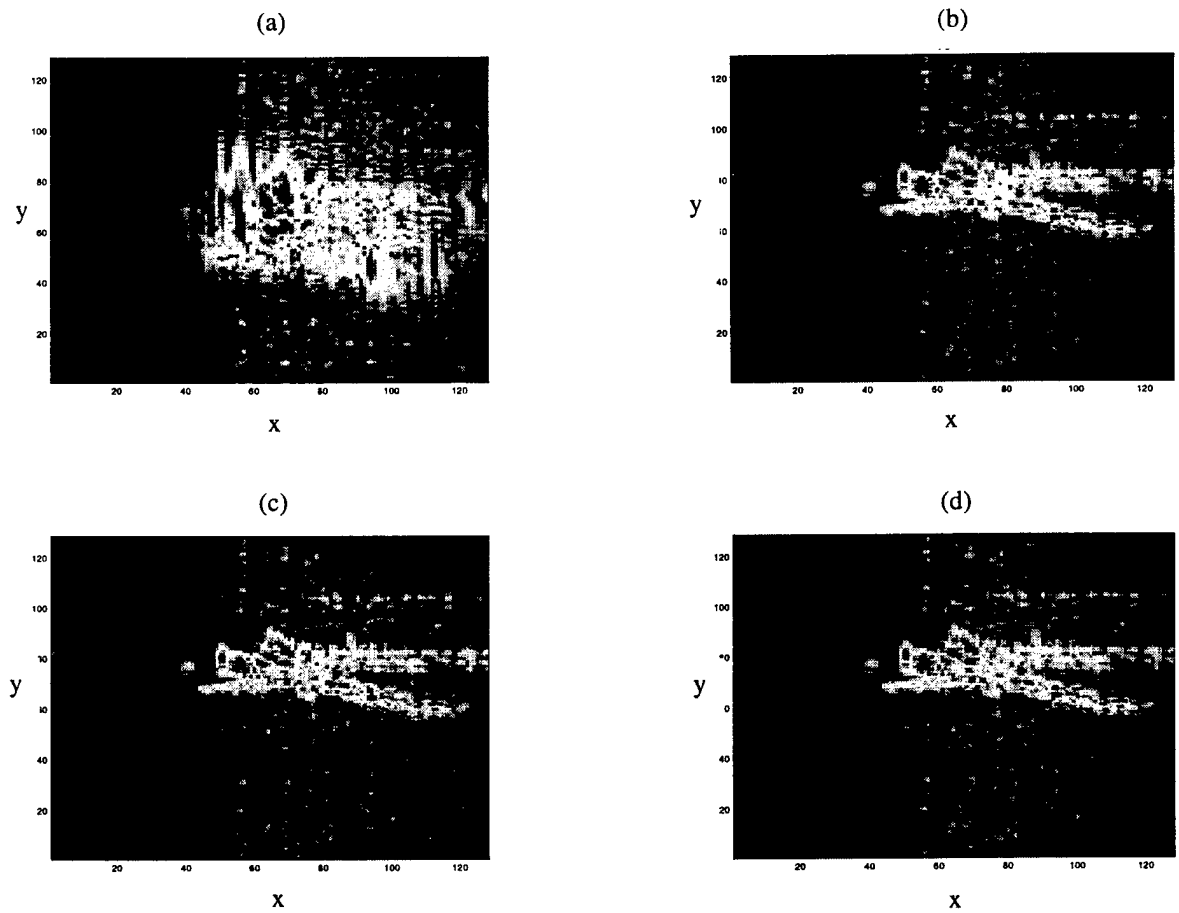

Fig. 10 Translation motion compensation applied to measurement data using a third-order motion model. (a) Image before fine motion compensation. (b) Binary-coded GA result. (c) Real-coded GA result. (d) Exhaustive search result.

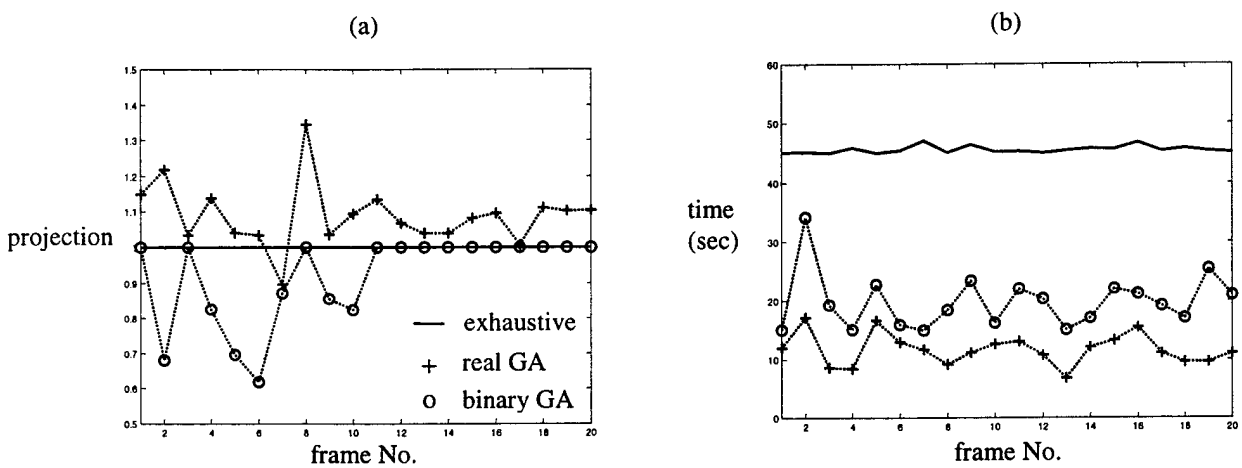

Fig. 11. Comparison of the performance of GA and exhaustive search using measurement data. (a) Projection value. (b) Computation time.

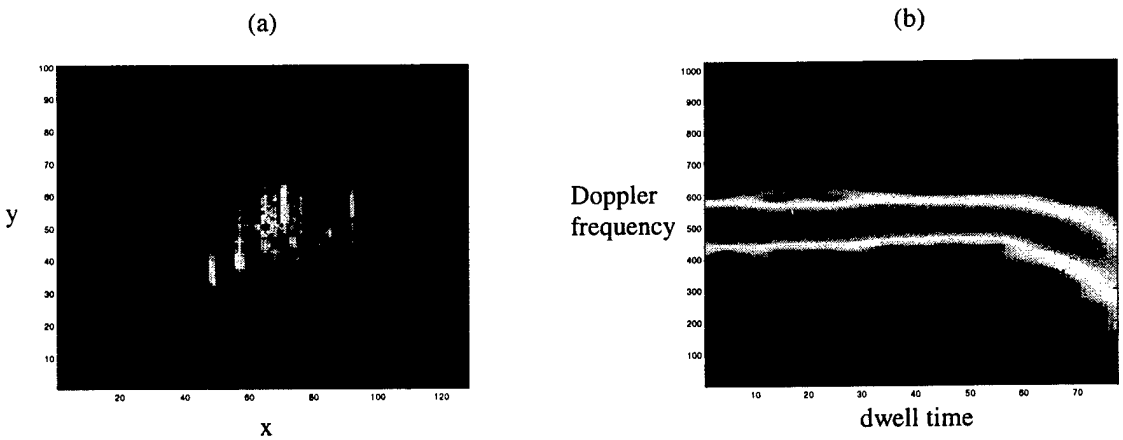

Fig. 12. Motion compensation example for another measurement data set. (a) Image after third-order translation motion compensation using real-coded GA. (b) Spectrogram of the signal in range cell 64.

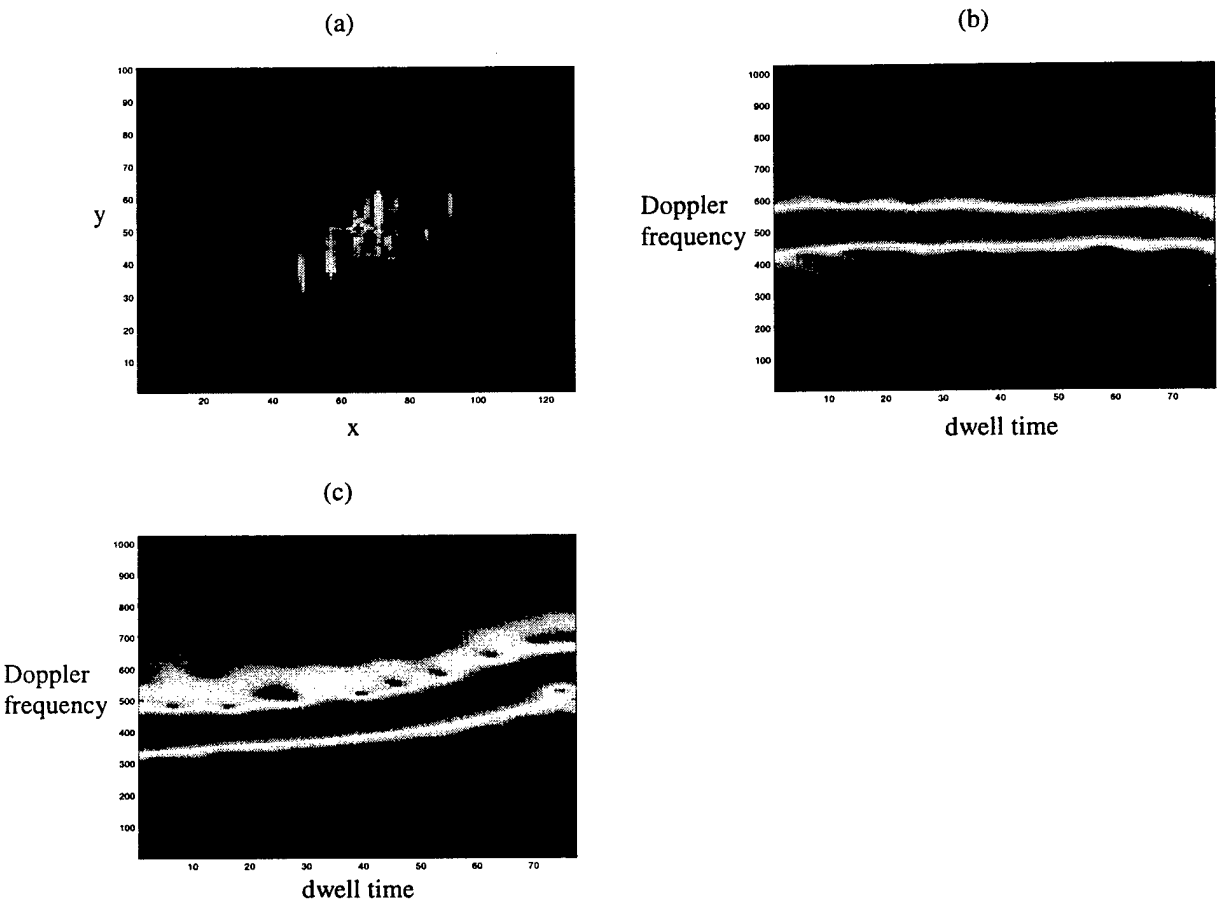

Fig. 13. Higher-order translation motion compensation. (a) Image after fourth-order translation motion compensation using real-coded GA. (b) Spectrogram of the signal in range cell 64. (c) Spectrogram of the signal in range cell 71.

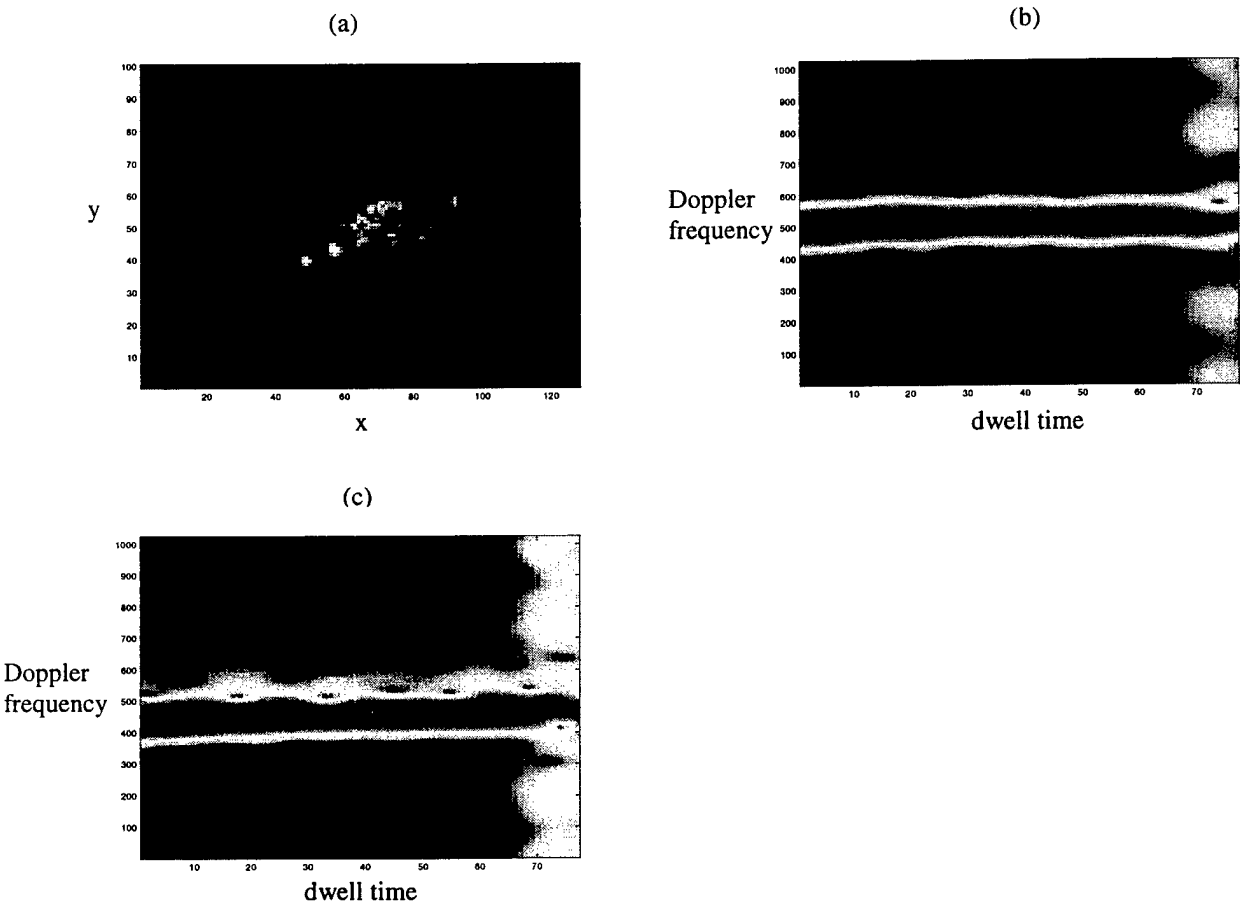

Fig. 14. Higher-order rotational motion compensation. (a) Image after fourth-order rotational motion compensation using real-coded GA. (b) Spectrogram of the signal in range cell 64. (c) Spectrogram of the signal in range cell 71.

Electromagnetic Inversion of Ipswich Objects Using the Genetic Algorithm

Yong Zhou and Hao Ling

Department of Electrical and Computer Engineering
The University of Texas at Austin
Austin, TX 78712-1084 USA

Abstract: The genetic algorithm is combined with a moment method solver to carry out the shape inversion of two-dimensional metallic objects. The binary bitmap discretization is used in conjunction with geometrical median filtering to describe the shape of the object. Results of the shape inversion using this algorithm are presented for several Ipswich objects based on measurement data.

Introduction: Inverse synthetic aperture radar (ISAR) imaging [1] is a linearized form of electromagnetic inverse scattering. While the algorithm is fast and robust in obtaining the approximate shape of an object, it suffers from resolution limitation and image artifacts due to multiple scattering phenomena. Rigorously solving the electromagnetic inverse scattering problem, on the other hand, is much more challenging. Recently, some researchers have explored the use of genetic algorithms (GA) together with computational electromagnetic solvers to attack the inverse scattering problem [2-6]. In this letter, we present results of using GA in conjunction with a method of moment (MoM) solver to invert metallic objects from the Ipswich measurement data set [7]. In particular,

we focus our attention on concave metallic objects with strong multiple scattering effects.

In the inversion of two-dimensional (2D) objects, two types of the geometrical descriptions have been used: the Fourier series scheme [2,4] and the binary bitmap discretization [3,5]. The Fourier series scheme is very efficient in representing smooth convex shapes. However, it does not work well for objects with highly concave shapes or disconnect parts. The binary bitmap discretization is a more general way to represent arbitrary 2D shapes. Its main drawback is the larger degrees of freedom required to accurately model simple shapes. More recently, cubic B-splines were also investigated as a way to accurately represent complex shapes [6]. In this work, we use the binary bitmap approach to discretize the search space. To constrain the problem, a geometrical median filter is applied to create more realizable shapes. A cost function is defined as the difference between the measured and the computed scattered fields from each assumed shape. The inverse problem is then cast into a minimization problem and genetic algorithm is applied to minimize this cost function. Three Ipswich objects, the triangular cylinder, the dihedral and the circular cavity are inverted by using this scheme. Results based on both the MoM-simulated field and the measured data are presented.

GA Scheme: In an inverse problem involving metallic objects, the measured scattering field E^{mea} from the object is known while the shape and size of the object are unknown. We apply a method of moment solution based on the electric field integral equation to obtain the rigorously computed scattered field

E^{cal} from each assumed shape. To evaluate the performance of each shape, we define the cost function as the root-mean-square (RMS) error between E^{mea} and E^{cal}.

The genetic algorithm is applied as the searching tool to minimize the cost function. In our GA implementation, the initial generation is produced randomly and each object shape is encoded into an N×N binary array with ones representing metal and zeros representing free space. A 2D median filter is used as a low-pass filter to eliminate unrealistic shapes consisting of isolated cells. With a fixed window size of M×M, the median filter slides through every cell of the binary array and sets the cell to one if the sum of the cell values within the window is greater than or equal to $M^2/2$ and zero otherwise. The median filter is applied once every several generations so that the isolated cells are cleared from time to time, while the new features created by the mutation and crossover operations have a chance to survive in the population.

The cost function for each member is then calculated and the shapes with low cost values are selected as parents to produce the next generation. A 2-point crossover scheme involving three selected parents is used. The process selects three parents and divides each parent into three parts. The three parent shapes are then intermingled to produce three children shapes. This crossover scheme exhibits a more disruptive characteristic for regeneration than the conventional one-point or two-point crossover. It serves to counteract against the median filtering effect. The mutation operation, which is applied to the individual array cells, inverts the cell according to a preset mutation rate. The

selection, crossover and mutation process is iterated until the lowest cost function in the population reaches a sufficiently small threshold or when the cost function does not decrease any more.

Results: The Ipswich measurement data was taken at a single frequency of 10GHz in the bistatic configuration. There were a total of 36 transmitter positions around the object and 18 receiver locations for each transmitter position (Fig. 1). Fig. 2a shows the shape and size of three metallic Ipswich objects selected for inversion, namely, the triangular cylinder, the dihedral and the circular cavity. They are labeled as Ips009, Ips004 and Ips011, respectively. For Ips009 and Ips011, the electric field is parallel to the axis of the target. For Ips004, the electric field is perpendicular to the axis of the target.

We first tested the inversion algorithm using MoM-simulated field data as the input. In all of the reconstructions, the number of the population was set to 100 and the crossover and mutation rates were set to 0.8 and 0.2, respectively. The search area was chosen to be 15cm×15cm for Ips004 and 12cm×12cm for Ips009 and Ips011. The number of cells within this area was set to 20×20. The reconstructed results in Fig. 2b show the final inverted shapes of the three objects. We observe that the final shapes are in fairly good agreement with the real shapes. The final RMS costs for the three objects were found to be 0.03, 0.38 and 0.18, respectively. The dihedral and the circular cavity contain strong multiple scattering and yet their inverted shapes closely resemble the correct objects. Results for these targets were also generated using

the traditional imaging method and they showed strong image artifacts due to multiple scattering.

Next, we applied the inversion algorithm to the actual measured data. Fig. 2c shows the final reconstruction shapes. As we can see, the inverted shape is good for the triangular cylinder, which has no multiple scattering effects. For the dihedral, the reconstructed shape is not continuous, but is quite similar to the real object. The circular cavity shows the most discrepancy with the real shape. The exterior and the opening of the cavity are correctly inverted, while the interior part of the cavity shape is not as satisfactory.

Interestingly, in all three inversions, we found that the final shape obtained by GA has a lower cost value than that of the exact shape (0.40 vs. 0.58 RMS error for the triangular cylinder; 0.82 vs. 0.92 for the dihedral and 0.55 vs. 0.73 for the circular cavity). This is caused by the mismatch between the measured field and the MoM-simulated field. We believe it is this difference that drove the GA to zoom onto a shape that is similar to the exact shape but has a lower cost value.

Note that the RMS error listed above is particularly high for the dihedral. We found that the agreement between the measured data and the MoM-computed data for this shape was good in the field amplitude. However, relatively large phase difference exists (even after adjusting for the rotation center) between the two results. The MoM results were also checked against other targets in the Ipswich data set and the phase agreement was found to be good. We therefore conclude that the phase data for Ips004 is suspect. As an

alternative, we also performed the inversion based on only the amplitude of the fields. The reconstructed shape is shown in Fig. 3. The quality of the reconstruction is close to that of the MoM-simulated data shown in Fig. 2(b).

Conclusion: A genetic algorithm was combined with a moment method solver to carry out shape inversion of the Ipswich measurement data. We used a binary bitmap discretization in conjunction with a geometrical median filter to describe the shape of the object. It was found that the algorithm could deal with objects containing strong multiple scattering effects.

Acknowledgment: This work is supported by the Office of Naval Research under contract No. N00014-98-1-0615.

References

1 Mensa, D. L., *High Resolution Radar Imaging,* Artech House, Dedham, MA, 1981

2 Chiu, C.C and Liu, P. T., Image reconstruction of a perfectly conducting cylinder by the genetic algorithm, *IEE Proc. - Microwave, Antennas Propag.*, Vol. 143, No. 3, 1996, pp. 249-253

3 Takenaka, T., Meng, Z. Q., Tanaka, T. and Chew, W. C., Local shape function combined with genetic algorithm applied to inverse scattering for strips, *Microwave Optical Tech. Lett.*, Vol. 16, No. 6, 1997, pp. 337-341

4 Qian, Z. and Hong, W., Image reconstruction of conducting cylinder based on FD-MEI and genetic algorithms, *IEEE Antennas Propagation Soc. Int. Symposium Digest*, 1998, Vol. 2, pp. 718 –721

5 Pastorino, M., Massa, A. and Caorsi, S., A microwave inverse scattering technique for image reconstruction based on a genetic algorithm, *IEEE Trans. Instrum. Meas.*, Vol. 49, June 2000, pp. 573 –578

6 Barkeshli, K., Mokhtari, M., and Amiri, N. M., Image reconstruction of impenetrable cylinders using cubic B-splines and genetic algorithms, *IEEE Antennas Propagation Soc. Int. Symposium Digest*, Boston, July 2001, Vol. 2, pp. 686-689

7 McGahan, R. V. and Kleinman, R. E., Second annual special session on image reconstruction using real data, *IEEE Antennas Propagat. Mag.*, Apr. 1997, Vol. 39, No. 2, pp. 7-9

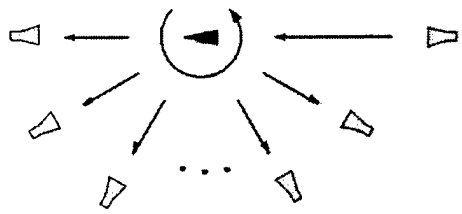

Fig. 1 *Ipswich measurement setup*

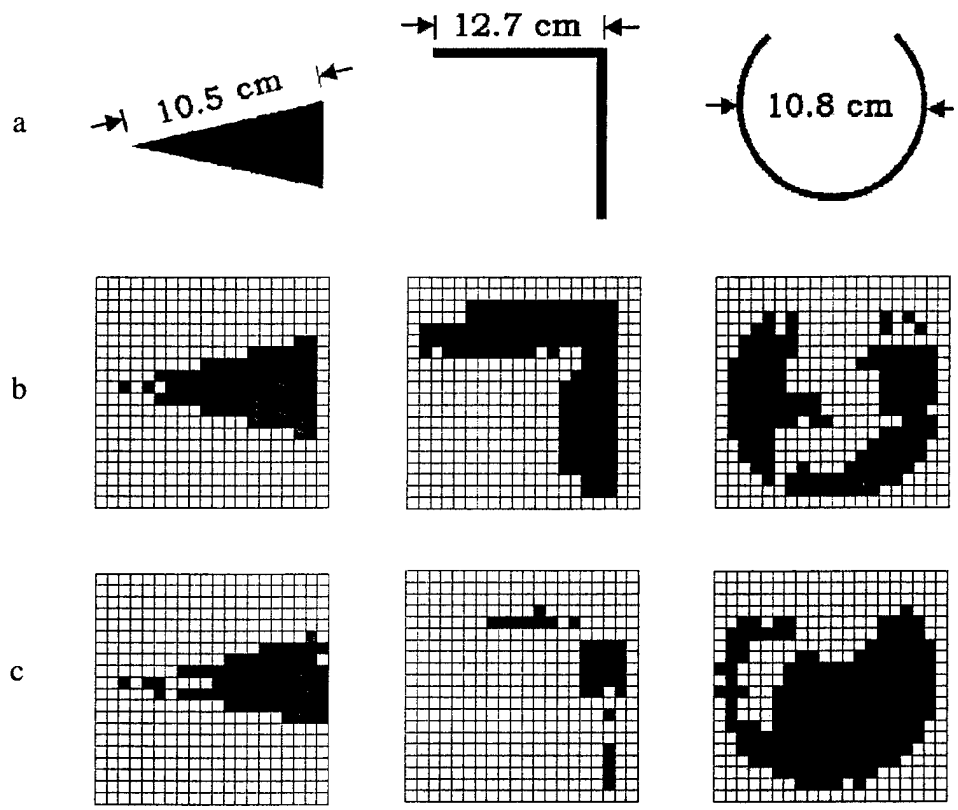

Fig. 2 *Inversion of three Ipswich objects*

a Real shapes of Ips009, Ips004 an Ips011
b Inversion based on MoM-simulated field
c Inversion based on measured complex field

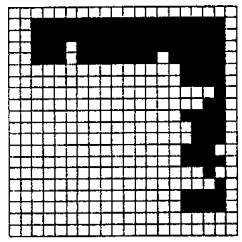

Fig. 3 *Inversion of the dihedral based on the amplitude of the measured data*

APPLICATION OF ADAPTIVE JOINT TIME-FREQUENCY PROCESSING TO ISAR IMAGE FORMATION

Hao Ling and Junfei Li

Dept. of Electrical and Computer Engineering
The Univ. of Texas at Austin
Austin, TX 78712-1084, USA

ABSTRACT

Two applications of the adaptive joint time-frequency (AJTF) algorithm for ISAR image formation are presented. First, AJTF is utilized for ISAR motion estimation and compensation. Focused images from measured radar data are presented to illustrate the effectiveness of the algorithm when applied to in-flight aircraft data. Second, the AJTF algorithm is extended to detect the presence of chaotic, three-dimensional motions in an articulating target. Preliminary test results on measured data show that the algorithm can correctly detect those imaging intervals where significant three-dimensional motions exist.

1. INTRODUCTION

High-resolution inverse synthetic aperture radar (ISAR) imaging is a promising tool for non-cooperative target identification (NCTI). The main challenge in ISAR-based NCTI is to form a well-focused image of an articulating target with unknown motion. In this paper, we first review the application of joint time-frequency methods for ISAR image formation. By using an adaptive joint time-frequency (AJTF) algorithm to estimate the phase of the prominent scatterers, we show that the target motion can be estimated and a focused image of the target can be constructed. Results of applying the algorithm to measured ISAR data are presented and discussed. Secondly, we report on our recent work to extend the AJTF algorithm to address the more challenging situation when the motion of the target is not limited to a two-dimensional plane. In particular, we discuss our research to detect the presence of three-dimensional motion using the AJTF algorithm.

2. ISAR MOTION COMPENSATION USING JOINT TIME-FREQUENCY ALGORITHM

We first review the application of joint time-frequency methods for ISAR image formation. To form a focused image from raw radar data, it is customary to first carry out a coarse alignment of the data in the range dimension, followed by fine motion compensation in the cross range dimension. Joint time-frequency techniques have been shown to be a useful tool to carry out the fine motion compensation [1,2]. We assume that after the coarse range alignment, all the scatterers are located in their respective range cells. The radar backscattered signal as a function of dwell time t in a particular range cell can be written as

$$E(t)=\sum_{k=1}^{N}A_k \exp[-j\frac{4\pi f}{c}(R(t)+x_k\cos\theta(t) + y_k \sin\theta(t))] \quad (1)$$

where N is the number of point scatterers in that range cell, and A_k, x_k, y_k are respectively the scattering amplitude, down range position and cross range position of the kth point scatterer. $R(t)$ is the residual uncompensated translation displacement and $\theta(t)$ is the rotational displacement. Due to translation and rotational motion, the Doppler frequency versus dwell time behavior of the point scatterers within this range cell is not constant in the joint time-frequency plane (see Fig. 1). An effective JTF technique to extract the motion parameters is based on a search and projection procedure to represent the phase behavior of the signal $E(t)$. This procedure is based on the adaptive spectrogram proposed in [3], and is similar in concept to a one-term matching pursuit algorithm [4]. We shall term it the adaptive JTF (AJTF) algorithm. To find the motion parameters, basis functions in the form of

$$h(t)=exp[-j(a_1t+a_2t^2+a_3t^3)] \quad (2)$$

are chosen. We search for the basis function over the parameter space (a_1, a_2, a_3) that best represents the time-frequency behavior of the signal by maximizing the projection of the signal onto the basis:

$$\max_{a_1,a_2,a_3}\left|\int E(t)h^*(t)dt\right|^2 \quad (3)$$

After the time-varying phase for the strongest point scatterer is found, we multiply the original signal by the conjugate of this phase factor to compensate for the translation motion. This algorithm can also be extended to

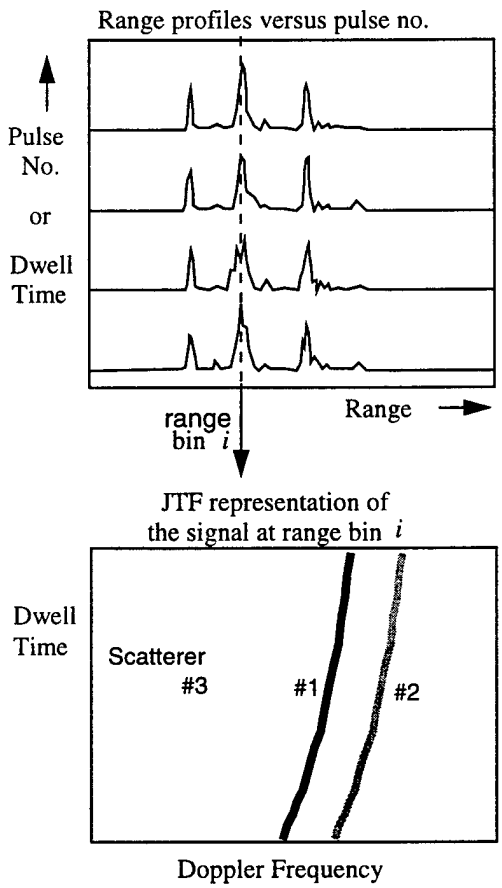

Fig. 1. Fine motion compensation is carried out by the Doppler frequency versus dwell time behavior of the strong point scatterer in the signal.

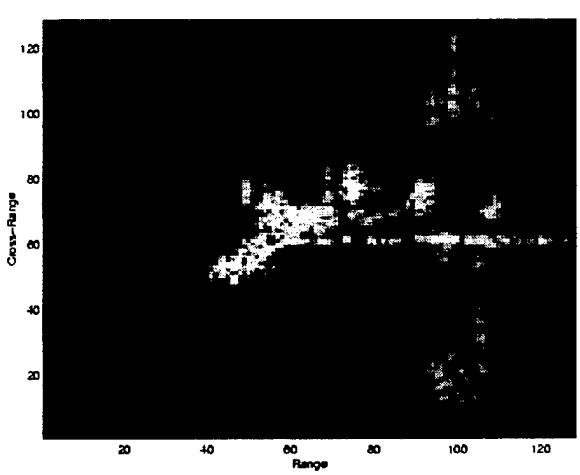

Fig. 2. ISAR image of an in-flight aircraft obtained after AJTF motion compensation.

multiple range cells to correct for higher-order rotation motion. After applying the JTF motion compensation, the standard FFT processing in the dwell time domain brings the signal into the cross range image domain. Fig. 2 shows an exmaple of applying the AJTF algorithm to measured ISAR data of an in-flight aircraft. The shape of the aircraft is clearly visible in the resulting image after the AJTF motion compensation.

3. THREE-DIMENSIONAL MOTION DETECTION USING JOINT TIME-FREQUENCY ALGORITHM

One basic assumption of standard motion compensation algorithms is that the target only undergoes motion in a two-dimensional plane during the dwell duration needed to form an image. From several independent examinations of measured ISAR data sets recently, it was reported that the presence of three-dimensional motion is quite detrimental to focusing the image [5-7]. We shall report on our recent work to extend the AJTF algorithm to address the more challenging situation when the motion of the target is not limited to a two-dimensional plane. In particular, we discuss our research to detect the presence of three-dimensional motion using the AJTF algorithm.

Allowing for arbitrary three-dimensional motion in space, we consider the following model as a generalization of the model for two-dimensional motion in (1):

$$E(t) = \sum_{k=1}^{N} A_k \exp[-j\frac{4\pi f_c}{c}(x_k + y_k\theta + z_k\phi)] \quad (4)$$

where θ is the azimuth angle of the target with respect to the radar, and ϕ is the elevation angle. In (4), it is assumed that the translation motion has been removed and that the standard small-angle, small bandwidth approximations apply. This model reduces to the standard two-dimensional motion model when θ and ϕ are linearly related.

In general, a focused image cannot be obtained from the standard two-dimensional motion compensation algorithm when three-dimensional target motion is present due to model mismatch. Therefore, it would be useful to detect the presence of three-dimensional motion directly from the radar data. Our approach is to utilize the AJTF algorithm to extract the phase behavior of the radar data at multiple range cells. We first parameterize the phase of the prominent point scatter in one range cell using AJTF. Next we repeat the same procedure at another range cell. It can be shown that when the target undergoes only two-dimensional motion during the dwell duration, the ratio between the parameters (a_1, a_2, a_3) extracted from one range cell and those corresponding parameters in another

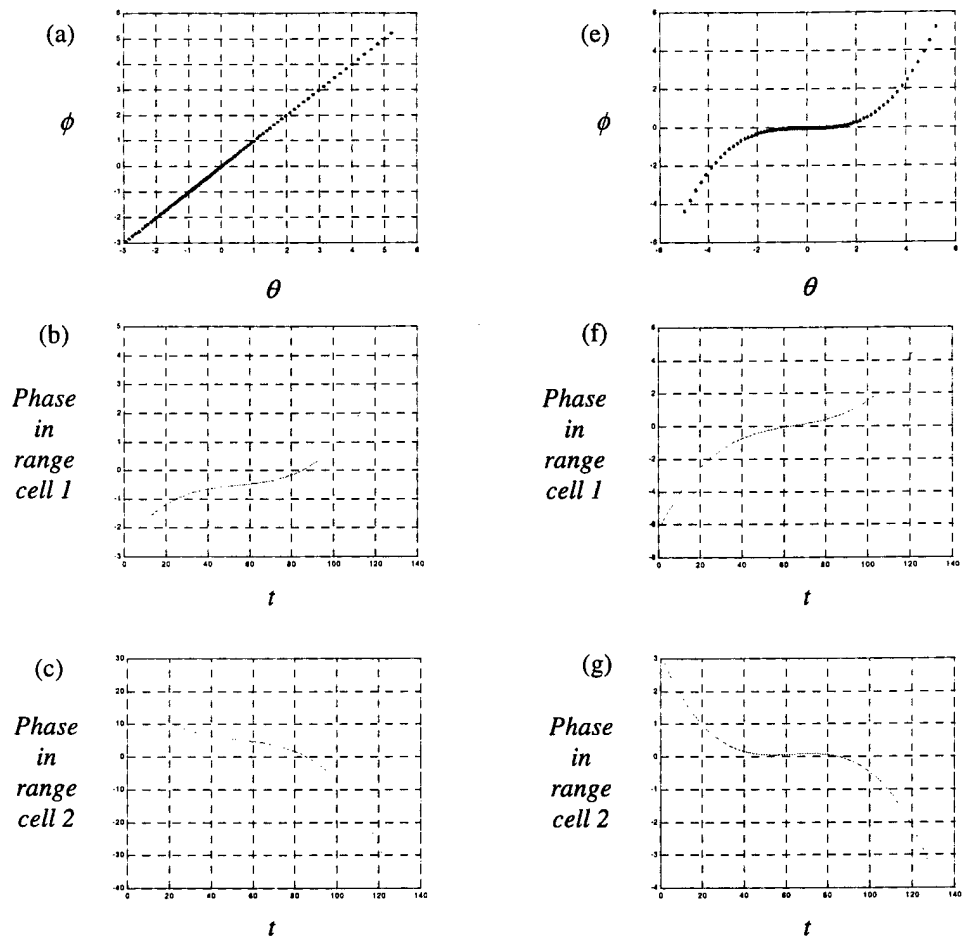

(d) c_1=-0.10
c_2=-0.10
c_3=-0.11

(h) c_1=7.20
c_2=1.60
c_3=-1.41

Fig. 3. (a) Simulated 2D target motion. (b) Phase behavior of the prominent point scatterer in range cell 1 extracted using AJTF. (c) Phase behavior of the prominent point scatterer in range cell 2 extracted using AJTF. (d) Ratios of the extracted phase parameters from the two range cells. Note that they are nearly constant. (e)-(h) Similar to (a)-(d), except that 3D motion is assumed. The resulting ratios in (h) are no longer constant.

range cell should be constant. Therefore, by examining the ratio of the parameters, we can distinguish two-dimensional motion from three-dimensional motion. Fig. 3 illustrates the idea using simulated point scatterer data. Figs. 3(a)-(d) show the two-dimensional motion scenario and Figs. 3(e)-(h) show the three-dimensional scenario. It can be seen from the results in Fig. 3(d) that the determined ratios:

$$c_i = a_i(\text{range cell } 1) / a_i(\text{range cell } 2) \qquad (5)$$

are nearly constant for all the terms in case of two dimensional motion, as expected. For three-dimensional motion, the ratios are not the same, as seen in Fig. 3(h).

Fig. 4 shows our preliminary results of applying the 3D motion detection algorithm to real radar data. Fig. 4(a) shows the degree of three-dimensional motion in the data for 20 different image frames, detected by applying our algorithm to the raw radar data. As a reference for comparison, Fig. 4(b) shows the degree of three-dimensional motion for the same 20 frames measured using the motion data derived from inertial navigation instruments carried onboard the aircraft during data collection. It can be seen that our algorithm correctly detects where significant three-dimensional motions exist. We are currently fine tuning the algorithm to achieve faster and more robust detection. We believe this detection algorithm could be quite useful for determining the "good"

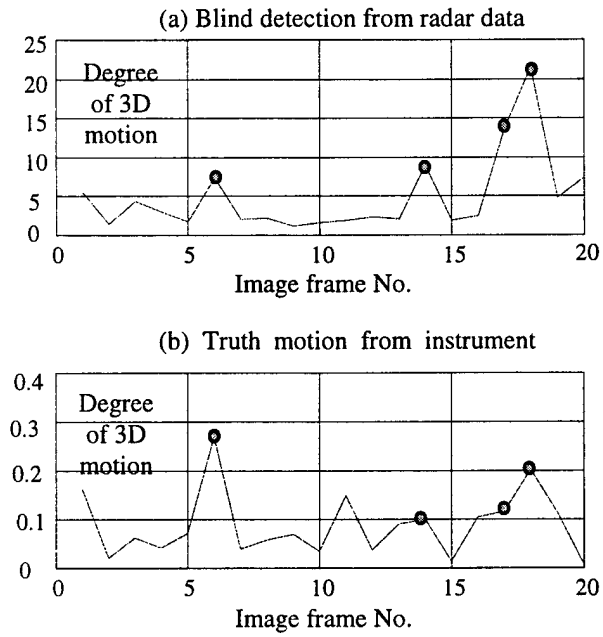

Fig. 4. Blind detection of three-dimensional motion from real radar data. (a) Degree of three-dimensional motion over 20 image frames detected using the proposed algorithm. (b) Degree of three-dimensional motion measured from on-board instrument data.

imaging intervals from which focused images can be more readily generated. For targets that exhibit very chaotic motions, such as ships on the ocean, finding such intervals of opportunity may be very critical for target recognition.

4. SUMMARY

In this paper, we presented two applications of the adaptive joint time-frequency algorithm for ISAR image formation. In the first application, we carry out fine motion compensation to form focused ISAR images of articulating targets. The AJTF algorithm is used to estimate the phase of the prominent point scatterer within a range cell. The higher-order phase error due to uncompensated translation and rotational errors are then removed prior to the image formation. Results show that well-focused images can be obtained from measured data of an in-flight aircraft. In the second application, we try to detect the presence of three-dimensional target motion, for which a well-defined imaging plane does not exist. A three-dimensional motion model is utilized and the linearity of the phase functions of the prominent point scatterers between different range cells is used to distinguish two-dimensional from three-dimensional motion. The AJTF engine is again used to extract the phase function of the prominent scatterer within each range cell. Preliminary test results using real radar data indicate that the algorithm can be used to detect those imaging intervals where conventional two-dimensional motion assumption would fail. We are working to devise algorithms for forming focused images even in the presence of these three-dimensional motions.

5. ACKNOWLEDGMENT

This work is supported by the Office of Naval Research under Contract No. N00014-98-1-0615.

6. REFERENCES

[1] V. C. Chen, "Reconstruction of inverse synthetic aperture images using adaptive time-frequency wavelet transforms," *SPIE Proc. on Wavelet Application*, vol. 2491, pp. 373-386, 1995.

[2] Y. Wang, H. Ling and V. C. Chen, "ISAR motion compensation via adaptive joint time-frequency technique," *IEEE Trans. Aerospace Electron. Syst.*, vol. 34, pp.670-677, Apr. 1998.

[3] S. Qian and D. Chen, "Signal representation using adaptive normalized Gaussian functions," *Signal Processing*, vol. 36, no. 1, pp. 1-11, Mar. 1994.

[4] S. G. Mallat and Z. Zhang, "Matching pursuits with time-frequency dictionaries," *IEEE Trans. Signal Processing*, vol. 41, pp. 3397-3415, Dec. 1993.

[5] V.C. Chen and W. J. Miceli, "Effect of roll, pitch and yaw motions on ISAR imaging," *SPIE Proc. on Radar Processing*, vol. 3810, July 1999.

[6] A. W. Rihaczek and S. J. Hershkowitz, "Choosing imaging intervals for identification of small ships," *SPIE Proc. on Radar Processing*, vol. 3810, July 1999.

[7] J. Li, Y. Wang, R. Bhalla, H. Ling and V. C. Chen, "Comparison of high-resolution ISAR imagery from measured data and synthetic signatures," *SPIE Proc. on Radar Processing*, vol. 3810, July 1999.

ISAR motion detection and compensation using genetic algorithms

Junfei Li and Hao Ling

Dept. of Electrical and Computer Engineering,
The Univ. of Texas at Austin, Austin, TX 78712-1084

ABSTRACT

Based on the point scatterer model, a radar signal can be effectively analyzed using the joint time-frequency (JTF) method. The basis functions of a few prominent point scatterers are believed to carry target motion information essential to the ISAR imaging process. One major problem with the JTF method is the computation load associated with the exhaustive search process for motion parameters. In this paper, genetic algorithms (GA) are used to for the parameterization process in the JTF method. Real and binary coded GA are investigated and their performance compared with the exhaustive search. It is shown that a significant amount of time can be saved while achieving almost the same image quality by using real-coded GA.

Keywords: inverse synthetic aperture radar (ISAR) imaging, motion compensation, joint time-frequency technique, genetic algorithm

1. INTRODUCTION

High-resolution inverse synthetic aperture radar (ISAR) imaging is a promising tool for non-cooperative target recognition.[1,2] It utilizes the motion of a moving target to generate the necessary cross-range resolution in forming an image. Ideally, the desired target motion is uniform rotation without translational motion, under which a two-dimensional Fourier transform converts the radar data in the (frequency)-(dwell time) domain into the (range)-(Doppler frequency) domain. Otherwise, motion compensation is needed as an intermediate step to form a focused ISAR image. Since target motion can always be decomposed into translational motion and rotational motion, a typical motion compensation algorithm consists of two steps. First, a point on the target is focused through translational motion compensation. When there is non-uniform rotational motion, other points on the target are not necessarily focused. Rotational motion compensation is then applied to focus these other points.

Recently, we proposed an ISAR motion compensation algorithm based on joint time-frequency (JTF) analysis.[3] The basic idea is to extract the phase of the prominent point scatterer within a range cell via a JTF projection technique. The data is systematically projected onto a set of basis functions to determine the one that best resembles the joint (dwell time)-(Doppler frequency) behavior of the strongest point scatterer in the range cell. We use polynomial functions as the phase function of the basis. Once the phase functions of two point scatterers are found by JTF analysis, both translational and rotational motion compensation can be achieved with good accuracy. However, because the phase parameters are obtained by an exhaustive search, the algorithm requires heavy computation load if high order polynomials are used. Therefore, the algorithm is not practical in dealing with cases where higher order target motions are involved.

In this paper, the genetic algorithm (GA)[4] is explored as an alternative to the exhaustive search in the JTF procedure. GA is a stochastic optimization method based on the principle of natural selection and evolution. A set of trial solutions forming an initial population is updated iteratively using crossover and mutation operators. From one generation to the next, the overall performance of the population is improved. Like exhaustive search, GA is a global optimization procedure. However, it is capable of finding the optimum in a very high-dimensional space in a much more efficient manner than exhaustive search. This paper is organized as follows. Section 2 gives a summary of the JTF motion compensation technique for ISAR imaging. The concept of translational and rotational motion compensation is introduced based on the point scatterer model. Genetic algorithm is described in Section 3. The general GA procedure and some issues specific to the motion parameter estimation problem are discussed. ISAR imaging results using some real-world data by the proposed JTF/GA method are shown in Section 4. Conclusions are given in the final section.

2. JOINT TIME-FREQUENCY MOTION COMPENSATION

The joint time-frequency projection technique[3] is used to estimate the phase of a prominent point scatterer. We begin with coarsely aligned radar range profiles over a certain dwell interval. Within a fixed range cell, the data can be written as

$$E_s(t_D) = \sum_{i=1}^{Nr} \sigma_i \exp(-j\frac{4\pi f_c}{c}(r(t_D) + x_i + y_i\varphi(t_D))) \tag{1}$$

where f_c is the radar center frequency, t_D is the dwell time, φ is the target aspect angle, and r describes the residual translational motion. The ith point scatterer is located at (x_i,y_i) with σ_i as its complex scatterering strength. Among the N_r point scatterers within the range cell, we express the phase behavior of the strongest one as a polynomial function:

$$P_M(t_D) = (f_1 t + f_2 t^2 + f_3 t^3 + ..) \tag{2}$$

and consider

$$h(t) = \exp[-jP_M(t_D)] \tag{3}$$

as a basis for the radar signal. The phase parameters are then found by searching for the maximum projection from the radar signal onto the basis function:

$$< f_1, f_2, f_3, ... >= \arg\max | \int E_s(t_D) h^*(t_D) dt_D | \tag{4}$$

In the search procedure, the first term f_1 can be obtained using the fast Fourier transform, while all higher order terms f_2, f_3, ... are obtained using exhaustive search. Figure 1 illustrates the process of JTF phase estimation. Figure 1(a) shows the coarsely aligned range profiles. Figure 1(b) shows the joint (dwell time)-(Doppler frequency) behavior of the radar signal in range cell r_0. It contains three point scatterers. The tilted trajectory of the prominent point scatterer 1 implies there exist higher-order terms in the phase function. Figure 1(c) shows the basis function $h(t_D)$. During the search, we change the position (f_1), tilting (f_2) and curvature (f_3, ...) of h until the projection of h onto the radar signal is maximized.

In order to carry out both translational and rotational motion compensation, the JTF phase estimation is needed for at least two prominent point scatterers from two different range cells. After phase estimation of the first point scatterer, we multiply its conjugate phase to the data to accomplish translational motion compensation. As we can see from Figures 2(a) and 2(b), the trajectory of the first point scatterer in the JTF plane is straightened to a horizontal line after the translational motion compensation. This point becomes focused in the image and serves as the origin of the remaining rotational motion. After phase estimation of the second point scatterer, we resample the phase function to make it into a linear function of dwell time. As shown in Figure 2(c), the JTF behaviors of both point scatterers become horizontal lines in the JTF plane and the whole target can be focused in the image. The main computational issue involved in this algorithm is an efficient strategy for the phase estimation problem in equation (4). Exhaustive search is very computationally intensive, and makes motion compensation of targets with higher order motions prohibitive.

3. GENETIC ALGORITHM

We explore the use of genetic algorithm (GA) to improve the computational efficiency of exhaustive search. GA is a global optimization method based on the concepts of natural selection and evolution.[4-5] The stochastic characteristic of GA makes it less vulnerable to local optimums as in deterministic optimization algorithms. Since GA is based on a set of population instead of one single possible solution, this helps the algorithm to find the global optimum more easily for a complex object function with many local optimums. Another advantage of GA is its robustness.

Figure 3 shows the flowchart of a simple genetic algorithm. It consists of three steps: 1) Initialization. Because the GA result is quite independent of the initial state, usually the initial population consists of random individuals. 2) Selection. Selection is based on the fitness of the individual. Individuals in the population are sorted according to the objective function evaluated at the corresponding optimization parameters. According to some stochastic strategy, two or more parents are selected to generate children. 3) Reproduction. In the reproduction stage, crossover and mutation operators are used to generate new individuals from the selected individuals. The crossover operation produces children genetically similar to parents. This ensures that good features in the solution are kept from one generation to the next. The mutation operation generates a child that is different from the parent. Better solutions containing features not included in the parent population are made possible by the added diversity from mutation.

After a new population is generated by a series of selection, crossover and mutation operations, the selection and reproduction processes are iterated until a preset convergence criterion is met. There are several choices for the convergence criterion. For example, if we know the true optimal objective function, an RMS error might be set to ensure the solution is accurate enough. In case we do not know the truth value, we might set a fixed generation number to balance the solution performance with the computational cost. A third option is to stop the process when GA has reached its saturation point. Typically, the rate of convergence is fast in the beginning. When GA has run for a long time and the solution performance does not improve much, we can choose to stop the process.

GA operates on coded parameters instead of the parameters themselves. A coded parameter is called a gene, and the string of genes to represent a set of optimization parameters is called a chromosome. While in traditional GA the parameters are usually binary coded, real-coded GA has also been developed and utilized.[6] Binary GA utilizes discrete binary bits to represent the parameters. Real GA utilizes continuous real numbers to represent the parameters. The main differences in the algorithms of binary versus real GA are the crossover and mutation operators depicted in Figure 4. In Figure 4(a) depicting binary GA, each chromosome consists of 8 bits. To make the crossover, 4 bits from the first parent are combined with 4 bits from the second parent to form a child. To make the mutation, the content of a random bit is flipped. In Figure 4(b) depicting real GA, crossover and mutation are defined as simple additions. The crossover operator is a linear combination of the two parents, where α is a random number between 0 and 1. The mutation for real GA adds some randomness to an individual chromosome by adding a random vector β to it. In case the mutated result is out of the search space, the mutation operator is repeated until an acceptable value is found. While either binary or real GA can be applied to an optimization problem, it appears to us that in problems involving continuous parameters, real-coded GA may achieve better solution performance than binary GA, since the binary search space is limited in resolution. Both the real-coded and binary-coded GA are tested for the phase estimation problem.

4. RESULTS

To test the accuracy of the GA search for the phase estimation problem, a phase function with 3rd order behavior is used to generate a set of simulated data. Real-coded GA is utilized to estimate the phase coefficients. In our GA, we use 50 chromosomes in the population. The crossover probability is 0.7 and the mutation probability is 0.3. The objective function O is defined as the projection value from the data onto the basis. Figure 5(a) shows the convergence curve of one GA run. It is seen that after 200 generations the projection value error of the best individual is 3%, while after 400 generations the error is about 1%. Figure 5(b) shows the truth phase function and the phase function obtained from the GA-searched parameters after 400 generations. The GA phase result is nearly indistinguishable from the truth phase.

Next, we investigate the computational complexity of the GA search as the number of search parameters is increased. This is shown in Figure 6, where the computation time is plotted as a function of the parameter number for both GA and exhaustive search. As the dotted curve shows, the computation time for exhaustive search increases dramatically with the number of parameters. The solid curve is for the real-coded GA search and it grows much slower than the exhaustive search. This means we can use GA to carry out the search much more efficiently when a large number of parameters is involved.

Finally, we test the GA search for the JTF phase estimation problem with a real radar data set.[7-8] There is no significant rotational motion of the target in this data so the phase estimation of only one point scatterer is needed. Imaging results from real-coded GA are compared to those from binary-coded GA and exhaustive search. Figures 7(a)-(c) show images generated for a typical frame using exhaustive search, binary-coded GA and real-coded GA, respectively. The corresponding computation time is 45 s, 22 s, and 16 s. In the 20 frames we examined, it is found that in 19 frames, the real-coded GA gave larger projection values than exhaustive search. The resulting image quality is either on par or slightly better than those

obtained from the exhaustive search, while the computation time is about 1/3 to 1/9 of the exhaustive search. For the binary-coded GA, 8 frames are found to be of inferior image quality than the exhaustive search result. Therefore, real-coded GA appears to be the better choice for the JTF motion compensation problem at hand.

5. CONCLUSIONS

One problem with JTF-based ISAR imaging is the time complexity associated with the exhaustive search process. In this paper, GA is used to replace the exhaustive search process in the JTF phase estimation for higher efficiency. It is shown that the real-coded GA achieves almost the same image quality while saves computation time significantly. With GA, the computation time complexity for higher order motion is much smaller than that of exhaustive search. Therefore, GA is a good candidate for performing ISAR motion compensation of targets with higher order motion.

ACKNOWLEDGEMENT

This work is supported by the Office of Naval Research under Contract No. N00014-98-1-0615.

REFERENCES

1. C. C. Chen and H. C. Andrews, "Target motion induced radar imaging," *IEEE Trans. Aerospace Electron. Syst.*, vol. 16, pp.2-14, Jan. 1980.
2. A. Ausherman, A. Kozma, J. L. Waker, H.M. Jones and E. C. Poggio, "Developments in radar imaging," *IEEE Trans. Aerospace Electron. Syst.* vol. 20, pp.363-400, Apr. 1984.
3. Y. Wang, H. Ling and V. C. Chen, "ISAR motion compensation via adaptive joint time-frequency technique," *IEEE Trans. Aerospace Electron. Syst.*, vol. 34, pp.670-677, Apr. 1998.
4. D. E. Goldberg, *Genetic Algorithms in Search, Optimization and Machine Learning*, Addison-Wesley, Reading, MA, 1989.
5. Y. Rahmat-Samii and E. Michielssen, ed., *Electromagnetic Optimization by Genetic Algorithm*, John Wiley & Sons, New York, 1999.
6. D. E. Goldberg, "Real-coded genetic algorithms, virtual alphabets and blocking," *Complex Syst.* vol. 9, pp.193-212, 1996.
7. H. Ling, Y. Wang, J. Li, R. Bhalla and V.C. Chen, "ISAR image formation of TIRA data using adaptive joint time-frequency processing," *NATO Sensors and Electronics Technology Symposium on High Resolution Radar Techniques*, Granada, Spain, Mar. 1999.
8. J. Li, Y. Wang, R. Bhalla, H. Ling, and V. C. Chen, "Comparison of high-resolution ISAR imagery from measured data and synthetic signatures," *SPIE Proc. On Radar Processing*, vol. 3810, July 1999.

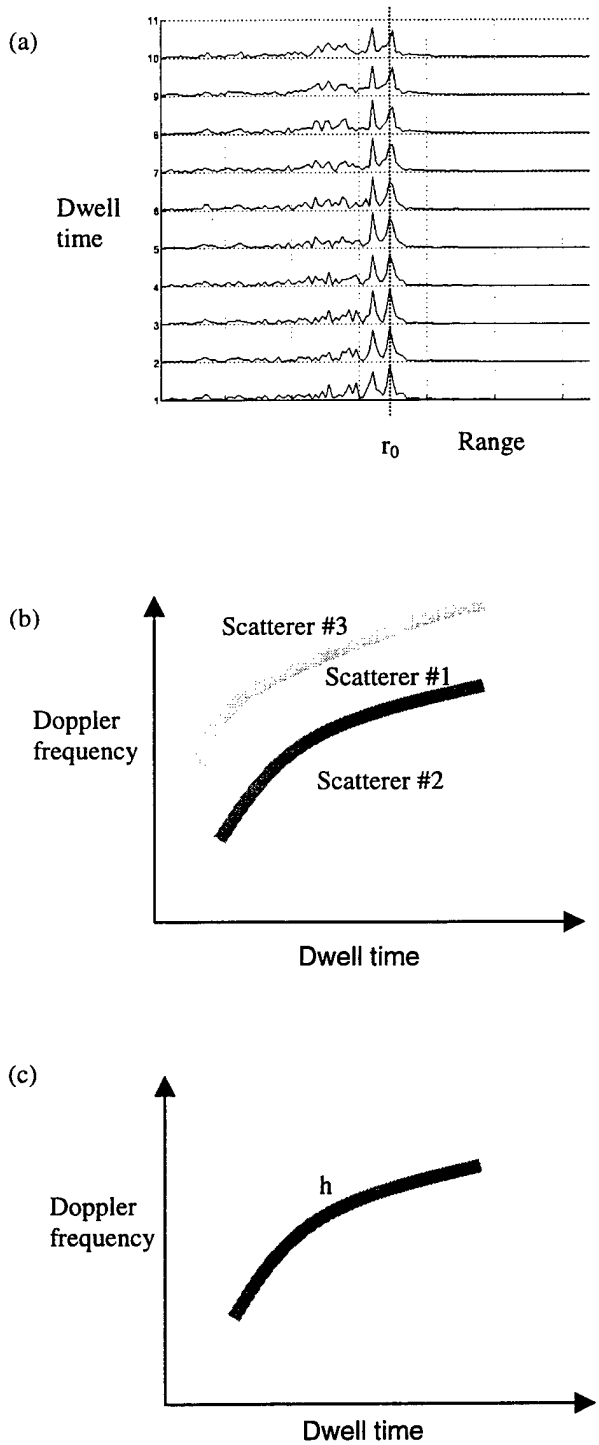

Fig.1. Joint time-frequency analysis of radar signal. (a) Range profiles versus dwell time. (b) Joint (dwell-time)-(Doppler frequency) representation of the radar signal within range cell r_0 showing several point scatterers. (c) Phase of the strongest point scatterer is found by projecting the radar signal onto the best

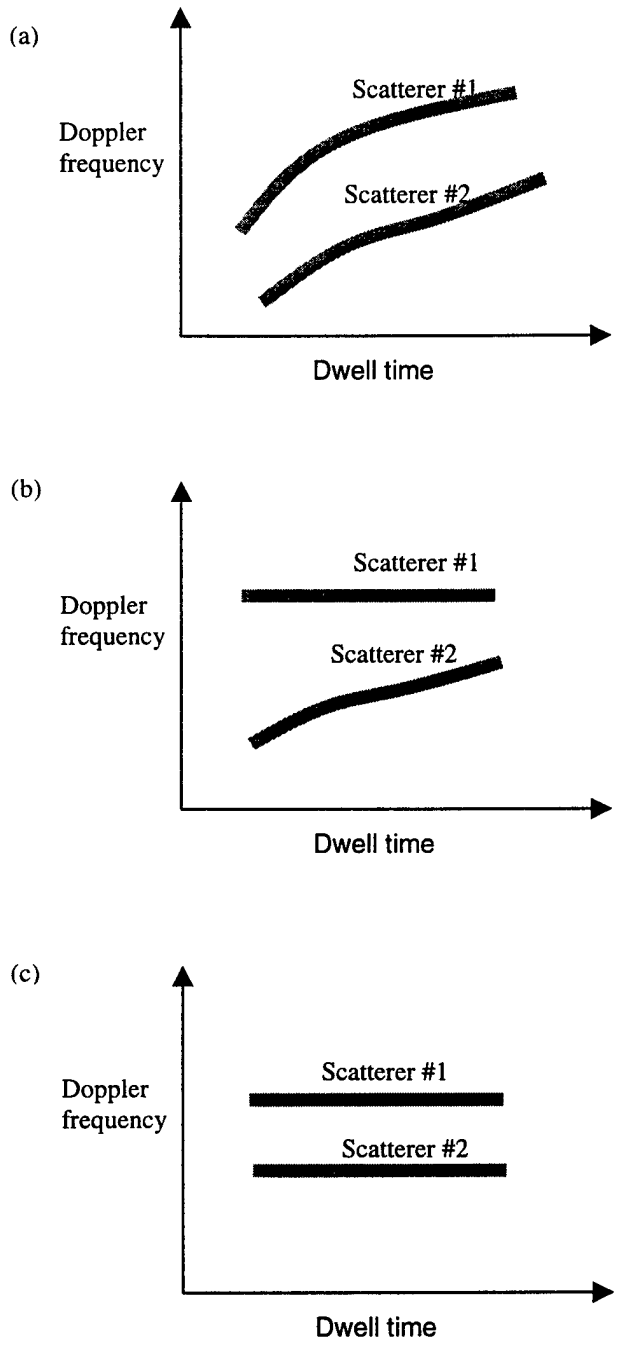

Fig.2. Translational and rotational motion compensation by JTF. (a) JTF display of the uncompensated radar signal with two prominent point scatterers. (b) After translational motion compensation. (c) After tranlsational and rotational motion compensation.

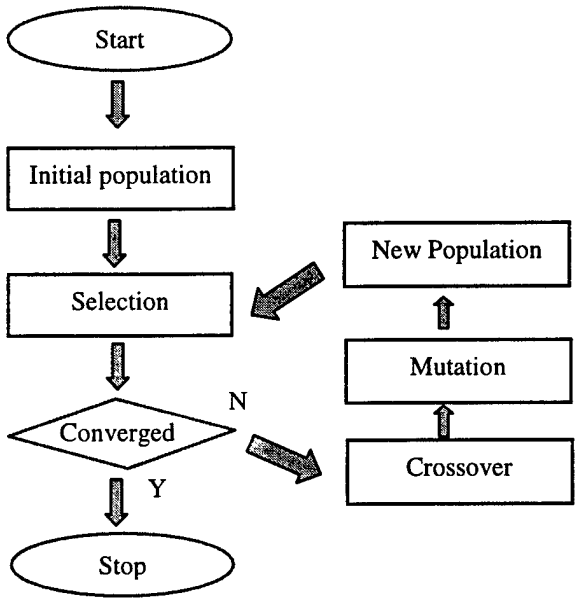

Fig.3. Flow chart of a simple genetic algorithm

(a)

Crossover **1 0 1 1 1 1 0 1** } **1 0 1 1** *1 0 1 0*
0 1 1 0 1 0 1 0 } *0 1 1 0* **1 1 0 1**

Mutation **1 0 1 1 1 1 0 1** → **1 0 0 1 1 1 0 1**

(b)

Crossover $\mathbf{C_1}$ } $\alpha\mathbf{C_1}+(1-\alpha)\mathbf{C_2}$
$\mathbf{C_2}$ } $(1-\alpha)\mathbf{C_1}+\alpha\mathbf{C_2}$

Mutation $\mathbf{C} \rightarrow \mathbf{C}+\beta$

Fig.4. Examples of crossover and mutation operations in binary and real-coded GA.
(a) Binary GA. (b) Real GA.

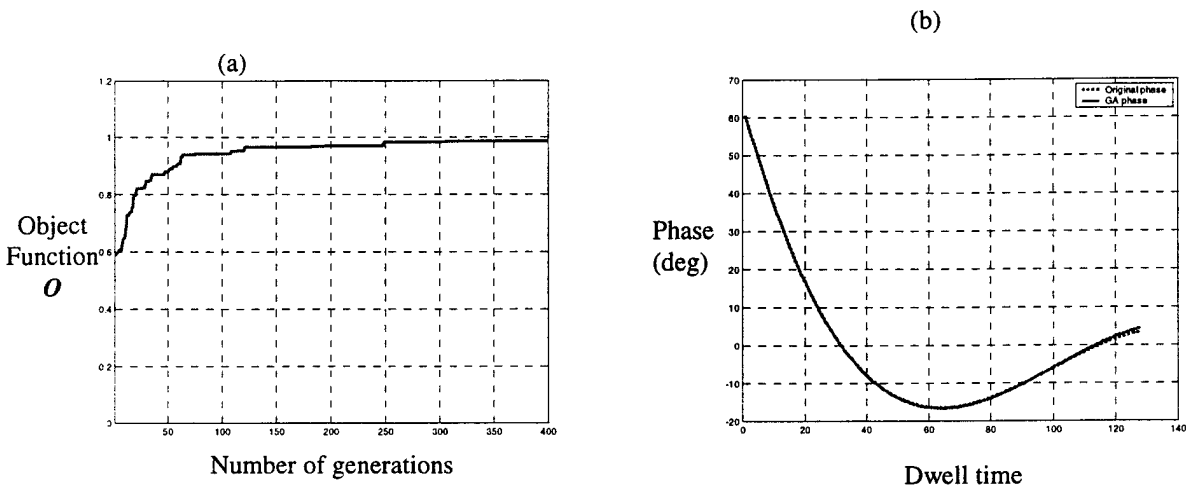

Fig.5. Behavior of a typical GA run for phase estimation. (a) Convergence curve. (b) GA phase comparison with the original truth phase.

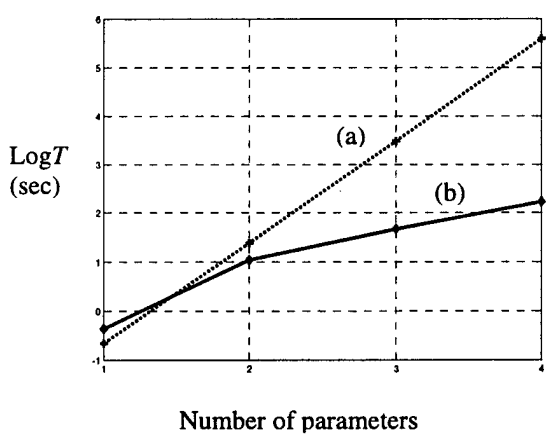

Fig.6. Computation time comparison. (a) Exhaustive search. (b)Real GA.

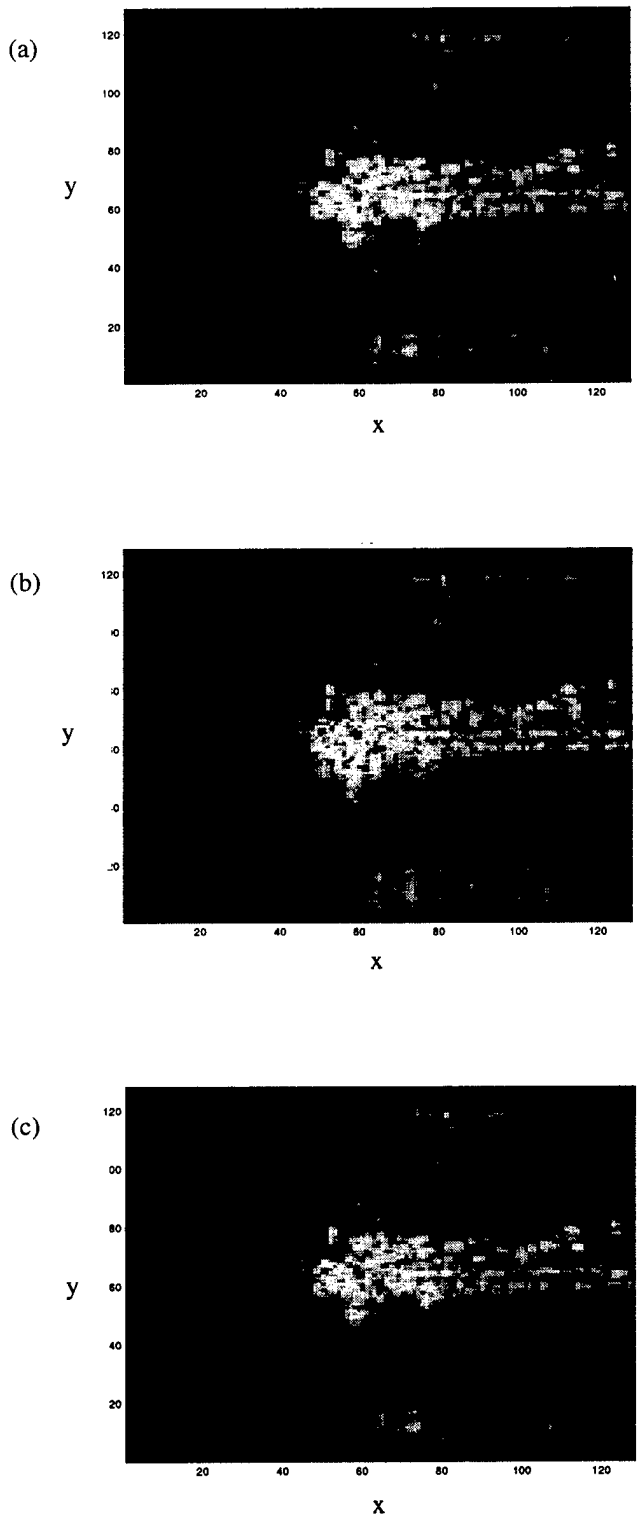

Fig.7. Resulting radar images after motion compensation from real data.
(a) Exhaustive search. (b) Binary GA. (c) Real GA.

Micro-Doppler Feature Extraction from ISAR Data Using Adaptive Chirplet Representation

Junfei Li and Hao Ling
Department of Electrical and Computer Engineering
University of Texas at Austin
Austin, TX 78712

Abstract

With the assumption of rigid body motion, traditional high-resolution ISAR imaging is capable of generating a (range)-(cross range) image of the target. When the target has non-rigid body motion, the resulting radar image does not preserve the spatial features of the target. In this paper, we investigate the extraction of micro-Doppler features due to non-rigid body motions. Joint time-frequency analysis with adaptive chirplet basis functions is employed to represent the range compressed radar data. After the parameterization, returns from different moving parts on the target can be easily separated. The algorithm is applied to analyze the measurement data from a walking man. It is shown that the rate of the arm swing can be accurately estimated after the extraction.

1. Introduction

In inverse synthetic aperture radar (ISAR), the backscattered data from a moving target is collected and processed with a motion compensation algorithm to generate a (range)-(cross range) image of the target. Since the image is a 2-dimensional projection of the target, spatial features present in the image are useful for target identification

purpose [1]. A basic assumption in ISAR imaging is that the target is a rigid body during the data acquisition time.

However, non-rigid body motions (associated with a target which is not a rigid body) can exist in many real targets. For example, a target may consist of multiple movable components. In such cases, a focused ISAR image resembling the original target cannot be obtained by the tradition ISAR processing. On the other hand, while the geometrical relationship is difficult to capture, motion features are still embedded in the radar data. Recently, the term micro-Doppler has been coined to describe the small motion features of a non-rigid target [2]. Micro-Doppler provides an additional feature to the Doppler return from the main body motion, and has been studied for identifying the natural resonant frequency of a tractor-trailer truck [3].

In this paper, we investigate the problem of micro-Doppler feature extraction from ISAR data. The approach we use is adaptive joint time frequency (AJTF) analysis [4,5], with chirplet as the basis function to represent the signal [6]. This work is an improvement of the work reported in [7], where chirp basis functions with constant amplitude were used to model the radar return from a helicopter. We apply the algorithm to the radar data from a walking man and extract micro-Doppler features due to the swinging arms.

2. Adaptive Chirplet Representation

Adaptive joint time-frequency analysis is a good tool to analyze the time-varying Doppler features of a target. Previously, AJTF was utilized to achieve ISAR motion compensation [8]. As in [7], we are interested here in parameterizing the radar return so

that we can extract the different components of the signal for further processing. For this purpose, the chirplet basis function proposed in [6] is used. The radar signal as a function of dwell time t is expanded in terms of N basis functions as follows:

$$s(t) = \sum_{k=1}^{N} c_k (2\alpha_k / \pi)^{1/4} \exp[-(t - tk)^2 / \alpha_k^2 + j2\pi f_k (t - t_k) + j\pi\beta_k (t - t_k)^2] \quad (1)$$

where c_k is the coefficient with the kth basis function. Each basis function is a four-parameter chirplet with time location t_k, frequency center f_k, time extent α_k, and chirp rate β_k. The parameters for all the individual chirplets are found adaptively. The chirplet with the highest energy is extracted first. We exhaustively search for the maximum projection from the radar signal onto the set of basis functions in the parameter space. Once the best basis is identified, we then subtract its contribution from the radar signal and continue to search for the next best basis. This process is iterated until we have a good representation the original signal.

3. Results from Walking Man Data

A particular example with micro-Doppler features is the radar data of a walking man [2]. Figure 1 shows the geometry of the situation. During the data collection, a man walked toward the radar. At least two different motions were present on the walking man: the steady body motion and the swinging arm motion. One segment of the radar data after range compression is shown in Figure 2. We see the nearly linear range variation in the figure due to the steady walking speed of the man. We first carry out a coarse range alignment by correlating the range profiles. The signal through a particular range cell is then used for JTF processing. Shown in Figure 3 is the spectrogram (generated using the

short-time Fourier transform) of the radar signal in a particular range cell containing strong micro-Doppler. We immediately recognize the two motion components present in this figure. The horizontal trajectory is due to the body motion, while the sinusoidal curve is due to the arm swing.

We apply the JTF extraction outlined in Section 2 and extract 50 chirplets. After the parameterization, we separate the body and the arm returns. As can be seen in Figure 3, the body return should consist of chirplet bases with both small Doppler frequency f_k and small chirp rate β_k. By applying this criterion to the basis functions representing the signal, we can separate the body return from the arm return. The results are shown in Figures 4a and 4b, respectively. Notice that the main features in the two returns are preserved after the JTF extraction. The Doppler features due to the arm swing shown in Figure 4b are nearly periodic. This period can be easily estimated from the arm-only data by taking the autocorrelation of the time sequence. The result is shown in Figure 5a. The peaks in the autocorrelation function indicate the period of the motion and it is estimated to be 0.44 sec. Note that without using JTF analysis, accurate detection of the swing period would be more difficult due to the presence of the body return. The autocorrelation calculated from the unfiltered data is shown in Fig. 4b. As we can see, the peaks are much less prominent.

4. Conclusions

Adaptive joint time-frequency analysis is an effective technique to extract micro-Doppler features. Using the measured radar data of a walking man, we showed that it is possible to separate the return of the body from that of the swinging arm. Furthermore,

we showed that the arm swing period could be accurately estimated from the arm return. This work can be extended for other targets with non-rigid body motions. The extracted micro-Doppler features may be exploited for target identification applications.

Acknowledgement

This work is supported by the Office of Naval Research under contract No. N00014-98-1-0615.

References

[1] A. Ausherman, A. Kozma, J. L. Waker, H. M. Jones and E. C. Poggio, "Developments in radar imaging," *IEEE Trans. Aerospace Electron. Syst.,* vol. 20, no. 4, pp. 363-400, July 1984.

[2] V.C. Chen, "Analysis of radar micro-Doppler with time-frequency transform," *Proc. of the 10th IEEE workshop on Statistical Signal and Array Processing*, pp. 463-466, Pocono Manor, PA, Aug. 2000.

[3] E. F. Greneker, J. L. Geisheimer, D. Asbell, "Extraction of micro-Doppler data from vehicle targets at x-band frequencies," *SPIE Proc. Radar Sensor Technology VI*, vol. 4374, pp. 1-9, Orlando, FL, Apr. 2001.

[4] S. Qian and D. Chen, "Signal representation using adaptive normalized Gaussian functions," *Signal Processing*, vol. 36, no. 1, pp. 1-11, Mar. 1994.

[5] S. G. Mallat and Z. Zhang, "Matching pursuits with time-frequency dictionaries," *IEEE Trans. Signal Processing*, vol. 41, no. 12, pp. 3397-3415, Dec. 1993.

[6] S. Qian, D. Chen and Q. Yin, "Adaptive chirplet based signal approximation," *Proc. ICASSP*, vol. III, pp. 1871-1874, May 1998.

[7] Y. Wang, H. Ling and V. C. Chen, "Application of adaptive joint time-frequency processing to ISAR image enhancement and Doppler feature extraction for targets with rotating parts," *SPIE 43rd Annual Meeting, Radar Processing, Technology, and Applications*, vol. 3462, pp. 156-163, San Diego, CA, July 1998.

[8] Y. Wang, H. Ling and V. C. Chen, " ISAR motion compensation via adaptive joint time-frequency techniques," *IEEE Trans. Aerospace Electron. Syst.*, vol. 34, no. 2, pp. 670-677, Apr. 1998.

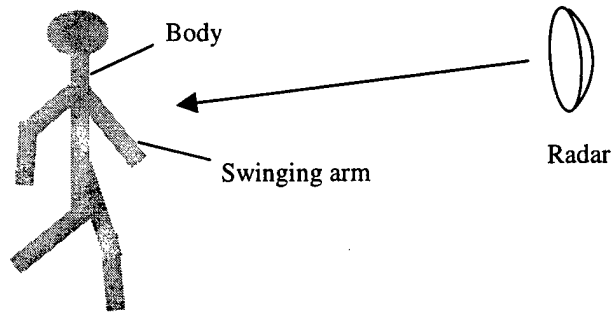

Fig. 1 Geometry of the problem -- radar data collection of a walking man.

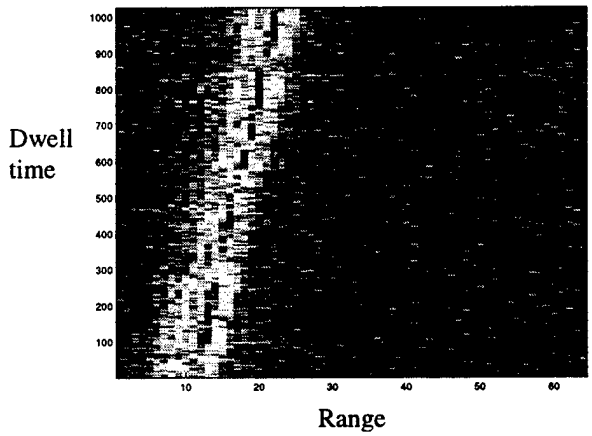

Fig. 2 Radar data after range compression

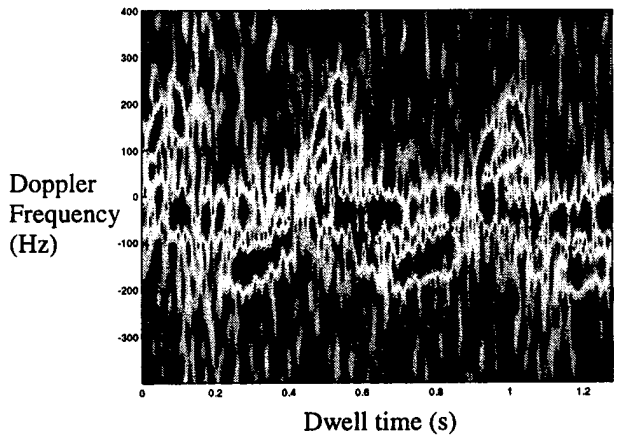

Fig. 3 Spectrogram of the radar signal showing micro-Doppler features of the swinging arm.

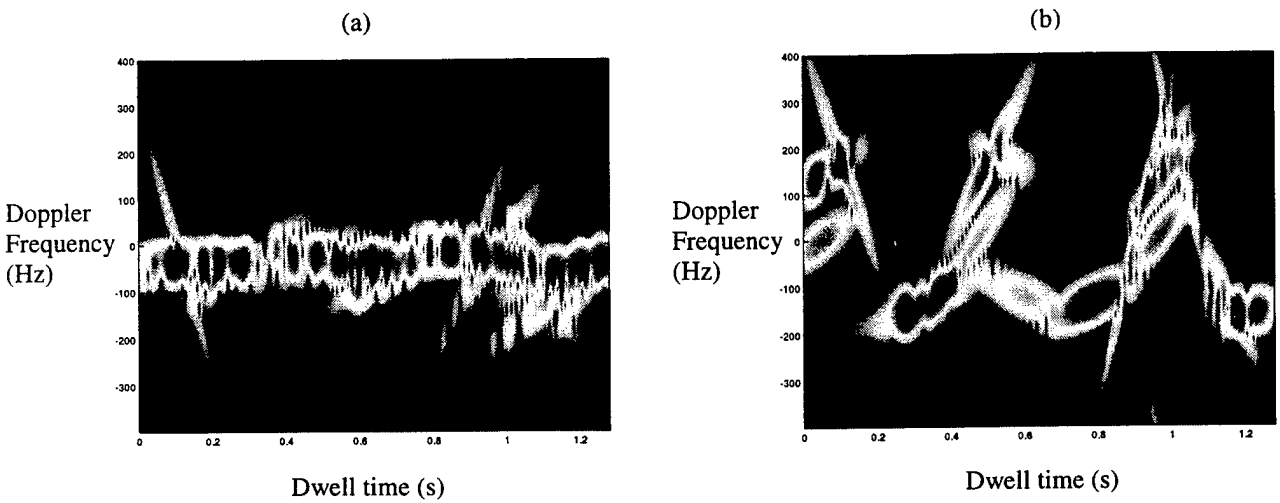

Fig. 4 Separation of the contribution from (a) the body and (b) the swing arm using the adaptive chirplet representation.

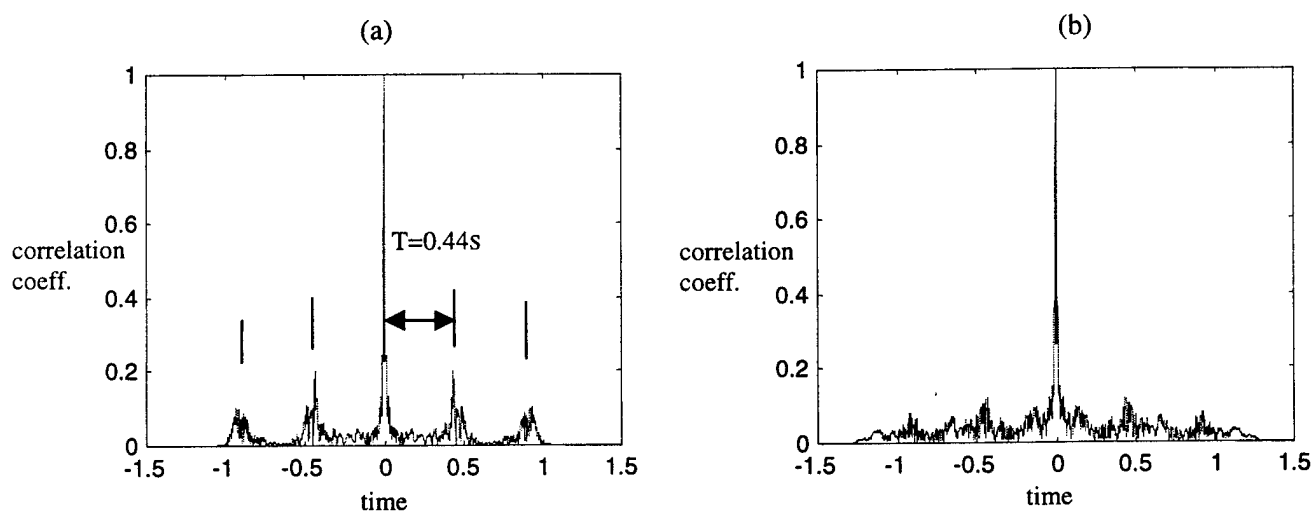

Fig. 5 Autocorrelation to determine the rate of arm swing.
(a) after JTF extraction (b) before JTF extraction.